

APPENDIX A: BENCHMARK CALCULATIONS
(Total of 26 Pages Including This Page)

Note: This appendix was taken from a different report. Hence, the next page is labeled
"Appendix 4A, Page 1".

APPENDIX 4A: BENCHMARK CALCULATIONS

4A.1 INTRODUCTION AND SUMMARY

Benchmark calculations have been made on selected critical experiments, chosen, in so far as possible, to bound the range of variables in the rack designs. Two independent methods of analysis were used, differing in cross section libraries and in the treatment of the cross sections. MCNP4a [4A.1] is a continuous energy Monte Carlo code and KENO5a [4A.2] uses group-dependent cross sections. For the KENO5a analyses reported here, the 238-group library was chosen, processed through the NITAWL-II [4A.2] program to create a working library and to account for resonance self-shielding in uranium-238 (Nordheim integral treatment). The 238 group library was chosen to avoid or minimize the errors[†] (trends) that have been reported (e.g., [4A.3 through 4A.5]) for calculations with collapsed cross section sets.

In rack designs, the three most significant parameters affecting criticality are (1) the fuel enrichment, (2) the ¹⁰B loading in the neutron absorber, and (3) the lattice spacing (or water-gap thickness if a flux-trap design is used). Other parameters, within the normal range of rack and fuel designs, have a smaller effect, but are also included in the analyses.

Table 4A.1 summarizes results of the benchmark calculations for all cases selected and analyzed, as referenced in the table. The effect of the major variables are discussed in subsequent sections below. It is important to note that there is obviously considerable overlap in parameters since it is not possible to vary a single parameter and maintain criticality; some other parameter or parameters must be concurrently varied to maintain criticality.

One possible way of representing the data is through a spectrum index that incorporates all of the variations in parameters. KENO5a computes and prints the "energy of the average lethargy causing fission" (EALF). In MCNP4a, by utilizing the tally option with the identical 238-group energy structure as in KENO5a, the number of fissions in each group may be collected and the EALF determined (post-processing).

[†] Small but observable trends (errors) have been reported for calculations with the 27-group and 44-group collapsed libraries. These errors are probably due to the use of a single collapsing spectrum when the spectrum should be different for the various cases analyzed, as evidenced by the spectrum indices.

Figures 4A.1 and 4A.2 show the calculated k_{eff} for the benchmark critical experiments as a function of the EALF for MCNP4a and KENO5a, respectively (UO_2 fuel only). The scatter in the data (even for comparatively minor variation in critical parameters) represents experimental error[†] in performing the critical experiments within each laboratory, as well as between the various testing laboratories. The B&W critical experiments show a larger experimental error than the PNL criticals. This would be expected since the B&W criticals encompass a greater range of critical parameters than the PNL criticals.

Linear regression analysis of the data in Figures 4A.1 and 4A.2 show that there are no trends, as evidenced by very low values of the correlation coefficient (0.13 for MCNP4a and 0.21 for KENO5a). The total bias (systematic error, or mean of the deviation from a k_{eff} of exactly 1.000) for the two methods of analysis are shown in the table below.

Calculational Bias of MCNP4a and KENO5a	
MCNP4a	0.0009 ± 0.0011
KENO5a	0.0030 ± 0.0012

The bias and standard error of the bias were derived directly from the calculated k_{eff} values in Table 4A.1 using the following equations^{††}, with the standard error multiplied by the one-sided K-factor for 95% probability at the 95% confidence level from NBS Handbook 91 [4A.18] (for the number of cases analyzed, the K-factor is ~2.05 or slightly more than 2).

$$\bar{k} = \frac{1}{n} \sum_i^n k_i \quad (4A.1)$$

[†] A classical example of experimental error is the corrected enrichment in the PNL experiments, first as an addendum to the initial report and, secondly, by revised values in subsequent reports for the same fuel rods.

^{††} These equations may be found in any standard text on statistics, for example, reference [4A.6] (or the MCNP4a manual) and is the same methodology used in MCNP4a and in KENO5a.

$$\sigma_k^2 = \frac{\sum_{i=1}^n k_i^2 - (\sum_{i=1}^n k_i)^2 / n}{n (n-1)} \quad (4A.2)$$

$$Bias = (1 - \bar{k}) \pm K \sigma_{\bar{k}} \quad (4A.3)$$

where k_i are the calculated reactivities of n critical experiments; σ_k is the unbiased estimator of the standard deviation of the mean (also called the standard error of the bias (mean)); K is the one-sided multiplier for 95% probability at the 95% confidence level (NBS Handbook 91 [4A.18]).

Formula 4.A.3 is based on the methodology of the National Bureau of Standards (now NIST) and is used to calculate the values presented on page 4.A-2. The first portion of the equation, $(1 - \bar{k})$, is the actual bias which is added to the MCNP4a and KENO5a results. The second term, $K \sigma_{\bar{k}}$, is the uncertainty or standard error associated with the bias. The K values used were obtained from the National Bureau of Standards Handbook 91 and are for one-sided statistical tolerance limits for 95% probability at the 95% confidence level. The actual K values for the 56 critical experiments evaluated with MCNP4a and the 53 critical experiments evaluated with KENO5a are 2.04 and 2.05, respectively.

The bias values are used to evaluate the maximum k_{eff} values for the rack designs. KENO5a has a slightly larger systematic error than MCNP4a, but both result in greater precision than published data [4A.3 through 4A.5] would indicate for collapsed cross section sets in KENO5a (SCALE) calculations.

4A.2 Effect of Enrichment

The benchmark critical experiments include those with enrichments ranging from 2.46 w/o to 5.74 w/o and therefore span the enrichment range for rack designs. Figures 4A.3 and 4A.4 show the calculated k_{eff} values (Table 4A.1) as a function of the fuel enrichment reported for the critical experiments. Linear regression analyses for these data confirms that there are no trends, as indicated by low values of the correlation coefficients (0.03 for MCNP4a and 0.38 for KENO5a). Thus, there are no corrections to the bias for the various enrichments.

As further confirmation of the absence of any trends with enrichment, a typical configuration was calculated with both MCNP4a and KENO5a for various enrichments. The cross-comparison of calculations with codes of comparable sophistication is suggested in Reg. Guide 3.41. Results of this comparison, shown in Table 4A.2 and Figure 4A.5, confirm no significant difference in the calculated values of k_{eff} for the two independent codes as evidenced by the 45° slope of the curve. Since it is very unlikely that two independent methods of analysis would be subject to the same error, this comparison is considered confirmation of the absence of an enrichment effect (trend) in the bias.

4A.3 Effect of ^{10}B Loading

Several laboratories have performed critical experiments with a variety of thin absorber panels similar to the Boral panels in the rack designs. Of these critical experiments, those performed by B&W are the most representative of the rack designs. PNL has also made some measurements with absorber plates, but, with one exception (a flux-trap experiment), the reactivity worth of the absorbers in the PNL tests is very low and any significant errors that might exist in the treatment of strong thin absorbers could not be revealed.

Table 4A.3 lists the subset of experiments using thin neutron absorbers (from Table 4A.1) and shows the reactivity worth (Δk) of the absorber.[†]

No trends with reactivity worth of the absorber are evident, although based on the calculations shown in Table 4A.3, some of the B&W critical experiments seem to have unusually large experimental errors. B&W made an effort to report some of their experimental errors. Other laboratories did not evaluate their experimental errors.

To further confirm the absence of a significant trend with ^{10}B concentration in the absorber, a cross-comparison was made with MCNP4a and KENO5a (as suggested in Reg. Guide 3.41). Results are shown in Figure 4A.6 and Table 4A.4 for a typical geometry. These data substantiate the absence of any error (trend) in either of the two codes for the conditions analyzed (data points fall on a 45° line, within an expected 95% probability limit).

[†] The reactivity worth of the absorber panels was determined by repeating the calculation with the absorber analytically removed and calculating the incremental (Δk) change in reactivity due to the absorber.

4A.4 Miscellaneous and Minor Parameters

4A.4.1 Reflector Material and Spacings

PNL has performed a number of critical experiments with thick steel and lead reflectors.[†] Analysis of these critical experiments are listed in Table 4A.5 (subset of data in Table 4A.1). There appears to be a small tendency toward overprediction of k_{eff} at the lower spacing, although there are an insufficient number of data points in each series to allow a quantitative determination of any trends. The tendency toward overprediction at close spacing means that the rack calculations may be slightly more conservative than otherwise.

4A.4.2 Fuel Pellet Diameter and Lattice Pitch

The critical experiments selected for analysis cover a range of fuel pellet diameters from 0.311 to 0.444 inches, and lattice spacings from 0.476 to 1.00 inches. In the rack designs, the fuel pellet diameters range from 0.303 to 0.3805 inches O.D. (0.496 to 0.580 inch lattice spacing) for PWR fuel and from 0.3224 to 0.494 inches O.D. (0.488 to 0.740 inch lattice spacing) for BWR fuel. Thus, the critical experiments analyzed provide a reasonable representation of power reactor fuel. Based on the data in Table 4A.1, there does not appear to be any observable trend with either fuel pellet diameter or lattice pitch, at least over the range of the critical experiments applicable to rack designs.

4A.4.3 Soluble Boron Concentration Effects

Various soluble boron concentrations were used in the B&W series of critical experiments and in one PNL experiment, with boron concentrations ranging up to 2550 ppm. Results of MCNP4a (and one KENO5a) calculations are shown in Table 4A.6. Analyses of the very high boron concentration experiments (> 1300 ppm) show a tendency to slightly overpredict reactivity for the three experiments exceeding 1300 ppm. In turn, this would suggest that the evaluation of the racks with higher soluble boron concentrations could be slightly conservative.

[†] Parallel experiments with a depleted uranium reflector were also performed but not included in the present analysis since they are not pertinent to the Holtec rack design.

4A.5 MOX Fuel

The number of critical experiments with PuO_2 bearing fuel (MOX) is more limited than for UO_2 fuel. However, a number of MOX critical experiments have been analyzed and the results are shown in Table 4A.7. Results of these analyses are generally above a k_{eff} of 1.00, indicating that when Pu is present, both MCNP4a and KENO5a overpredict the reactivity. This may indicate that calculation for MOX fuel will be expected to be conservative, especially with MCNP4a. It may be noted that for the larger lattice spacings, the KENO5a calculated reactivities are below 1.00, suggesting that a small trend may exist with KENO5a. It is also possible that the overprediction in k_{eff} for both codes may be due to a small inadequacy in the determination of the Pu-241 decay and Am-241 growth. This possibility is supported by the consistency in calculated k_{eff} over a wide range of the spectral index (energy of the average lethargy causing fission).

References

- [4A.1] J.F. Briesmeister, Ed., "MCNP4a - A General Monte Carlo N-Particle Transport Code, Version 4A; Los Alamos National Laboratory, LA-12625-M (1993).
- [4A.2] SCALE 4.3, "A Modular Code System for Performing Standardized Computer Analyses for Licensing Evaluation", NUREG-0200 (ORNL-NUREG-CSD-2/U2/R5, Revision 5, Oak Ridge National Laboratory, September 1995.
- [4A.3] M.D. DeHart and S.M. Bowman, "Validation of the SCALE Broad Structure 44-G Group ENDF/B-Y Cross-Section Library for Use in Criticality Safety Analyses", NUREG/CR-6102 (ORNL/TM-12460) Oak Ridge National Laboratory, September 1994.
- [4A.4] W.C. Jordan et al., "Validation of KENO.V.a", CSD/TM-238, Martin Marietta Energy Systems, Inc., Oak Ridge National Laboratory, December 1986.
- [4A.5] O.W. Hermann et al., "Validation of the Scale System for PWR Spent Fuel Isotopic Composition Analysis", ORNL-TM-12667, Oak Ridge National Laboratory, undated.
- [4A.6] R.J. Larsen and M.L. Marx, An Introduction to Mathematical Statistics and its Applications, Prentice-Hall, 1986.
- [4A.7] M.N. Baldwin et al., Critical Experiments Supporting Close Proximity Water Storage of Power Reactor Fuel, BAW-1484-7, Babcock and Wilcox Company, July 1979.
- [4A.8] G.S. Hoovier et al., Critical Experiments Supporting Underwater Storage of Tightly Packed Configurations of Spent Fuel Pins, BAW-1645-4, Babcock & Wilcox Company, November 1991.
- [4A.9] L.W. Newman et al., Urania Gadolinia: Nuclear Model Development and Critical Experiment Benchmark, BAW-1810, Babcock and Wilcox Company, April 1984.

- [4A.10] J.C. Manaranche et al., "Dissolution and Storage Experimental Program with 4.75 w/o Enriched Uranium-Oxide Rods," Trans. Am. Nucl. Soc. 33: 362-364 (1979).
- [4A.11] S.R. Bierman and E.D. Clayton, Criticality Experiments with Subcritical Clusters of 2.35 w/o and 4.31 w/o ^{235}U Enriched UO_2 Rods in Water with Steel Reflecting Walls, PNL-3602, Battelle Pacific Northwest Laboratory, April 1981.
- [4A.12] S.R. Bierman et al., Criticality Experiments with Subcritical Clusters of 2.35 w/o and 4.31 w/o ^{235}U Enriched UO_2 Rods in Water with Uranium or Lead Reflecting Walls, PNL-3926, Battelle Pacific Northwest Laboratory, December, 1981.
- [4A.13] S.R. Bierman et al., Critical Separation Between Subcritical Clusters of 4.31 w/o ^{235}U Enriched UO_2 Rods in Water with Fixed Neutron Poisons, PNL-2615, Battelle Pacific Northwest Laboratory, October 1977.
- [4A.14] S.R. Bierman, Criticality Experiments with Neutron Flux Traps Containing Voids, PNL-7167, Battelle Pacific Northwest Laboratory, April 1990.
- [4A.15] B.M. Durst et al., Critical Experiments with 4.31 wt % ^{235}U Enriched UO_2 Rods in Highly Borated Water Lattices, PNL-4267, Battelle Pacific Northwest Laboratory, August 1982.
- [4A.16] S.R. Bierman, Criticality Experiments with Fast Test Reactor Fuel Pins in Organic Moderator, PNL-5803, Battelle Pacific Northwest Laboratory, December 1981.
- [4A.17] E.G. Taylor et al., Saxton Plutonium Program Critical Experiments for the Saxton Partial Plutonium Core, WCAP-3385-54, Westinghouse Electric Corp., Atomic Power Division, December 1965.
- [4A.18] M.G. Natrella, Experimental Statistics, National Bureau of Standards, Handbook 91, August 1963.

Table 4A.1

Summary of Criticality Benchmark Calculations

			Calculated k_{eff}		EALF' (eV)		
Reference	Identification	Enrich.	MCNP4a	KENO5a	MCNP4a	KENO5a	
1	B&W-1484 (4A.7)	Core I	2.46	0.9964 ± 0.0010	0.9898 ± 0.0006	0.1759	0.1753
2	B&W-1484 (4A.7)	Core II	2.46	1.0008 ± 0.0011	1.0015 ± 0.0005	0.2553	0.2446
3	B&W-1484 (4A.7)	Core III	2.46	1.0010 ± 0.0012	1.0005 ± 0.0005	0.1999	0.1939
4	B&W-1484 (4A.7)	Core IX	2.46	0.9956 ± 0.0012	0.9901 ± 0.0006	0.1422	0.1426
5	B&W-1484 (4A.7)	Core X	2.46	0.9980 ± 0.0014	0.9922 ± 0.0006	0.1513	0.1499
6	B&W-1484 (4A.7)	Core XI	2.46	0.9978 ± 0.0012	1.0005 ± 0.0005	0.2031	0.1947
7	B&W-1484 (4A.7)	Core XII	2.46	0.9988 ± 0.0011	0.9978 ± 0.0006	0.1718	0.1662
8	B&W-1484 (4A.7)	Core XIII	2.46	1.0020 ± 0.0010	0.9952 ± 0.0006	0.1988	0.1965
9	B&W-1484 (4A.7)	Core XIV	2.46	0.9953 ± 0.0011	0.9928 ± 0.0006	0.2022	0.1986
10	B&W-1484 (4A.7)	Core XV "	2.46	0.9910 ± 0.0011	0.9909 ± 0.0006	0.2092	0.2014
11	B&W-1484 (4A.7)	Core XVI "	2.46	0.9935 ± 0.0010	0.9889 ± 0.0006	0.1757	0.1713
12	B&W-1484 (4A.7)	Core XVII	2.46	0.9962 ± 0.0012	0.9942 ± 0.0005	0.2083	0.2021
13	B&W-1484 (4A.7)	Core XVIII	2.46	1.0036 ± 0.0012	0.9931 ± 0.0006	0.1705	0.1708

Table 4A.1

Summary of Criticality Benchmark Calculations

			Calculated k_{eff}		EALF ¹ (eV)		
Reference	Identification	Enrich.	MCNP4a	KENO5a	MCNP4a	KENO5a	
14	B&W-1484 (4A.7)	Core XIX	2.46	0.9961 ± 0.0012	0.9971 ± 0.0005	0.2103	0.2011
15	B&W-1484 (4A.7)	Core XX	2.46	1.0008 ± 0.0011	0.9932 ± 0.0006	0.1724	0.1701
16	B&W-1484 (4A.7)	Core XXI	2.46	0.9994 ± 0.0010	0.9918 ± 0.0006	0.1544	0.1536
17	B&W-1645 (4A.8)	S-type Fuel, w/886 ppm B	2.46	0.9970 ± 0.0010	0.9924 ± 0.0006	1.4475	1.4680
18	B&W-1645 (4A.8)	S-type Fuel, w/746 ppm B	2.46	0.9990 ± 0.0010	0.9913 ± 0.0006	1.5463	1.5660
19	B&W-1645 (4A.8)	SO-type Fuel, w/1156 ppm B	2.46	0.9972 ± 0.0009	0.9949 ± 0.0005	0.4241	0.4331
20	B&W-1810 (4A.9)	Case 1 1337 ppm B	2.46	1.0023 ± 0.0010	NC	0.1531	NC
21	B&W-1810 (4A.9)	Case 12 1899 ppm B	2.46/4.02	1.0060 ± 0.0009	NC	0.4493	NC
22	French (4A.10)	Water Moderator 0 gap	4.75	0.9966 ± 0.0013	NC	0.2172	NC
23	French (4A.10)	Water Moderator 2.5 cm gap	4.75	0.9952 ± 0.0012	NC	0.1778	NC
24	French (4A.10)	Water Moderator 5 cm gap	4.75	0.9943 ± 0.0010	NC	0.1677	NC
25	French (4A.10)	Water Moderator 10 cm gap	4.75	0.9979 ± 0.0010	NC	0.1736	NC
26	PNL-3602 (4A.11)	Steel Reflector, 0 separation	2.35	NC	1.0004 ± 0.0006	NC	0.1018

Table 4A.1

Summary of Criticality Benchmark Calculations

			Calculated k_{eff}		EALF [†] (eV)		
Reference	Identification	Enrich.	MCNP4a	KENO5a	MCNP4a	KENO5a	
27	PNL-3602 (4A.11)	Steel Reflector, 1.321 cm sepn.	2.35	0.9980 ± 0.0009	0.9992 ± 0.0006	0.1000	0.0909
28	PNL-3602 (4A.11)	Steel Reflector, 2.616 cm sepn	2.35	0.9968 ± 0.0009	0.9964 ± 0.0006	0.0981	0.0975
29	PNL-3602 (4A.11)	Steel Reflector, 3.912 cm sepn.	2.35	0.9974 ± 0.0010	0.9980 ± 0.0006	0.0976	0.0970
30	PNL-3602 (4A.11)	Steel Reflector, infinite sepn.	2.35	0.9962 ± 0.0008	0.9939 ± 0.0006	0.0973	0.0968
31	PNL-3602 (4A.11)	Steel Reflector, 0 cm sepn.	4.306	NC	1.0003 ± 0.0007	NC	0.3282
32	PNL-3602 (4A.11)	Steel Reflector, 1.321 cm sepn.	4.306	0.9997 ± 0.0010	1.0012 ± 0.0007	0.3016	0.3039
33	PNL-3602 (4A.11)	Steel Reflector, 2.616 cm sepn.	4.306	0.9994 ± 0.0012	0.9974 ± 0.0007	0.2911	0.2927
34	PNL-3602 (4A.11)	Steel Reflector, 5.405 cm sepn.	4.306	0.9969 ± 0.0011	0.9951 ± 0.0007	0.2828	0.2860
35	PNL-3602 (4A.11)	Steel Reflector, Infinite sepn. ^{††}	4.306	0.9910 ± 0.0020	0.9947 ± 0.0007	0.2851	0.2864
36	PNL-3602 (4A.11)	Steel Reflector, with Boral Sheets	4.306	0.9941 ± 0.0011	0.9970 ± 0.0007	0.3135	0.3150
37	PNL-3926 (4A.12)	Lead Reflector, 0 cm sepn.	4.306	NC	1.0003 ± 0.0007	NC	0.3159
38	PNL-3926 (4A.12)	Lead Reflector, 0.55 cm sepn.	4.306	1.0025 ± 0.0011	0.9997 ± 0.0007	0.3030	0.3044
39	PNL-3926 (4A.12)	Lead Reflector, 1.956 cm sepn.	4.306	1.0000 ± 0.0012	0.9985 ± 0.0007	0.2883	0.2930

Table 4A.1

Summary of Criticality Benchmark Calculations

			Calculated k_{eff}		EALF [†] (eV)		
Reference	Identification	Enrich.	MCNP4a	KENO5a	MCNP4a	KENO5a	
40	PNL-3926 (4A.12)	Lead Reflector, 5.405 cm sepn.	4.306	0.9971 ± 0.0012	0.9946 ± 0.0007	0.2831	0.2854
41	PNL-2615 (4A.13)	Experiment 004/032 - no absorber	4.306	0.9925 ± 0.0012	0.9950 ± 0.0007	0.1155	0.1159
42	PNL-2615 (4A.13)	Experiment 030 - Zr plates	4.306	NC	0.9971 ± 0.0007	NC	0.1154
43	PNL-2615 (4A.13)	Experiment 013 - Steel plates	4.306	NC	0.9965 ± 0.0007	NC	0.1164
44	PNL-2615 (4A.13)	Experiment 014 - Steel plates	4.306	NC	0.9972 ± 0.0007	NC	0.1164
45	PNL-2615 (4A.13)	Exp. 009 1.05% Boron-Steel plates	4.306	0.9982 ± 0.0010	0.9981 ± 0.0007	0.1172	0.1162
46	PNL-2615 (4A.13)	Exp. 012 1.62% Boron-Steel plates	4.306	0.9996 ± 0.0012	0.9982 ± 0.0007	0.1161	0.1173
47	PNL-2615 (4A.13)	Exp. 031 - Boral plates	4.306	0.9994 ± 0.0012	0.9969 ± 0.0007	0.1165	0.1171
48	PNL-7167 (4A.14)	Experiment 214R - with flux trap	4.306	0.9991 ± 0.0011	0.9956 ± 0.0007	0.3722	0.3812
49	PNL-7167 (4A.14)	Experiment 214V3 - with flux trap	4.306	0.9969 ± 0.0011	0.9963 ± 0.0007	0.3742	0.3826
50	PNL-4267 (4A.15)	Case 173 - 0 ppm B	4.306	0.9974 ± 0.0012	NC	0.2893	NC
51	PNL-4267 (4A.15)	Case 177 - 2550 ppm B	4.306	1.0057 ± 0.0010	NC	0.5509	NC
52	PNL-5803 (4A.16)	MOX Fuel - Type 3.2 Exp. 21	20% Pu	1.0041 ± 0.0011	1.0046 ± 0.0006	0.9171	0.8868

Table 4A.1

Summary of Criticality Benchmark Calculations

			Calculated k_{eff}		EALF [†] (eV)		
Reference	Identification	Enrich.	MCNP4a	KENO5a	MCNP4a	KENO5a	
53	PNL-5803 (4A.16)	MOX Fuel - Type 3.2 Exp. 43	20% Pu	1.0058 ± 0.0012	1.0036 ± 0.0006	0.2968	0.2944
54	PNL-5803 (4A.16)	MOX Fuel - Type 3.2 Exp. 13	20% Pu	1.0083 ± 0.0011	0.9989 ± 0.0006	0.1665	0.1706
55	PNL-5803 (4A.16)	MOX Fuel - Type 3.2 Exp. 32	20% Pu	1.0079 ± 0.0011	0.9966 ± 0.0006	0.1139	0.1165
56	WCAP-3385 (4A.17)	Saxton Case 52 PuO2 0.52" pitch	6.6% Pu	0.9996 ± 0.0011	1.0005 ± 0.0006	0.8665	0.8417
57	WCAP-3385 (4A.17)	Saxton Case 52 U 0.52" pitch	5.74	1.0000 ± 0.0010	0.9956 ± 0.0007	0.4476	0.4580
58	WCAP-3385 (4A.17)	Saxton Case 56 PuO2 0.56" pitch	6.6% Pu	1.0036 ± 0.0011	1.0047 ± 0.0006	0.5289	0.5197
59	WCAP-3385 (4A.17)	Saxton Case 56 borated PuO2	6.6% Pu	1.0008 ± 0.0010	NC	0.6389	NC
60	WCAP-3385 (4A.17)	Saxton Case 56 U 0.56" pitch	5.74	0.9994 ± 0.0011	0.9967 ± 0.0007	0.2923	0.2954
61	WCAP-3385 (4A.17)	Saxton Case 79 PuO2 0.79" pitch	6.6% Pu	1.0063 ± 0.0011	1.0133 ± 0.0006	0.1520	0.1555
62	WCAP-3385 (4A.17)	Saxton Case 79 U 0.79" pitch	5.74	1.0039 ± 0.0011	1.0008 ± 0.0006	0.1036	0.1047

Notes: NC stands for not calculated.

[†] EALF is the energy of the average lethargy causing fission.

^{††} These experimental results appear to be statistical outliers ($>3\sigma$) suggesting the possibility of unusually large experimental error. Although they could justifiably be excluded, for conservatism, they were retained in determining the calculational basis.

Table 4A.2

COMPARISON OF MCNP4a AND KENO5a CALCULATED REACTIVITIES[†]
FOR VARIOUS ENRICHMENTS

Enrichment	Calculated $k_{eff} \pm 1\sigma$	
	MCNP4a	KENO5a
3.0	0.8465 ± 0.0011	0.8478 ± 0.0004
3.5	0.8820 ± 0.0011	0.8841 ± 0.0004
3.75	0.9019 ± 0.0011	0.8987 ± 0.0004
4.0	0.9132 ± 0.0010	0.9140 ± 0.0004
4.2	0.9276 ± 0.0011	0.9237 ± 0.0004
4.5	0.9400 ± 0.0011	0.9388 ± 0.0004

[†] Based on the GE 8x8R fuel assembly.

Table 4A.3

**MCNP4a CALCULATED REACTIVITIES FOR
CRITICAL EXPERIMENTS WITH NEUTRON ABSORBERS**

Ref.	Experiment		Δk Worth of Absorber	MCNP4a Calculated k_{eff}	EALF [†] (eV)
4A.13	PNL-2615	Boral Sheet	0.0139	0.9994 ± 0.0012	0.1165
4A.7	B&W-1484	Core XX	0.0165	1.0008 ± 0.0011	0.1724
4A.13	PNL-2615	1.62% Boron-steel	0.0165	0.9996 ± 0.0012	0.1161
4A.7	B&W-1484	Core XIX	0.0202	0.9961 ± 0.0012	0.2103
4A.7	B&W-1484	Core XXI	0.0243	0.9994 ± 0.0010	0.1544
4A.7	B&W-1484	Core XVII	0.0519	0.9962 ± 0.0012	0.2083
4A.11	PNL-3602	Boral Sheet	0.0708	0.9941 ± 0.0011	0.3135
4A.7	B&W-1484	Core XV	0.0786	0.9910 ± 0.0011	0.2092
4A.7	B&W-1484	Core XVI	0.0845	0.9935 ± 0.0010	0.1757
4A.7	B&W-1484	Core XIV	0.1575	0.9953 ± 0.0011	0.2022
4A.7	B&W-1484	Core XIII	0.1738	1.0020 ± 0.0011	0.1988
4A.14	PNL-7167	Expt 214R flux trap	0.1931	0.9991 ± 0.0011	0.3722

[†]EALF is the energy of the average lethargy causing fission.

Table 4A.4

COMPARISON OF MCNP4a AND KENO5a
CALCULATED REACTIVITIES[†] FOR VARIOUS ¹⁰B LOADINGS

¹⁰ B, g/cm ²	Calculated $k_{\text{eff}} \pm 1\sigma$	
	MCNP4a	KENO5a
0.005	1.0381 \pm 0.0012	1.0340 \pm 0.0004
0.010	0.9960 \pm 0.0010	0.9941 \pm 0.0004
0.015	0.9727 \pm 0.0009	0.9713 \pm 0.0004
0.020	0.9541 \pm 0.0012	0.9560 \pm 0.0004
0.025	0.9433 \pm 0.0011	0.9428 \pm 0.0004
0.03	0.9325 \pm 0.0011	0.9338 \pm 0.0004
0.035	0.9234 \pm 0.0011	0.9251 \pm 0.0004
0.04	0.9173 \pm 0.0011	0.9179 \pm 0.0004

[†] Based on a 4.5% enriched GE 8x8R fuel assembly.

Table 4A.5

**CALCULATIONS FOR CRITICAL EXPERIMENTS WITH
THICK LEAD AND STEEL REFLECTORS[†]**

Ref.	Case	E, wt%	Separation, cm	MCNP4a k_{eff}	KENO5a k_{eff}
4A.11	Steel Reflector	2.35	1.321	0.9980 ± 0.0009	0.9992 ± 0.0006
		2.35	2.616	0.9968 ± 0.0009	0.9964 ± 0.0006
		2.35	3.912	0.9974 ± 0.0010	0.9980 ± 0.0006
		2.35	∞	0.9962 ± 0.0008	0.9939 ± 0.0006
4A.11	Steel Reflector	4.306	1.321	0.9997 ± 0.0010	1.0012 ± 0.0007
		4.306	2.616	0.9994 ± 0.0012	0.9974 ± 0.0007
		4.306	3.405	0.9969 ± 0.0011	0.9951 ± 0.0007
		4.306	∞	0.9910 ± 0.0020	0.9947 ± 0.0007
4A.12	Lead Reflector	4.306	0.55	1.0025 ± 0.0011	0.9997 ± 0.0007
		4.306	1.956	1.0000 ± 0.0012	0.9985 ± 0.0007
		4.306	5.405	0.9971 ± 0.0012	0.9946 ± 0.0007

[†] Arranged in order of increasing reflector-fuel spacing.

Table 4A.6

**CALCULATIONS FOR CRITICAL EXPERIMENTS WITH VARIOUS SOLUBLE
BORON CONCENTRATIONS**

Reference	Experiment	Boron Concentration, ppm	Calculated k_{eff}	
			MCNP4a	KENO5a
4A.15	PNL-4267	0	0.9974 ± 0.0012	-
4A.8	B&W-1645	886	0.9970 ± 0.0010	0.9924 ± 0.0006
4A.9	B&W-1810	1337	1.0023 ± 0.0010	-
4A.9	B&W-1810	1899	1.0060 ± 0.0009	-
4A.15	PNL-4267	2550	1.0057 ± 0.0010	-

Table 4A.7

CALCULATIONS FOR CRITICAL EXPERIMENTS WITH MOX FUEL

Reference	Case [†]	MCNP4a		KENO5a	
		k_{eff}	EALF ^{††}	k_{eff}	EALF ^{††}
PNL-5803 [4A.16]	MOX Fuel - Exp. No. 21	1.0041 ± 0.0011	0.9171	1.0046 ± 0.0006	0.8868
	MOX Fuel - Exp. No. 43	1.0058 ± 0.0012	0.2968	1.0036 ± 0.0006	0.2944
	MOX Fuel - Exp. No. 13	1.0083 ± 0.0011	0.1665	0.9989 ± 0.0006	0.1706
	MOX Fuel - Exp. No. 32	1.0079 ± 0.0011	0.1139	0.9966 ± 0.0006	0.1165
WCAP-3385-54 [4A.17]	Saxton @ 0.52" pitch	0.9996 ± 0.0011	0.8665	1.0005 ± 0.0006	0.8417
	Saxton @ 0.56" pitch	1.0036 ± 0.0011	0.5289	1.0047 ± 0.0006	0.5197
	Saxton @ 0.56" pitch borated	1.0008 ± 0.0010	0.6389	NC	NC
	Saxton @ 0.79" pitch	1.0063 ± 0.0011	0.1520	1.0133 ± 0.0006	0.1555

Note: NC stands for not calculated

[†] Arranged in order of increasing lattice spacing.

^{††} EALF is the energy of the average lethargy causing fission.

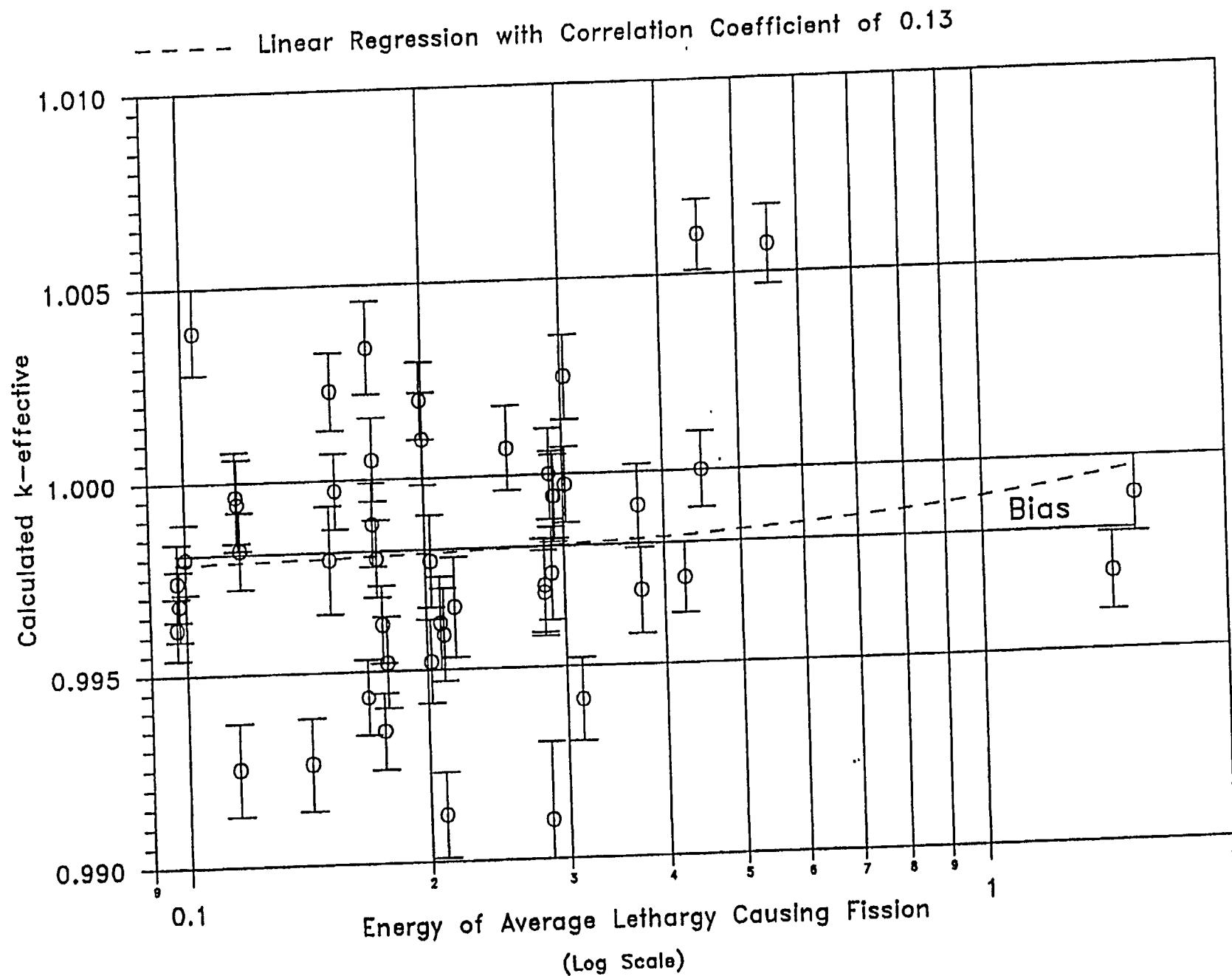
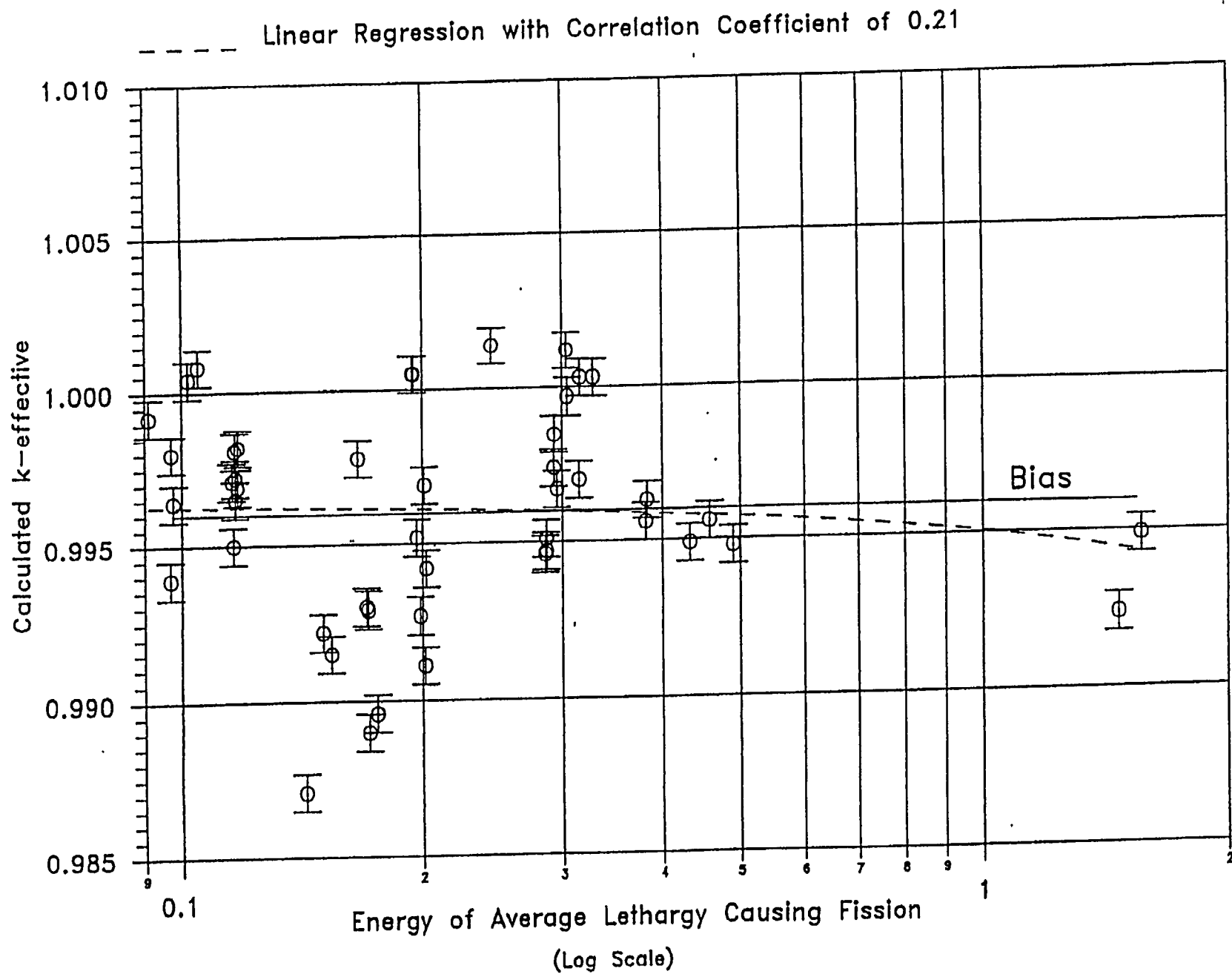


FIGURE 4A.1 : MCNP CALCULATED k-eff VALUES for
VARIOUS VALUES OF THE SPECTRAL INDEX



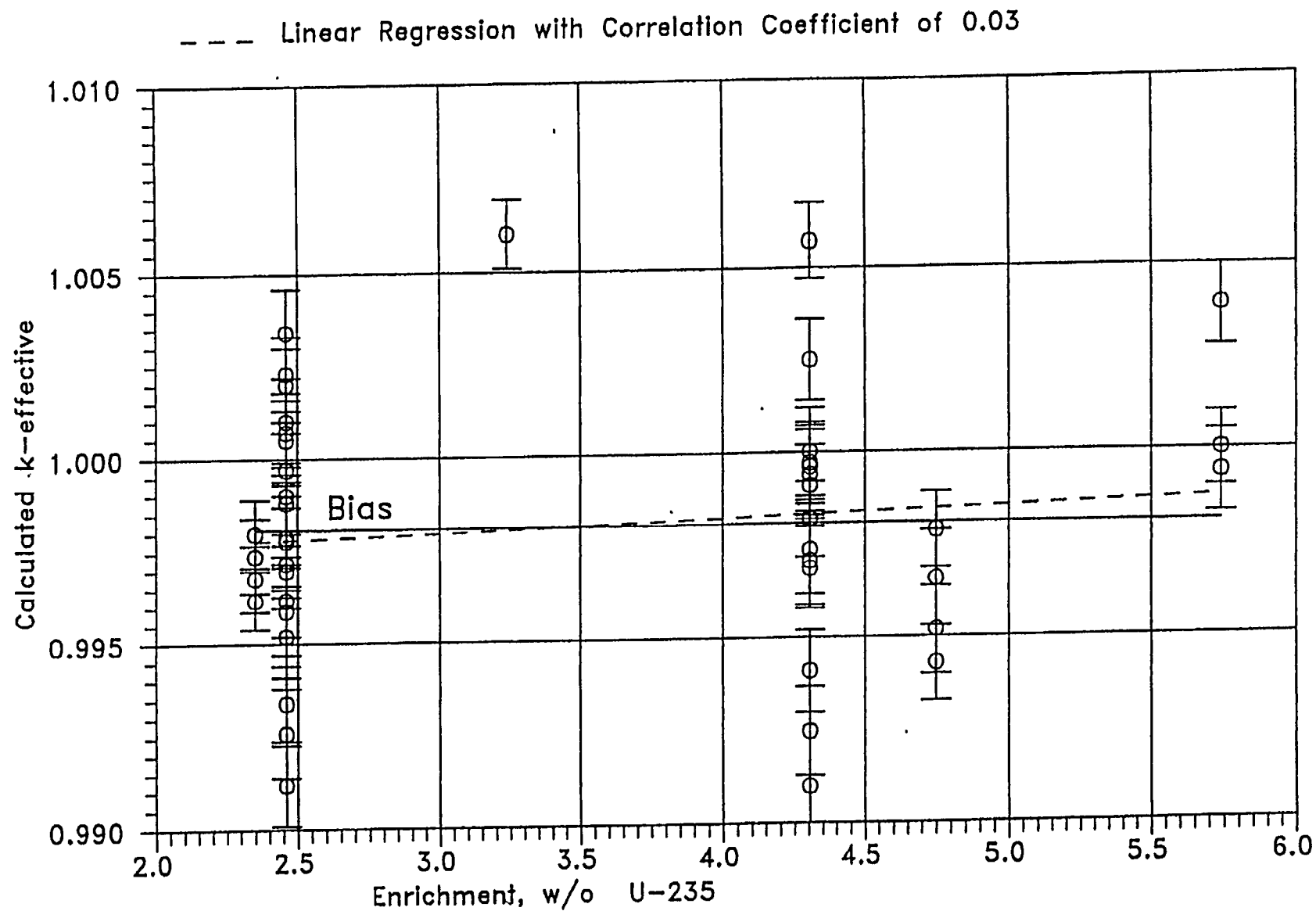


FIGURE 4A.3 MCNP CALCULATED k -eff VALUES
AT VARIOUS U-235 ENRICHMENTS

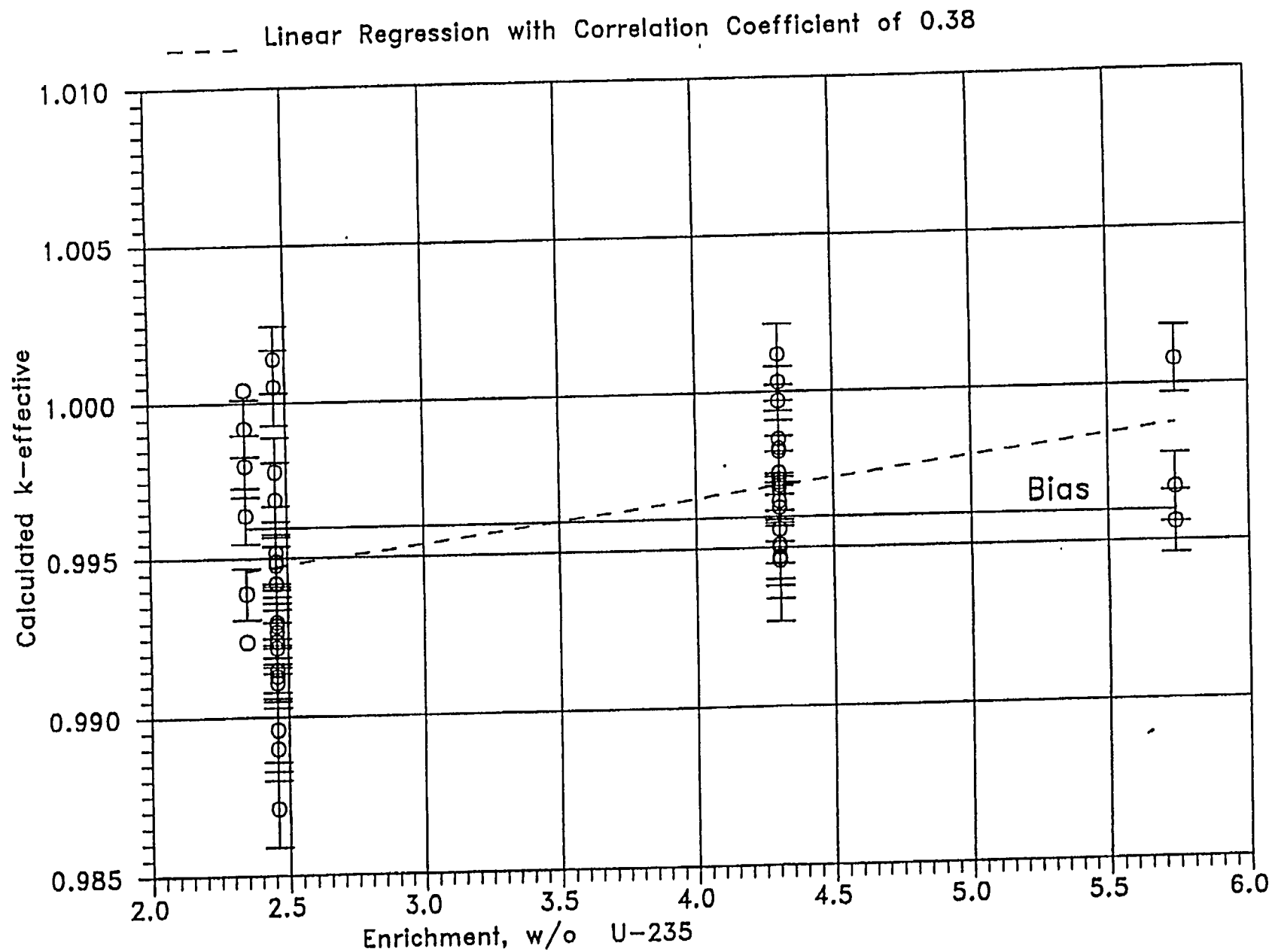


FIGURE 4A.4 KENO CALCULATED k -eff VALUES
AT VARIOUS U-235 ENRICHMENTS

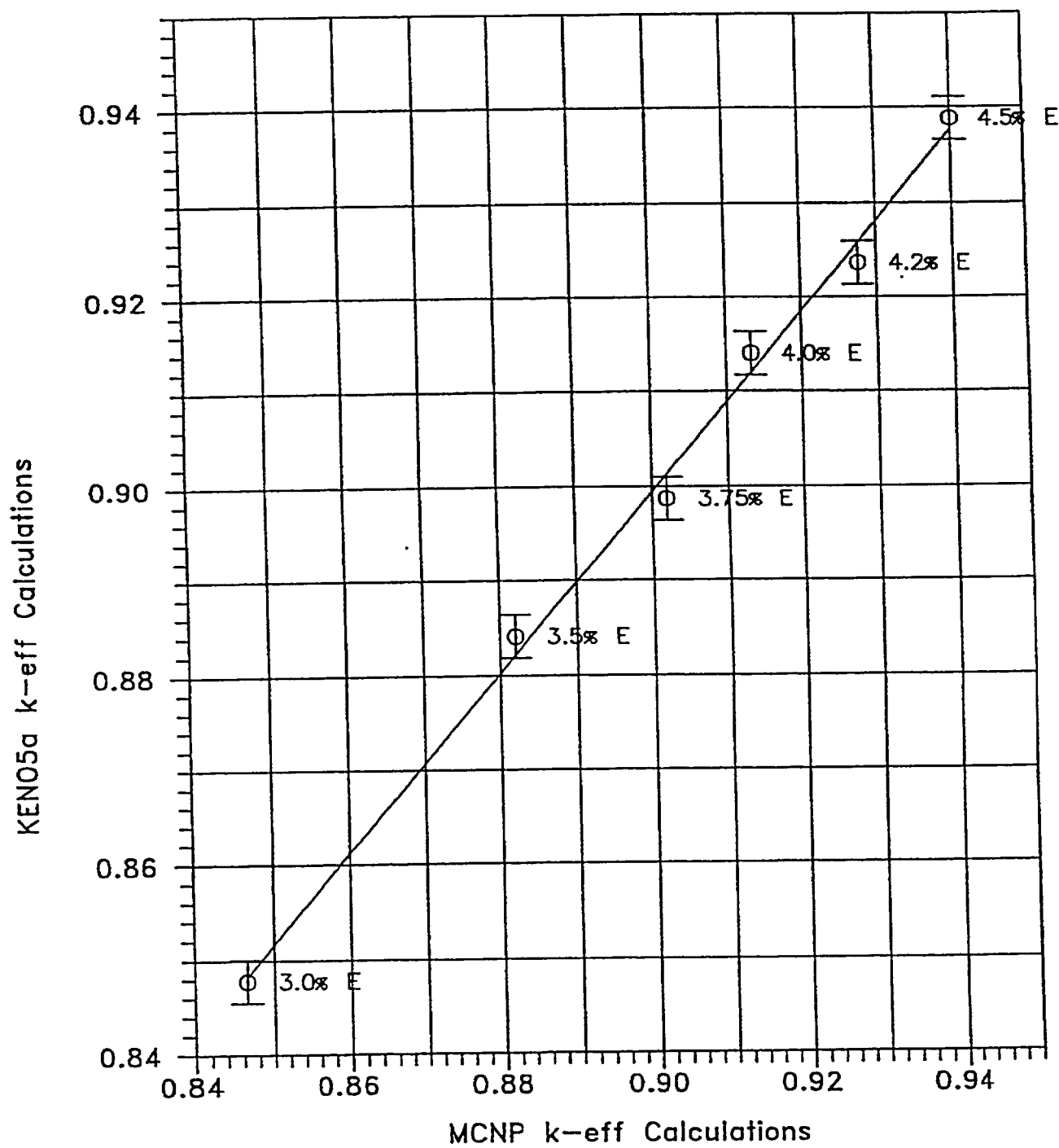


FIGURE 4A.5 COMPARISON OF MCNP AND KENO5A CALCULATIONS FOR VARIOUS FUEL ENRICHMENTS

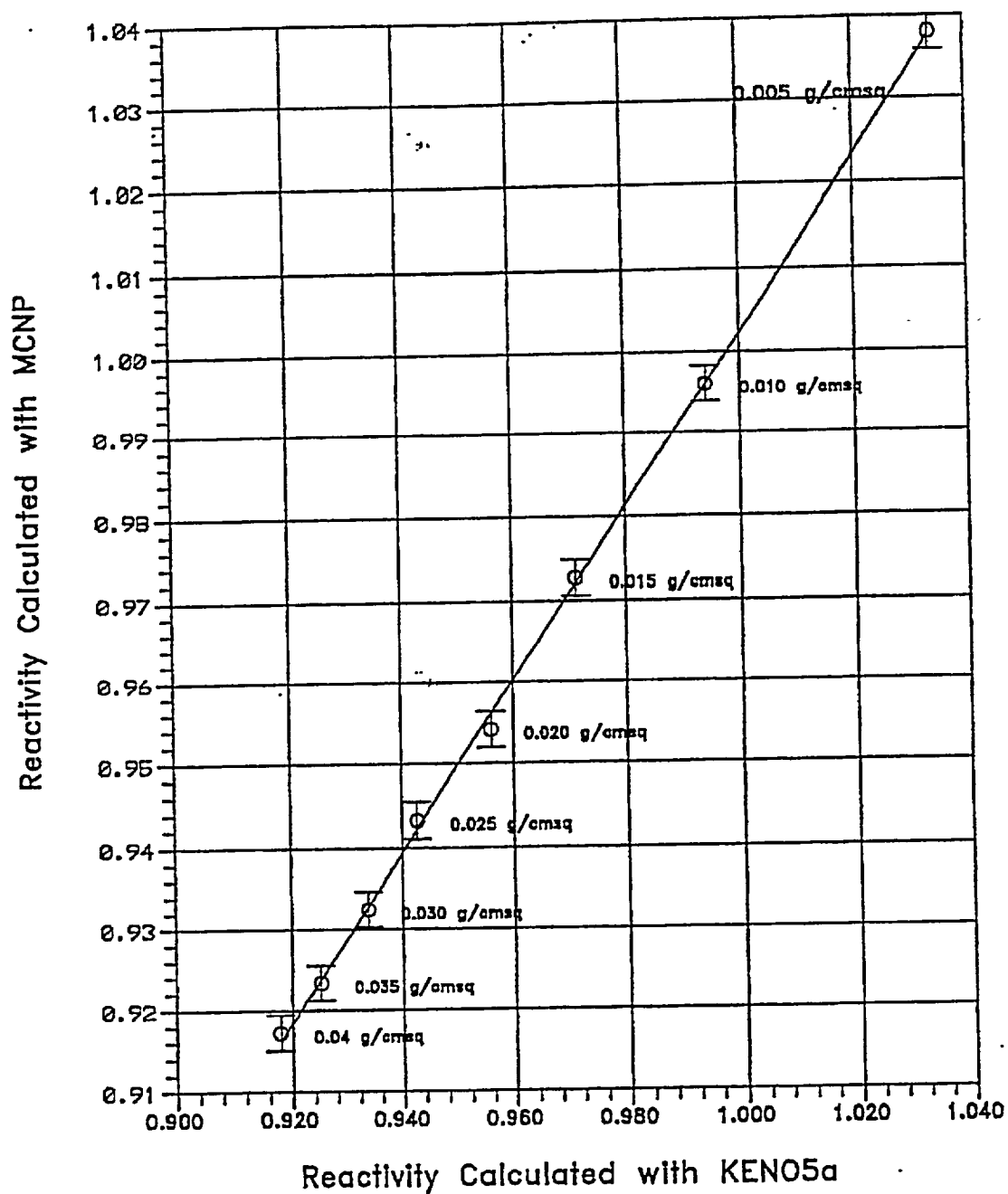


FIGURE 4A.6 COMPARISON OF MCNP AND KENO5a CALCULATIONS FOR VARIOUS BORON-10 AREAL DENSITIES

5.0 THERMAL-HYDRAULIC CONSIDERATIONS

5.1 Introduction

This section provides a summary of the analyses performed to demonstrate the compliance of the unit spent fuel pools (SFPs) and their attendant cooling systems with the provisions of USNRC Standard Review Plan (SRP) 9.1.3 (Spent Fuel Pool Cooling and Cleanup System, Rev. 1, July 1981) and Section III of the USNRC "OT Position Paper for Review and Acceptance of Spent Fuel Storage and Handling Applications," (April 14, 1978). Similar methods of thermal-hydraulic analysis have been used in the licensing evaluations for other SFP capacity expansion projects.

The thermal-hydraulic qualification analyses for the expanded rack array may be broken down into the following categories:

- i. Evaluation of the maximum SFP bulk temperatures for the design-basis offload scenarios, to establish that maximum bulk temperature limits are not exceeded.
- ii. Evaluation of loss-of-forced cooling scenarios, to establish minimum times to boil and to perform corrective actions, and the associated makeup water requirements.
- iii. Determination of the maximum local water temperature, at the instant when the bulk temperature reaches its maximum value, to establish that localized boiling in the fuel storage racks is not possible while forced cooling is operating.
- iv. Evaluation of the maximum fuel rod cladding temperature, at the instant when the bulk temperature reaches its maximum value, to establish that nucleate boiling is not possible while forced cooling is operating.

The following sections present plant system descriptions, analysis methodologies and assumptions, a synopsis of the input data employed and summaries of the calculated results.

5.2 Cooling Systems Description

The SFPCS design basis for both units requires that the system must maintain the SFP bulk temperature below 150°F under the following conditions:

- During routine (non-offload) operation
- Following a normal partial core offload, with one cooling pump operating (assuming a single pump failure)
- Following a full core offload, with both cooling pumps operating (no single failure assumed)

The SFP decay heat load is greater during core offload conditions than during non-offload conditions. Therefore, the peak SFP temperature during routine operation was not evaluated, because it is bounded by the peak SFP temperatures occurring during core offload conditions.

The Unit 1 SFPCS consists of two parallel cooling pumps discharging to a single shell and tube heat exchanger. SFP water is circulated through the heat exchanger tubes and heat is transferred to component cooling water circulating through the shell side. For determining the peak SFP temperature on a partial core offload, a single pump failure is taken that reduces the SFPCS flow to one operating pump and the common heat exchanger. No pump failure is assumed for the full core offload.

The Unit 2 SFPCS consists of two parallel cooling pumps discharging to a common header which supplies two parallel heat exchangers. SFP water is circulated through the tubes and heat is transferred to component cooling water circulating through the shell side. For determining the peak SFP temperature on a partial core offload, a single pump failure is taken that reduces the SFPCS flow to one operating pump and one heat exchanger. No pump failure is assumed for the full core offload.

In addition to the three design basis conditions above, the condition of a full core offload with only one cooling pump available was also evaluated to determine the peak SFP temperature that could occur with minimum cooling. This evaluation provides a bounding value for the peak SFP temperature for a cooling condition beyond the SFPCS design basis.

The normal partial core offload condition with one operating pump is referred to as Scenario 1 in the following section. A full core offload with both cooling pumps operating is referred to as Scenario 2 and a full core offload with one cooling pump operating is referred to as Scenario 3.

5.3 Offload/Cooling Alignment Scenarios

Three offload scenarios are postulated for each St. Lucie unit. These scenarios are:

Scenario	Offload Type	Number of Assemblies Offloaded	Cooling System Configuration
Unit 1			
1	Partial Core	105	1 pump / 1 HX
2	Full Core	217	2 pumps / 1 HX
3	Full Core	217	1 pump / 1 HX
Unit 2			
1	Partial Core	105	1 pump / 1 HX
2	Full Core	217	2 pumps / 2 HXs
3	Full Core	217	1 pump / 1 HX

Scenario 1

A partial core offload is comprised of 105 assemblies offloaded into the SFP, completely filling all available storage locations. The minimum decay time of the previously offloaded fuel assemblies for this offload scenario is 18 months. A cooling alignment that includes the effects of a single active SFPCS component failure (i.e., pump failure) is considered.

Scenario 2

A full core offload is comprised of 217 assemblies offloaded into the SFP, completely filling all available storage locations. The 217 offloaded assemblies are separated into three distinct groups: 73 assemblies with 4.5 years of irradiation at full power, 72 assemblies with 3 years of irradiation at full power and 72 assemblies with 1.5 years of irradiation at full power. The minimum decay time of the previously offloaded fuel assemblies for this scenario is 18 months. Scenario 2 assumed maximum cooling is available with flow from both pumps to all available heat exchangers (1 HX on Unit 1 and 2 HXs on Unit 2). No component failures are assumed.

Scenario 3

Scenario 3 is identical to Scenario 2 except for the number of operating pumps (one instead of two). For both units, Scenario 3 assumes only one HX is supplied by the operating pump.

The core offload time for all scenarios on both units is 120 hours after reactor shutdown. The offload rate is assumed to be instantaneous to maximize decay heat, except for Unit 2 full core offload Scenario 3, which assumes an offload rate of 8 assemblies per hour.

Each of these offload/cooling scenarios is evaluated to determine the peak SFP bulk temperature.

One additional cooling condition was also evaluated beyond the above three scenarios, for the sole purpose of determining a worst-case decay heat load that would be imposed on the SFP and the resultant maximum bulk temperature with one cooling pump operating. This limiting cooling condition is a full core offload required 90 days after a refueling outage. The condition assumes a batch of 72 assemblies is offloaded from the reactor during refueling. After restart and 90 days at power, the full core of 217 assemblies is offloaded to the SFP starting at 72 hours after reactor shutdown, completely filling all available storage locations. One SFPCS pump is operating throughout the transient evaluation.

Tables 5.3.1 and 5.3.2 present the historic and projected offload schedules used for these analyses for Units 1 and 2, respectively.

5.4 Maximum Pool Bulk Temperatures

In this section, we present the methodology for calculating the maximum SFP bulk temperatures for the scenarios presented in the preceding section.

The following conservatisms are applied in the maximum SFP bulk temperature calculations:

- The reactor thermal power level is increased by 2% to account for the plant's reactor thermal power calorimetric uncertainty.
- Appropriate parameters (i.e., burnup, batch size, assembly uranium weight and initial enrichment) are used for all projected offloads.
- The thermal performance of the SFPCS heat exchanger(s) is determined with all heat transfer surfaces fouled to their design-basis maximum levels.
- The thermal performance of the SFPCS heat exchanger(s) is determined incorporating a 5% tube plugging allowance.
- The thermal inertia (thermal capacity) of the SFP is based on the net water volume only. This conservatively neglects the considerable thermal inertia of the fuel assemblies, stainless steel racks and stainless steel SFP liners.

The transient thermal response of the SFP and the attendant cooling systems is governed by a first-order, ordinary differential equation. The governing differential equation can be written by utilizing conservation of energy as:

$$C \frac{dT}{d\tau} = Q(\tau) - Q_{HX}(T) - Q_{ENV}(T) \quad (5-1)$$

where:

C = SFP thermal capacity, Btu/°F

T = SFP bulk temperature, °F

τ = Time after reactor shutdown, hr

$Q(\tau)$ = Time varying decay heat generation rate, Btu/hr

$Q_{HX}(T)$ = Temperature dependent SFPCS heat rejection rate, Btu/hr

$Q_{ENV}(T)$ = Temperature dependent passive heat loss to the environment, Btu/hr

$Q_{HX}(T)$ in Equation 5-1 is a function of the SFP bulk temperature and the coolant water flow rate and temperature, and can be written in terms of the temperature effectiveness (p) as follows:

$$Q_{HX}(T) = W_t C_t p (T - t_i) \quad (5-2)$$

where:

W_t = Coolant water flow rate, lb/hr

C_t = Coolant water specific heat capacity, Btu/(lb-°F)

p = SFPCS heat exchanger(s) temperature effectiveness

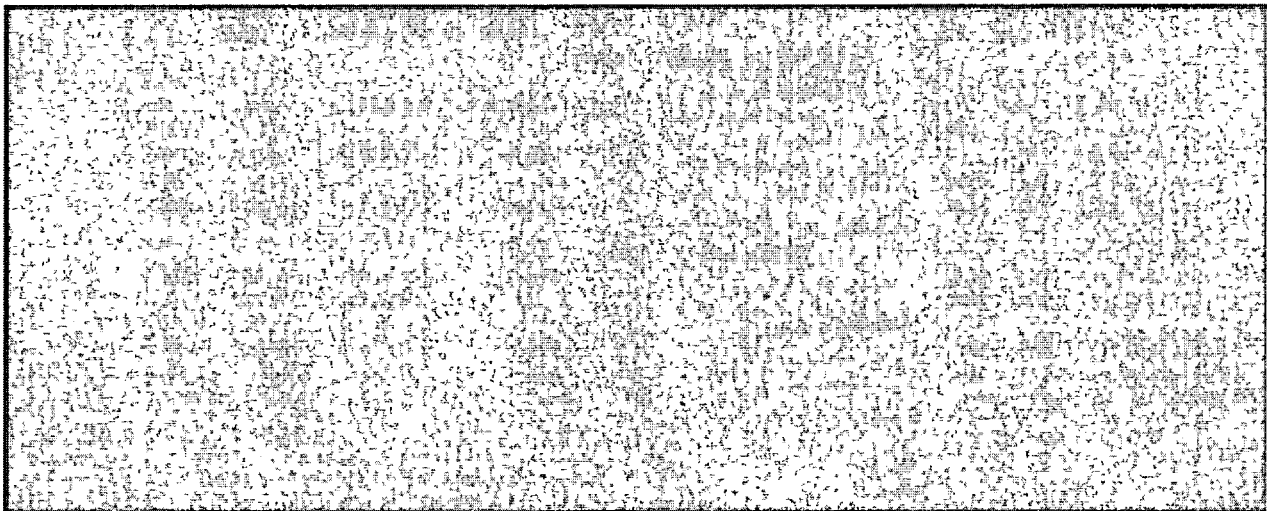
T = SFP bulk water temperature, °F

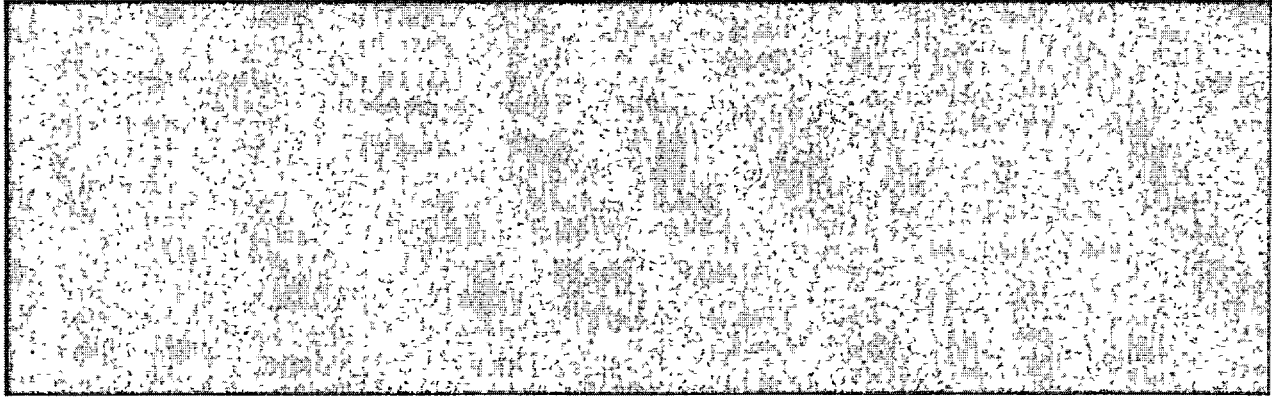
t_i = Coolant water inlet temperature, °F

The temperature effectiveness, a measure of the heat transfer efficiency of the heat exchanger(s), is defined as:

$$p = \frac{t_o - t_i}{T - t_i} \quad (5-3)$$

where t_o is the coolant outlet temperature (°F) and all other terms are as defined above. The SFPCS heat exchanger(s) coolant outlet temperature (t_o) for various SFP bulk temperatures (T) are determined using the Holtec QA validated computer program STER [5.4.7].





The differential equation that defines the transient thermal response of the SFP (Equation 5-1) is solved numerically. The decay heat load from previously offloaded fuel assemblies is assumed to be constant and is calculated using Holtec's QA validated LONGOR computer program [5.4.3]. This program incorporates the ORIGEN2 computer code [5.4.4] to perform the decay heat calculations. The transient decay heat loads and SFP bulk temperatures are calculated using Holtec's QA validated BULKTEM computer program [5.4.5], which also incorporates the ORIGEN2 computer code. The maximum SFP bulk temperatures are extracted from the results of the transient evaluations. The major input values for these analyses are summarized in Table 5.4.1.

As the SFP temperature exceeds the building ambient temperature, both heat and moisture are rejected from the surface to the SFP into the building air. Equation 5-4 utilizes the temperature of the air directly above the SFP to calculate the heat removed from the SFP by passive mechanisms. The following enthalpy and moisture balance equations govern the interaction between heat and moisture rejection at the SFP surface and absorption by the air:

$$\begin{aligned}
 m_{oad}h_{oad} + m_{oaw}h_{oaw} + Q_{sens} + m_{evap}h_{evap} &= m_{bad}h_{bad} + m_{baw}h_{baw} \\
 m_{oaw} + m_{evap} &= m_{baw}
 \end{aligned}
 \tag{5-5}$$

where:

m_{oad} = Mass flow rate of incoming dry air, lb/hr

h_{oad} = Enthalpy of incoming dry air, Btu/lb

m_{oaw} = Mass flow rate of incoming water vapor, lb/hr

h_{oaw} = Enthalpy of incoming water vapor, Btu/lb

Q_{sens} = Sensible heat transferred from SFP, Btu/hr
 m_{evap} = Mass flow rate from surface of SFP, lb/hr
 h_{evap} = Enthalpy of evaporated pool water, Btu/lb
 m_{bad} = Mass flow rate of dry air above SFP, lb/hr
 h_{bad} = Enthalpy of dry air above SFP, Btu/lb
 m_{baw} = Mass flow rate of water vapor above SFP, lb/hr
 h_{baw} = Enthalpy of water vapor above SFP, Btu/lb

To determine bounding maximum values for the temperature of the air directly above the SFP, heat and moisture transfer rates from the surface of the SFP with SFP temperatures in excess of the expected maximum bulk temperatures are calculated using Equation 5-4. Equation 5-5 is then used to determine the enthalpies of the dry air and water vapor directly above the SFP, which are subsequently used to determine the corresponding temperature. As the SFP bulk temperatures will actually be lower than the assumed bounding temperatures, this ensures bounding maximum temperatures for the air directly above the SFP for subsequent use in solving Equation 5-1.

5.5 Minimum Time-to-Boil and Maximum Boiloff Rate

In this section, we present the methodology for calculating the minimum time-to-boil and corresponding maximum boiloff rate for the scenarios presented in Section 5.3.

The following conservatisms and assumptions are applied in the time-to-boil and boiloff rate calculations:

- During the loss of forced cooling evaluations, the makeup water flow is started coincident with the onset of bulk boiling. It is assumed that the temperature of the makeup water added to the SFP is 100°F.
- The loss of forced cooling is assumed to occur coincident with the peak SFP bulk temperature. Maximizing the initial temperature will conservatively minimize the calculated time-to-boil.

- The passive heat losses from the SFP surface to the building air are evaluated assuming the relative humidity of the building air is 100%. This minimizes the evaporation driving force and reduces the resulting heat losses.
- The thermal inertia (thermal capacity) of the SFP is based on the net water volume only. This conservatively neglects the considerable thermal inertia of the fuel assemblies, stainless steel racks and stainless steel SFP liners.

The governing enthalpy balance equation for this condition, subject to these conservative assumptions, can be written as:

$$C(\tau) \frac{dT}{d\tau} = Q(\tau + \tau_0) - Q_{ENV}(T) \quad (5-6)$$

where:

$C(\tau)$ = Time-varying SFP thermal capacity
 τ = Time after cooling is lost (hr)
 τ_0 = Loss of cooling time after shutdown (hr)

All other terms in this equation are the same as defined for Equation 5-1 in Section 5.4.

Equation 5-6 is solved using a numerical solution technique to obtain the bulk pool temperature as a function of time. The time-to-boil, boil-off rate and water depth versus time are calculated using Holtec's QA validated TBOIL program [5.4.6]. Calculations also determined the makeup water flow rate, at the onset of bulk boiling, necessary to maintain a minimum of 9' of above the stored spent fuel. The SFP decay heat loads for these analyses are extracted from the results of the BULKTEM transient evaluations. The major input values for these analyses are summarized in Table 5.5.1.

5.6 Maximum SFP Local Water Temperature

In this section, a summary of the methodology for evaluating the maximum local water temperatures within the fuel racks in the SFP and cask pit is presented. The results of these evaluations are maximum local water temperatures.

In order to determine an upper bound on the maximum local water temperature, a series of conservative assumptions are made. The most important of these assumptions are:

- The walls and floor of the SFP and cask pit are all modeled as adiabatic surfaces, thereby neglecting conduction heat loss through these items.
- Heat losses by thermal radiation and natural convection from the hot SFP surface to the environment are neglected.
- No downcomer flow is assumed to exist between the rack modules in the Unit 1 SFP.
- The hydraulic resistance of every fuel storage rack cell is determined based on the most hydraulically limiting (i.e., highest hydraulic resistance) fuel assembly type.
- The hydraulic resistance parameters for the rack cells, permeability and inertial resistance, are conservatively adjusted by 10%.
- The bottom plenum heights used in the model are less than the actual heights.
- The hydraulic resistance of every fuel storage rack cell is determined based on the most restrictive water inlet geometry of the cells over rack support pedestals (i.e., all baseplate holes are completely blocked). These cells have a reduced water entrance area, caused by the pedestal blocking the baseplate hole, and a correspondingly increased hydraulic resistance.
- The hydraulic resistance of every fuel storage rack cell includes the effects of blockage due to an assumed dropped fuel assembly lying horizontally on top of the racks.
- For the Unit 1 CFD model, the fuel assemblies with the highest decay heat generation rates are grouped together in the center of the model. This conservatively maximizes the distance between these highest heat fuel assemblies and the rack-to-wall downcomers, so the cooled water from the SFPCS must travel the farther along the SFP floor to cool them. Discharge of these assemblies into any rack locations that are closer to a downcomer, including the cask pit rack, is bounded by the analyzed configuration.

To demonstrate adequate cooling of hot fuel in the SFP and the cask pit, it is necessary to rigorously quantify the coupled velocity and temperature fields created by the interaction of buoyancy driven and forced water flows. A Computational Fluid Dynamics (CFD) analysis for this demonstration is required. The objective of this study is to demonstrate that the thermal-hydraulic criterion of ensuring local subcooled conditions in the SFP is met for all postulated fuel

offload/cooling alignment scenarios. The local thermal-hydraulic analysis is performed such that partial cell blockage and slight fuel assembly variations are bounded. An outline of the CFD approach is described in the following.

There are several significant geometric and thermal-hydraulic features of the St. Lucie SFPs that need to be considered for a rigorous CFD analysis. From a fluid flow modeling standpoint, there are two regions to be considered. One region is the SFP bulk region where the classical Navier-Stokes equations [5.6.1] are solved, with turbulence effects included. The other region is the fuel storage racks containing heat generating fuel assemblies, located near the bottom of the SFP. In this region, water flow is directed vertically upwards due to buoyancy forces through relatively small flow channels formed by rods of the fuel assemblies in each rack cell. This situation is modeled as a porous solid region with pressure drop in the flowing fluid governed by Darcy's Law as:

$$\frac{\partial P}{\partial X_i} = -\frac{\mu}{K(i)} V_i - C \rho |V| \frac{V_i}{2} \quad (5-7)$$

where $\partial P/\partial X_i$ is the pressure gradient, $K(i)$, V_i and C are the corresponding permeability, velocity and inertial resistance parameters and μ is the fluid viscosity. These terms are added to the classic Navier-Stokes equations. The permeability and inertial resistance parameters for the rack cells loaded with fuel assemblies are determined based on friction factor correlations for the laminar flow conditions that would exist due to the low buoyancy induced velocities and the small size of the flow channels.

The St. Lucie SFP geometries require an adequate portrayal of both large scale and small scale features, spatially distributed heat sources in the racks and water inlet/outlet piping. Relatively cooler bulk water normally flows down between the fuel racks outline and wall liner, a clearance known as the downcomer. Near the bottom of the racks the flow turns from a vertical to horizontal direction into the bottom plenum, supplying cooling water to the rack cells. Heated water issuing out of the top of the racks mixes with the bulk water. An adequate modeling of

these features on the CFD program involves meshing the large scale bulk SFP region and small scale downcomer and bottom plenum regions with sufficient number of computational cells to capture both the global and local features of the flow field.

The distributed heat sources in the racks are modeled by identifying distinct heat generation zones considering recently offloaded fuel, bounding peaking effects, and the presence of background decay heat from previous offloads. Three heat generating zones are identified. The first consists of background fuel from previous offloads. The second and third zones consist of fuel from recently offloaded fuel assemblies. The two recent offload zones are differentiated by one zone with higher than average decay (hottest partial core offload batch of 73 assemblies) heat generation and the other with less than average decay heat generation (remainder of full core). This is a conservative model, since all of the fuel with higher than average decay heat is placed in a contiguous area. A uniformly distributed heat generation rate was applied throughout each distinct zone (i.e., there were no variations in heat generation rate within a single zone).

The CFD analysis was performed on the commercially available FLUENT [5.6.2] computational fluid dynamics program, which has been benchmarked under Holtec's QA program. The FLUENT code enables buoyancy flow and turbulence effects to be included in the CFD analysis. Buoyancy forces are included by specifying a temperature-dependent density for water and applying an appropriate gravity vector. Turbulence effects are modeled by relating time-varying Reynolds' Stresses to the mean bulk flow quantities with the standard k- ϵ turbulence model.

For Unit 1, the cask pit is actually a region within the rectangular SFP, but is separated from the SFP by a partial-height steel wall. Because the Unit 1 cask pit is not hydraulically isolated from the rest of the SFP, the entire SFP is modeled and evaluated. This model contains all of the fuel regions (i.e., hotter than average full core, cooler than average full core and background) discussed above.

For Unit 2, the cask pit is a completely separate body that is hydraulically connected to the rest of the SFP via a narrow fuel transfer slot. Because the Unit 2 cask pit is hydraulically isolated from the rest of the SFP, only the cask pit and the connecting slot are modeled with the temperature at the SFP end of the slot set equal to the SFP bulk temperature. The decay heat load in the rack in this cask pit is determined with fuel assemblies cooled for at least 18-months. Freshly discharged fuel cannot be placed in this rack.

Some of the major input values for this analysis are summarized in Table 5.6.1. Isometric views of the assembled CFD models for the St. Lucie units are presented in Figures 5.6.1 and 5.6.2.

5.7 Fuel Rod Cladding Temperature

In this section, the method to calculate the temperature of the fuel rod cladding is presented. As previously stated in Section 5.1, the maximum fuel rod cladding temperature is determined to establish that nucleate boiling is not possible while forced cooling is operating. This requires demonstrating that the highest fuel rod cladding temperatures are less than the local saturation temperature of the adjacent SFP water. The maximum fuel cladding superheat above the local water temperature is calculated for two different peak fuel rod heat emission rates.

A fuel rod can produce F_z times the average heat emission rate over a small length, where F_z is the axial peaking factor. The axial heat distribution in a rod is generally a maximum in the central region, and tapers off at its two extremities. Thus, peak cladding heat flux over an infinitesimal rod section is given by the equation:

$$q_c = \frac{Q \times F_z}{A_c} \quad (5-8)$$

where Q is the rod average heat emission and A_c is the total cladding external heat transfer area in the active fuel length region. The axial peaking factor is obtained by dividing the total peaking factor by the assembly peaking factor, both given in Table 5.6.1.

As described previously, the maximum local water temperature was computed. Within each fuel assembly sub-channel, water is continuously heated by the cladding as it moves axially upwards under laminar flow conditions. Rohsenow and Hartnett [5.7.1] report a Nusselt-number for laminar flow heat transfer in a heated channel. The film temperature driving force (ΔT_f) at the peak cladding flux location is calculated as follows:

$$\Delta T_f = \frac{q_c}{h_f} \quad (5-9)$$

$$h_f = \text{Nu} \frac{K_w}{D_h}$$

where h_f is the waterside film heat transfer coefficient, D_h is the sub-channel hydraulic diameter, K_w is the water thermal conductivity and Nu is the Nusselt number for laminar flow heat transfer.

In order to introduce some additional conservatism in the analysis, we assume that the fuel cladding has a crud deposit resistance R_c (equal to $0.0005 \text{ ft}^2\text{-hr-}^\circ\text{F/Btu}$) which covers the entire surface. Thus, including the temperature drop across the crud resistance, the cladding to water local temperature difference (ΔT_c) is given by the equation $\Delta T_c = \Delta T_f + R_c \times q_c$.

5.8 Results

This section contains results from the analyses performed for the postulated offload scenarios.

5.8.1 Maximum Pool Bulk Temperatures

For the offload/cooling scenarios described in Section 5.3, the maximum calculated bulk temperatures are summarized in Table 5.8.1. Given the conservatisms incorporated into the calculations, actual bulk temperatures will be lower than these calculated values. Figures 5.8.1

through 5.8.6 each present profiles of net decay heat load, passive heat losses and bulk temperature versus time for the evaluated transient scenarios.

The results presented in Table 5.8.1 demonstrate that calculated bulk temperatures for all scenarios other than Scenario 3 for each unit remain below the allowable bulk temperature limit. Table 5.8.1 provides the results of the bulk temperature evaluations for each unit. The maximum bulk temperature, the time after reactor shutdown that the maximum temperature is reached and the coincident net heat load are given for three core offload scenarios.

Scenarios 1 and 2:

The results presented in Table 5.8.1 demonstrate that the maximum calculated bulk temperatures for a partial core offload with one SFPCS pump (Scenario 1) and for a full core offload with two SFPCS pumps (Scenario 2) remain well below the allowable SFP bulk temperature limit of 150°F. Therefore, the SFP cooling system design basis is satisfied under maximum fuel assembly loading conditions with the new cask pit racks installed.

Scenario 3:

Scenario 3 is a full core offload with one SFPCS pump operating, a cooling scenario that is beyond the design basis for the SFP cooling system. For this abnormal condition, the bounding peak SFP temperature reaches approximately 161°F for Unit 1 and 166°F for Unit 2. These results demonstrate that no SFP boiling will occur under worst-case core offload conditions, provided at least one SFPCS cooling pump is available.

Scenario 4:

The evaluation concluded that the highest SFP bulk temperature for this “accident full core offload” scenario was 172°F on Unit 1 and 179°F on Unit 2. This demonstrates that no pool boiling will occur with one operating cooling pump for the worst-case decay heat load imposed on either unit's SFP.

5.8.2 Minimum Time-to-Boil and Maximum Boiloff Rate

For the offload/cooling described in Section 5.3, the calculated times-to-boil and maximum boil-off rates are summarized in Table 5.8.2. Given the conservatisms incorporated into the calculations, actual times-to-boil will be higher than these calculated values and actual boil-off rates will be lower than calculated.

5.8.3 Local Water and Fuel Cladding Temperatures

Consistent with our approach to make conservative assessments of temperature, the local water temperature calculations are performed for an SFP with a total decay heat generation equal to the calculated decay heat load coincident with the maximum SFP bulk temperature for Scenario 3. Thus, the local water temperature evaluation is a calculation of the temperature increment over the theoretical spatially uniform value due to local hot spots (due to the presence of highly heat emissive fuel assemblies). As described in Subsection 5.7, the peak fuel clad superheats (i.e., the maximum clad-to-local water temperature difference) are determined for two peak fuel rod heat emission levels. The resultant bounding superheat values were used to calculate bounding maximum fuel clad temperatures.

The numeric results of the maximum local water temperature and the bounding fuel cladding temperature evaluations are presented in Table 5.8.3. Figure 5.8.7 presents converged temperature contours in a vertical slice through the hot fuel region of the Unit 1 SFP. Figures 5.8.8 and 5.8.9, respectively, presents converged temperature contours and velocity vectors in a vertical slice through the center of the cask pit and slot.

The maximum local water is lower than the 240°F local boiling temperature at the top of the racks. The critical heat flux required for Departure from Nucleate Boiling (DNB) to occur is approximately 10^6 W/m². However, the maximum heat flux from the hottest rod is only about

5400 W/m². These results demonstrate that boiling, including nucleate boiling on clad surfaces, cannot occur.

5.9 References

- [5.4.1] "Heat Loss to the Ambient from Spent Fuel Pools: Correlation of Theory with Experiment", Holtec Report HI-90477, Revision 0, April 3, 1990.
- [5.4.2] "An Improved Correlation for Evaporation from Spent Fuel Pools", Holtec Report HI-971664, Revision 0.
- [5.4.3] "QA Documentation for LONGOR," Holtec Report HI-951390, Revision 0.
- [5.4.4] A.G. Croff, "ORIGEN2 - A Revised and Updated Version of the Oak Ridge Isotope Generation and Depletion Code," ORNL-5621, Oak Ridge National Laboratory, 1980.
- [5.4.5] "QA Documentation for BULKTEM," Holtec Report HI-951391, Revision 1.
- [5.4.6] "QA Documentation for TBOIL," Holtec Report HI-92832, Revision 5.
- [5.4.7] "QA Documentation for STER", Holtec Report HI-92776, Revision 11.
- [5.6.1] Batchelor, G.K., "An Introduction to Fluid Dynamics", Cambridge University Press, 1967.
- [5.6.2] "Validation of FLUENT Version 5.5", Holtec Report HI-2012642, Revision 0.
- [5.7.1] Rohsenow, N.M., and Hartnett, J.P., "Handbook of Heat Transfer", McGraw Hill Book Company, New York, 1973.

Table 5.3.1					
Historic and Projected Fuel Offload Schedule – Unit 1					
End-of-Cycle Number	Offload Date	Number of Assemblies	Average Burnup (MWd/MTU)	Initial ²³⁵ U Enrichment (wt.%)	Assembly ²³⁵ U Weight (kgU)
Previously Discharged Assemblies					
1	3/28/1978	52	13,239	1.948	396.884
2	4/1/1979	68	22,487	2.289	371.938
3	3/28/1980	88	28,111	2.703	375.866
4	9/11/1981	64	30,122	2.920	387.633
5	2/27/1983	87	32,760	2.970	380.742
6	10/23/1985	85	37,075	3.222	378.462
7	2/7/1987	84	38,253	3.552	372.521
8	7/11/1988	83	39,181	3.538	370.963
9	1/22/1990	101	35,795	3.355	373.567
10	10/18/1991	84	38,107	3.514	373.112
11	3/31/1993	84	40,374	3.615	371.897
12	10/26/1994	84	36,952	3.293	383.019
13	4/29/1996	88	38,399	3.470	397.328
14	10/20/1997	63	34,161	3.124	398.425
15	9/13/1999	89	40,136	3.668	396.868
16	4/9/2001	97	56,100	3.843	396.168
17	9/13/2002	105	56,100	4.50	380
18	3/13/2004	105	56,100	4.50	380
19	9/13/2005	105	56,100	4.50	380
20	3/13/2007	105	56,100	4.50	380
21	9/13/2008	105	56,100	4.50	380
Recently Discharged Assemblies					
partial core	3/13/2010	105	56,100	4.50	380
full core	3/13/2010	73	56,100	4.50	380
		72	50,490		
		72	42,075		

Table 5.3.2 Historic and Projected Fuel Offload Schedule – Unit 2					
End-of-Cycle Number	Offload Date	Number of Assemblies	Average Burnup (MWd/MTU)	Initial ²³⁵ U Enrichment (wt.%)	Assembly ²³⁵ U Weight (kgU)
Previously Discharged Assemblies					
1	10/12/1984	80	12,832	1.773	387.248
2	4/5/1986	84	27,165	2.356	363.215
3	10/2/1987	72	34,035	2.977	380.255
4	1/31/1989	84	39,568	3.563	378.352
5	9/30/1990	76	40,258	3.448	380.525
6	4/26/1992	68	44,186	3.586	382.636
7	3/31/1994	80	44,977	3.905	382.946
8	10/8/1995	84	44,776	3.995	379.540
9	4/14/1997	64	46,144	3.817	379.052
10	11/9/1998	64	46,629	3.716	383.701
11	4/25/2000	77	59,160	4.189	391.774
12	05/9/2000	105	59,160	4.50	380
13	11/9/2001	105	59,160	4.50	380
14	05/9/2003	105	59,160	4.50	380
15	11/9/2004	105	59,160	4.50	380
16	05/9/2006	105	59,160	4.50	380
17	11/9/2007	105	59,160	4.50	380
18	05/9/2009	105	59,160	4.50	380
19	11/9/2010	105	59,160	4.50	380
20	05/9/2012	105	59,160	4.50	380
21	11/9/2013	105	59,160	4.50	380
Recently Discharged Assemblies					
partial core	15/9/2015	105	59,160	4.50	380
full core	15/9/2015	73	59,160	4.50	380
		72	53,244		
		72	44,370		

TABLE 5.4.1 Key Input Data for Bulk Temperature Evaluation		
Parameter	Unit 1 Value	Unit 2 Value
Number of Storage Cells in SFP	1,849	1,809
Maximum Refueling Batch Size	105 assemblies	105
Reactor Thermal Power		
Current	2,700 MW(t)	2,700 MW(t)
Up rated	2,916 MW(t)	2,916 MW(t)
Reactor Thermal Power Uncertainty	2%	2%
Reactor Core Size	217 assemblies	217 assemblies
Bounding Maximum Inlet CCW Temperature	100°F	100°F
SFPCS HX Coolant Flow Rate	2850 gpm	2850 gpm
SFP Water Flow to SFPCS HX		
One Operating Pump	2000 gpm	1746 gpm
Two Operating Pumps	3000 gpm	1368 gpm
Minimum In-Core Hold Time	120 hrs	120 hrs
Minimum Fuel Assembly Transfer Rate		
Partial Core	Instantaneous	Instantaneous
Full Core without Active Failure	Instantaneous	Instantaneous
Full Core with Single Active Failure	Instantaneous	8 per hour

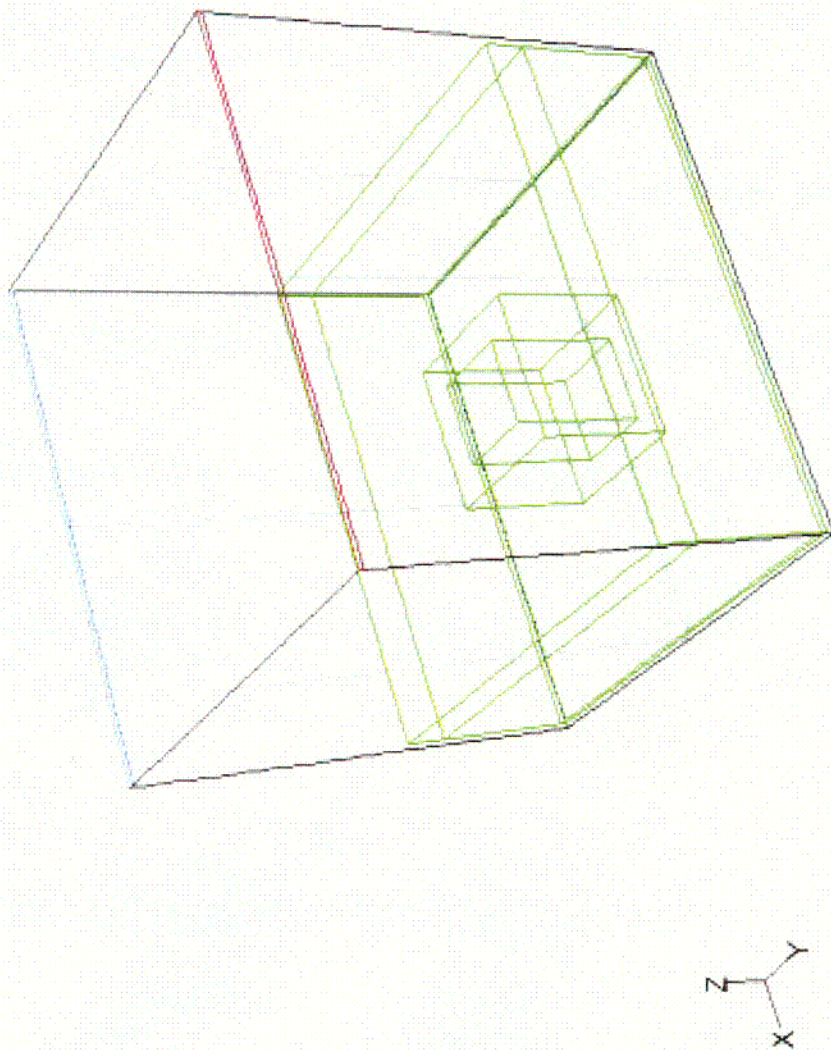
Table 5.5.1 Key Input Data for Time-To-Boil Evaluation		
Parameter	Unit 1 Value	Unit 2 Value
SFP Surface Area	1221 ft ²	1194 ft ²
Minimum Pool Water Depth	38 feet and 4 inches	38 feet
Fuel Racks Displaced Volume	853 ft ³	856 ft ³
Fuel Assemblies Displaced Volume	6,257 ft ³	6,121 ft ³
SFP Net Water Volume	39,480 ft ³	44,307 ft ³

Table 5.6.1 Key Input Data for Local Temperature Evaluation		
Parameter	Unit 1 Value	Unit 2 Value
Assembly Peaking Factor	1.65	1.75
Total Peaking Factor	2.80	3.09
Cooled SFP Water Flow Rate through SFPCS Heat Exchanger(s)	1×10^6 lb/hr	Not Applicable
Hydraulically Limiting Fuel Assembly	Combustion Engineering 16x16	Combustion Engineering 16x16
Fuel Rod Outer Diameter	0.382 inches	0.382 inches
Active Fuel Length	134 inches	134 inches
Number of Rods per Assembly	236 rods	236 rods
Rack Cell Inner Dimension	8.58 inches	8.58 inches
Rack Cell Length	180 inches	180 inches
Modeled Bottom Plenum Height	3 inches	5 inches

Table 5.8.1 Result of Transient Bulk Temperature Evaluations			
Scenario	Maximum Bulk Temperature (°F)	Time After Reactor Shutdown (hrs)	Coincident Net Heat Load (Btu/hr)
Unit 1 Results			
1 - Partial Core	134.47	137	21.31×10^6
2 - Full Core	125.01	128	39.38×10^6
3 - Full Core	161.19	137	37.17×10^6
Unit 2 Results			
1 - Partial Core	139.58	140	22.20×10^6
2 - Full Core	142.87	133	39.81×10^6
3 - Full Core	165.89	159	36.30×10^6

Table 5.8.2 Results of Loss-of-Forced Cooling Evaluations			
Scenario	Minimum Time-to-Boil	Maximum Boiloff Rate	Makeup Water Rate to Maintain 9' of Water Above Fuel
Unit 1 Results			
Partial Core	9.39 hrs	45.98 gpm	28 gpm
Full Core	3.33 hrs	76.23 gpm	52 gpm
Unit 2 Results			
Partial Core	9.42 hrs	44.98 gpm	30 gpm
Full Core	3.10 hrs	84.74 gpm	54 gpm

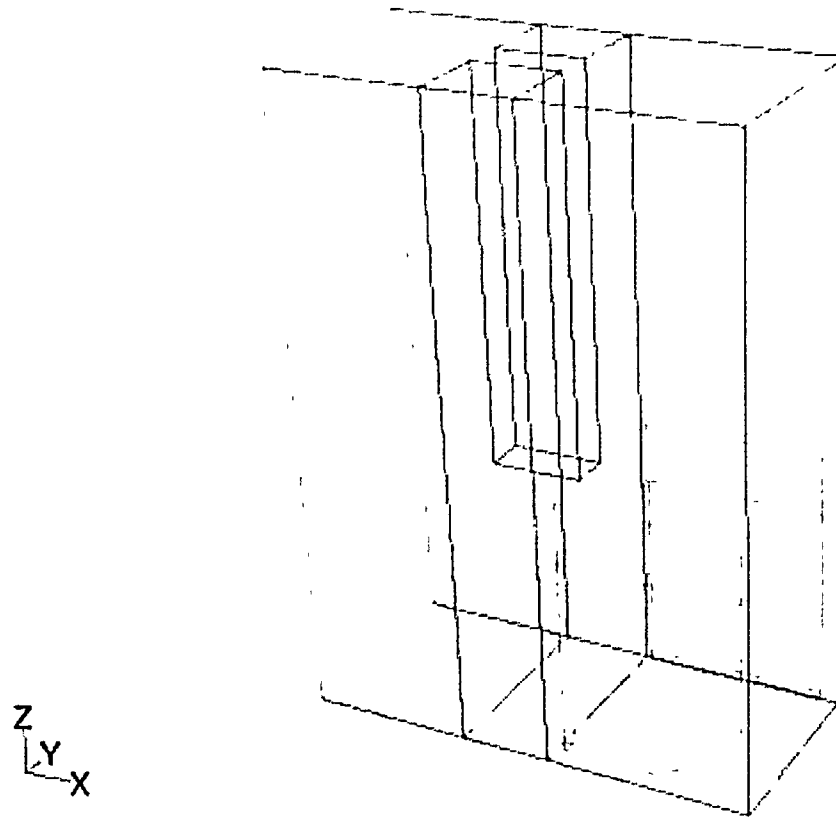
Table 5.8.3 Results of Maximum Local Water and Fuel Cladding Temperature Evaluations			
	Maximum Local Water Temp. (°F)	Bounding Fuel Clad Superheat (°F)	Bounding Fuel Clad Temperature (°F)
Unit 1	190.0	51.96	241.96
Unit 2	189.1	3.25	192.35



Grid

Jan 18, 2002
FLUENT 5.5 (3d, segregated, ke)

Figure 5.6.1 – Unit 1 CFD Model Isometric View



Grid

Jun 27, 2002
FLUENT 5.5 (3d, segregated, ke)

Figure 5.6.2 – Unit 2 CFD Model Isometric View

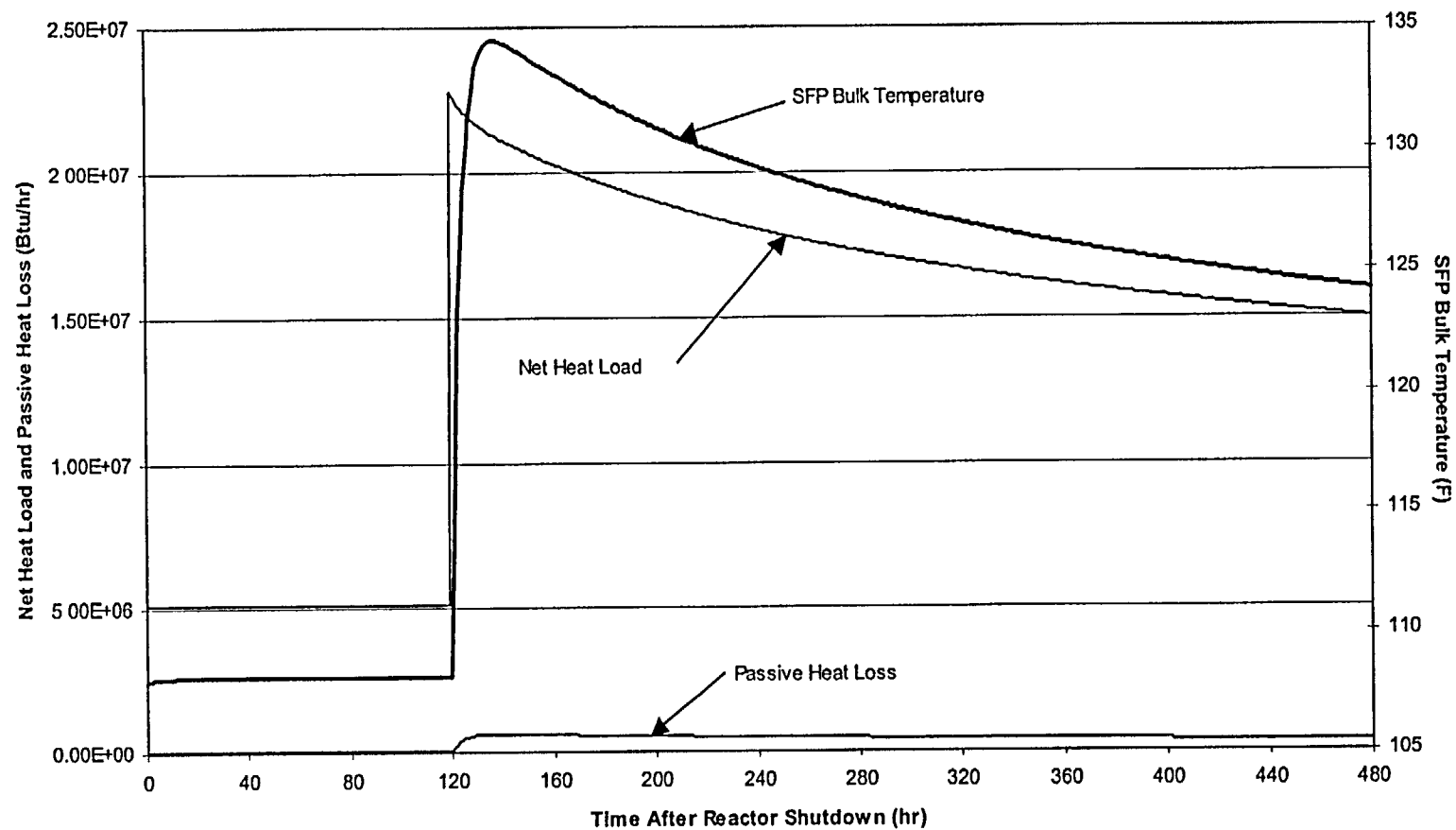


Figure 5.8.1 – Unit 1 Scenario 1 – Partial Core Discharge with Coincident Single Active Failure

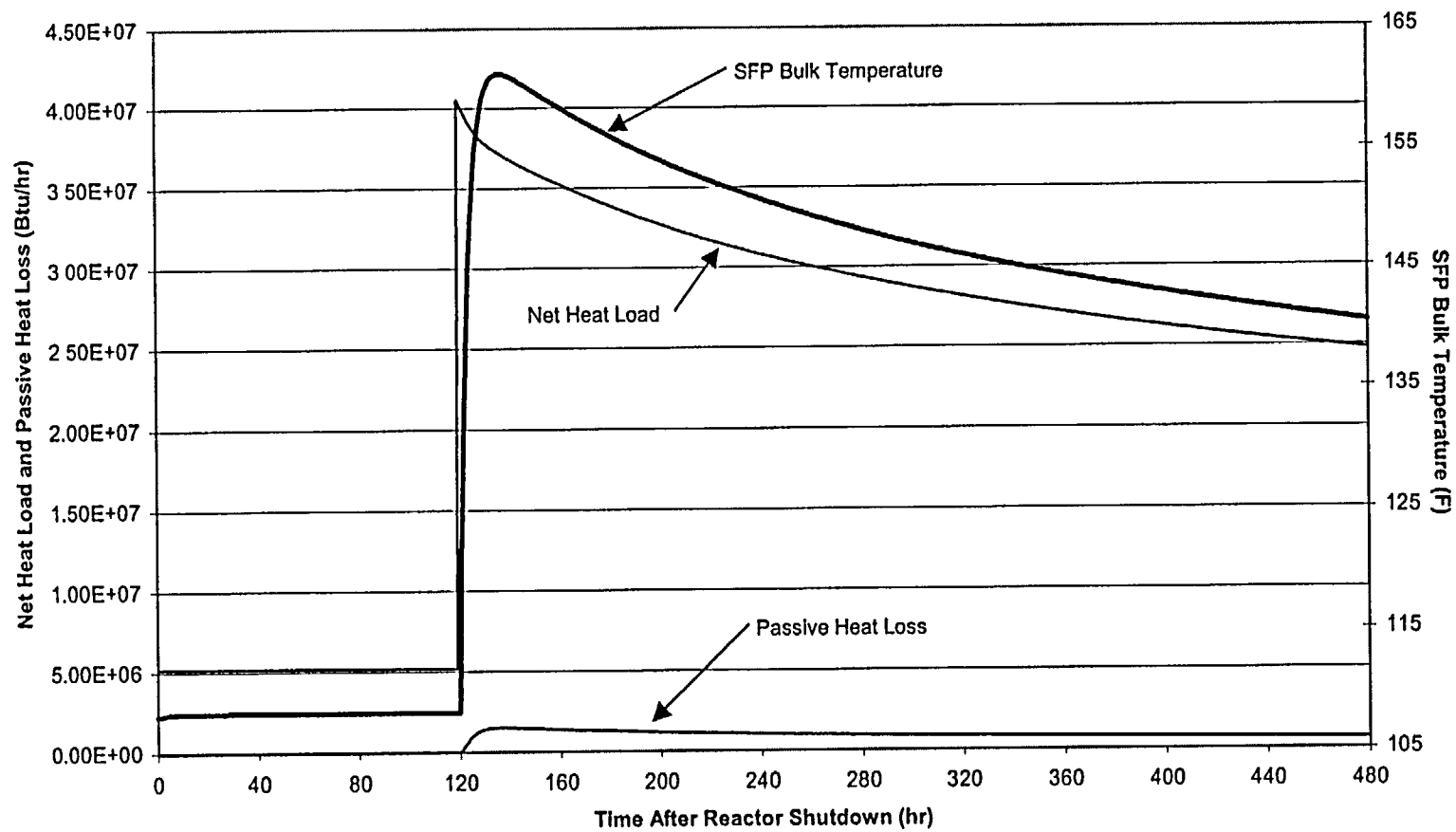


Figure 5.8.2 – Unit 1 Scenario 2a – Full Core Discharge with Coincident Single Active Failure

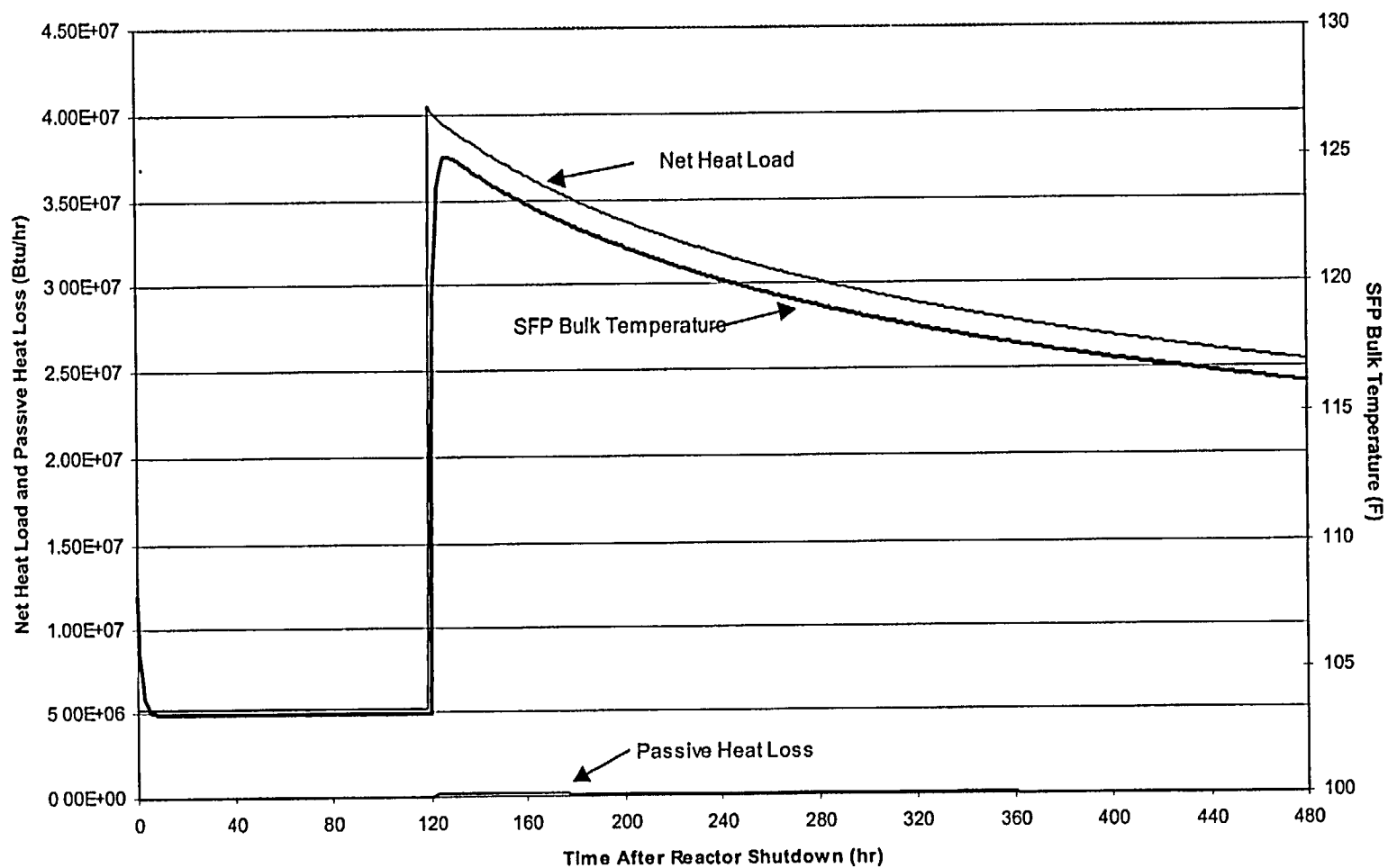


Figure 5.8.3 – Unit 1 Scenario 2b – Full Core Discharge without Coincident Single Active Failure

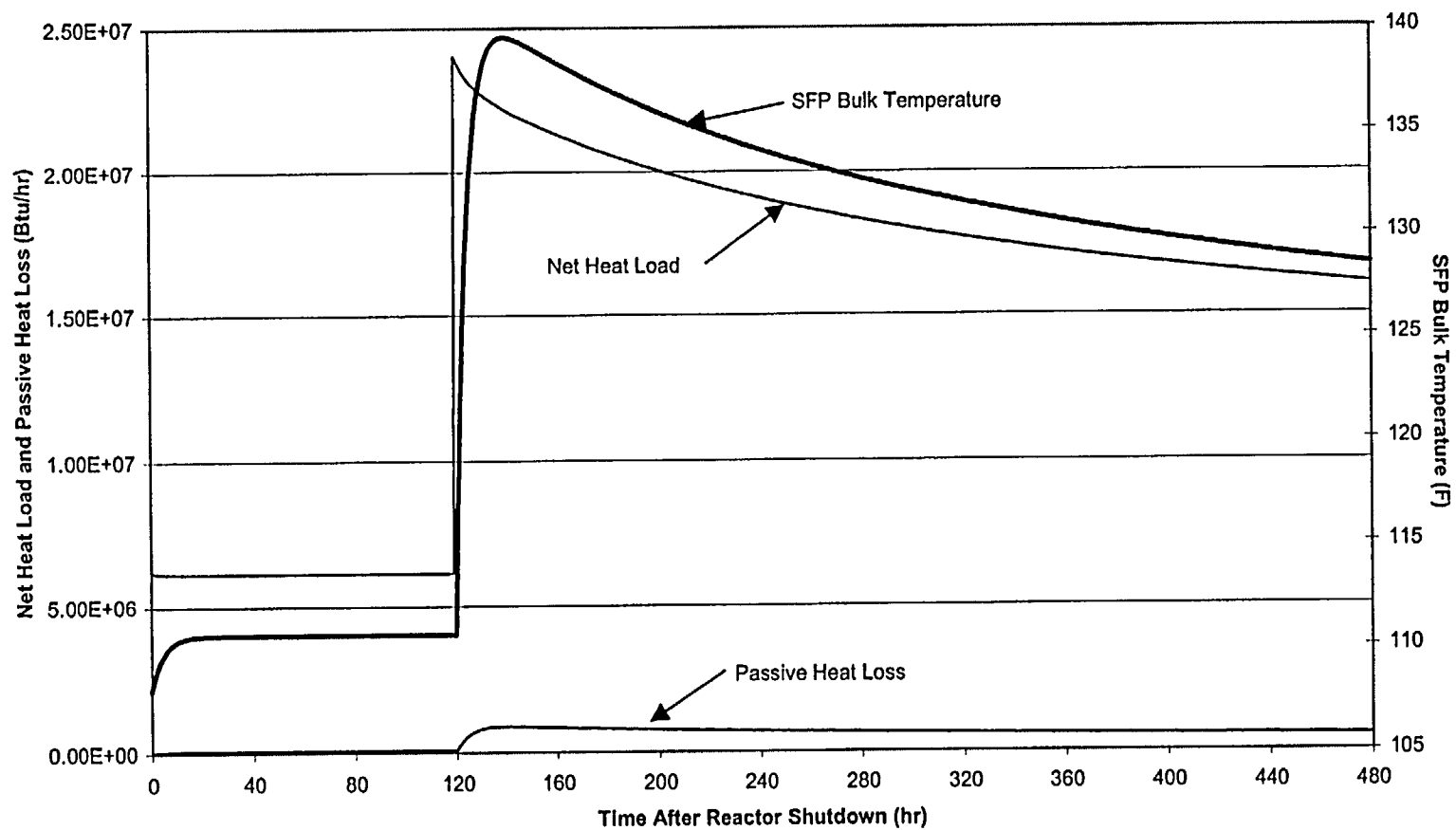


Figure 5.8.4 – Unit 2 Scenario 1 – Partial Core Discharge with Coincident Single Active Failure

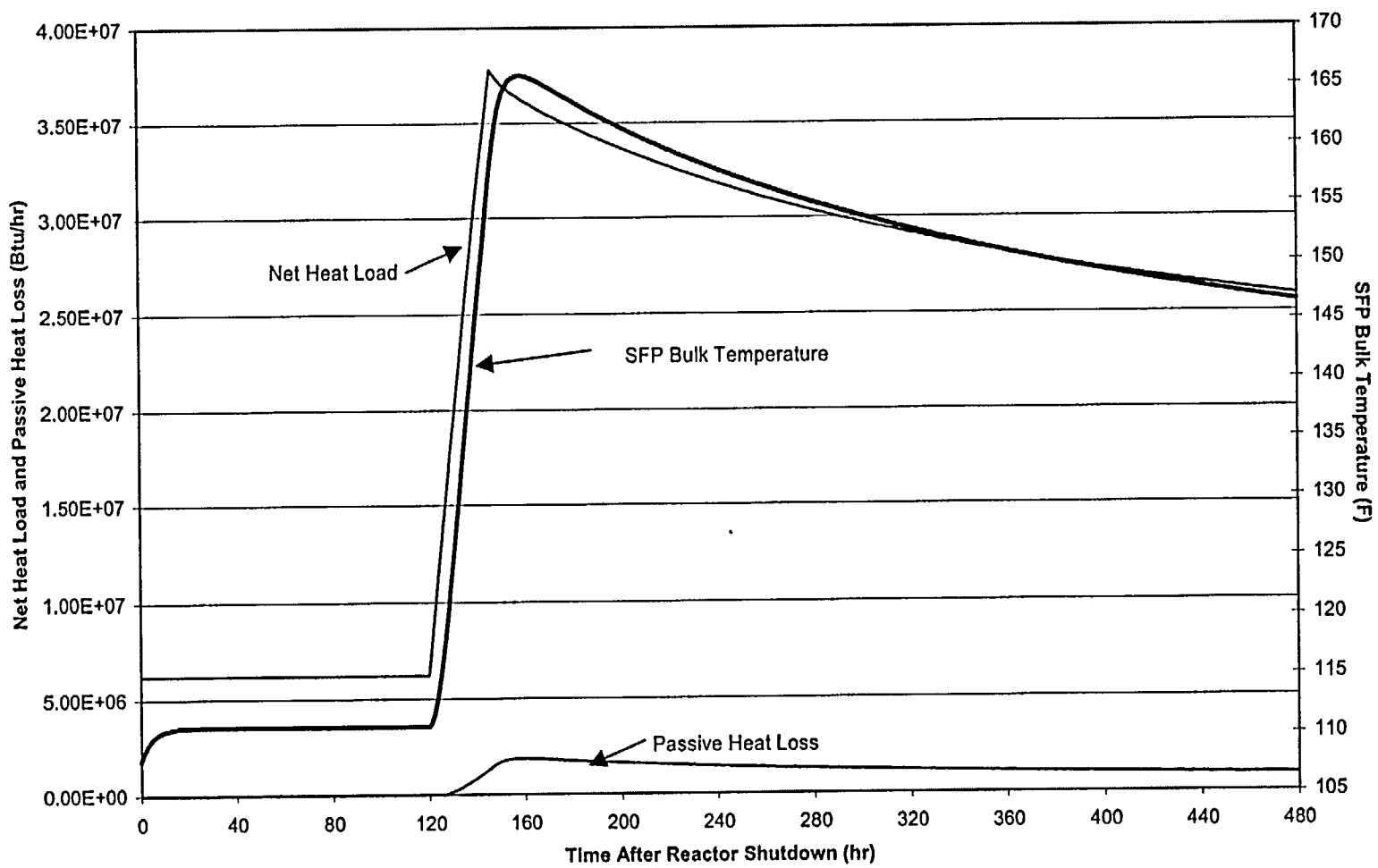


Figure 5.8.5 – Unit 2 Scenario 2a – Full Core Discharge with Coincident Single Active Failure

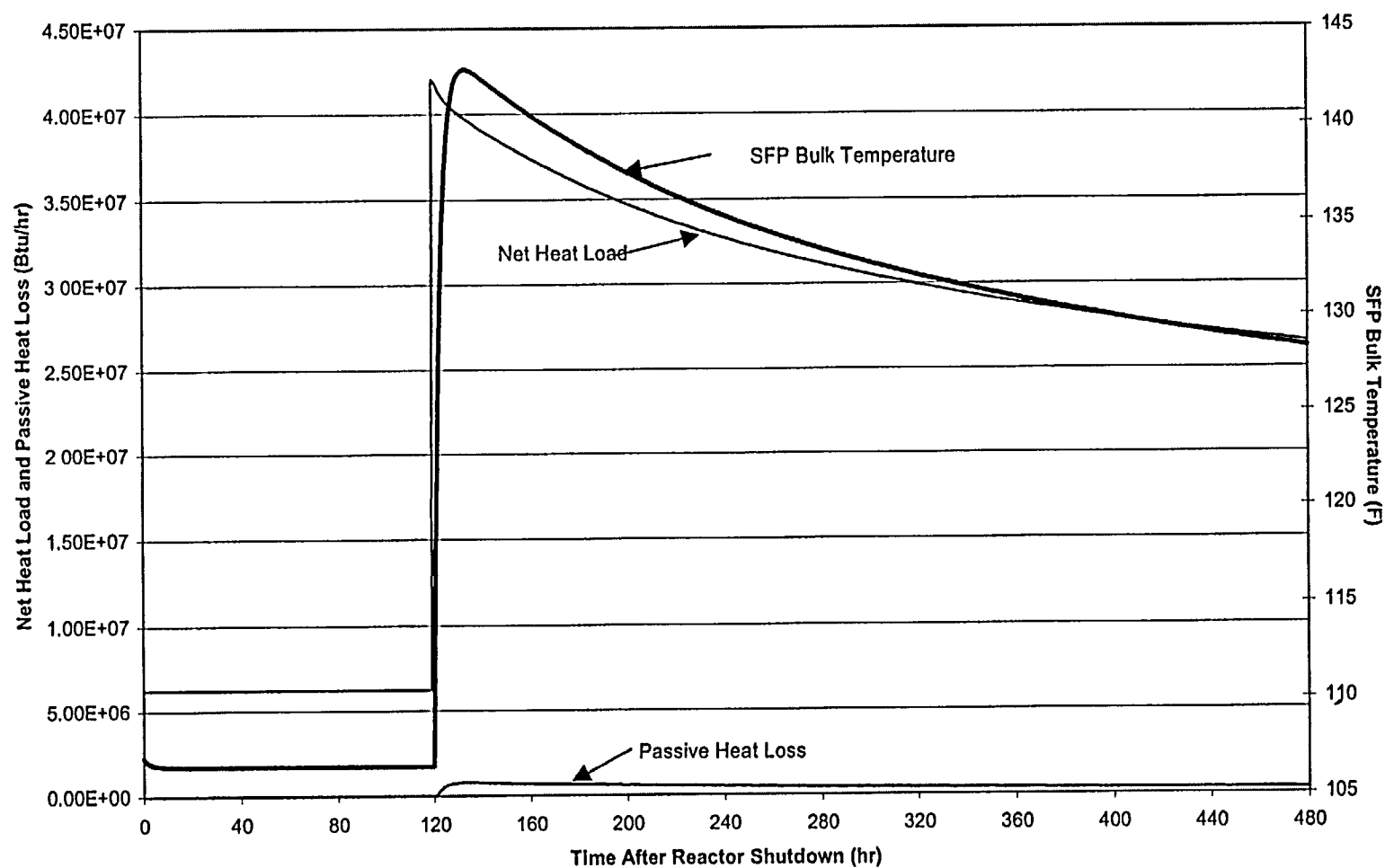
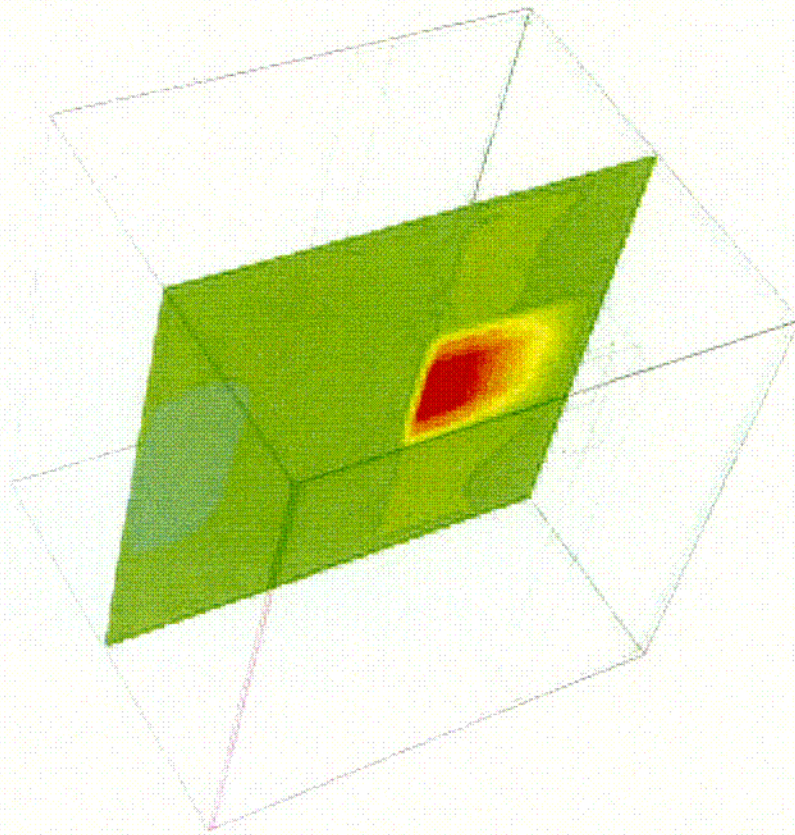
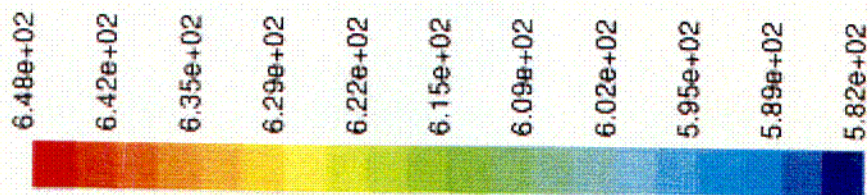


Figure 5.8.6 – Unit 2 Scenario 2b – Full Core Discharge without Coincident Single Active Failure



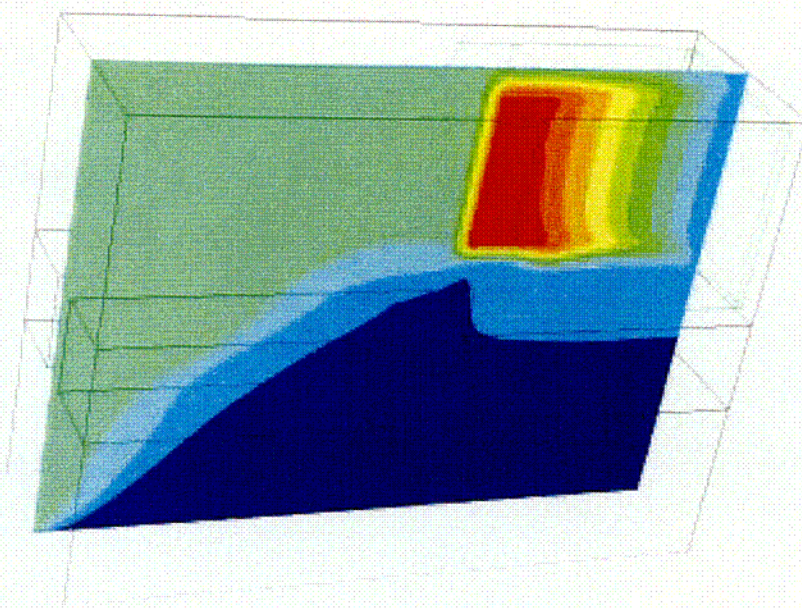
Contours of Static Temperature (r)

Aug 08, 2002
FLUENT 5.5 (3d, segregated, ke)

Figure 5.8.7 – Unit 1 CFD Model with Converged Temperature Contours

3.61e+02
3.60e+02
3.60e+02
3.59e+02
3.59e+02
3.58e+02
3.58e+02
3.57e+02
3.57e+02
3.56e+02
3.56e+02

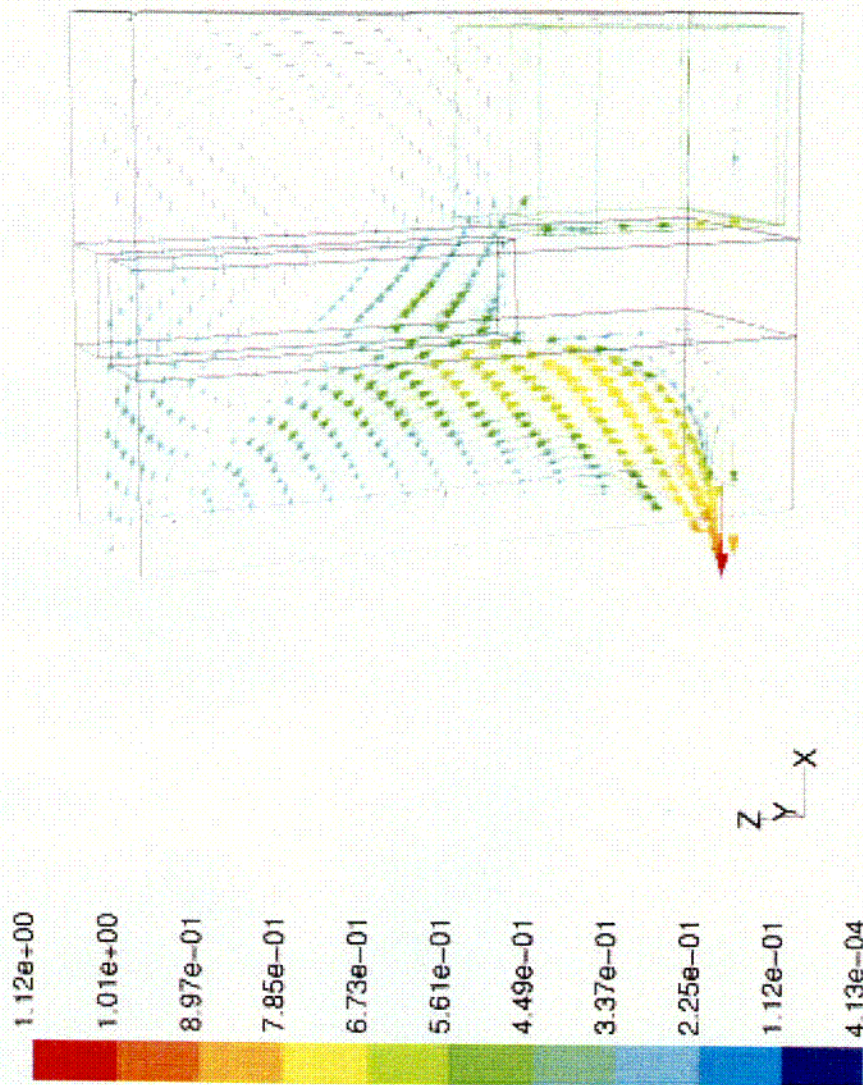
Z
Y
X



Contours of Static Temperature (K)

Jun 27, 2002
FLUENT 5.5 (3d, segregated, ke)

Figure 5.8.8 – Unit 2 CFD Model with Converged Temperature Contours



Velocity Vectors Colored By Velocity Magnitude (ft/s)

FLUENT 5.5 (3d, segregated, ke)

Aug 22, 2002

Figure 5.8.9 – Unit 2 CFD Model with Converged Velocity Vectors

6.0 STRUCTURAL/SEISMIC CONSIDERATIONS

6.1 Introduction

This section considers the structural adequacy of the new fuel racks in each of the Plant St. Lucie Cask Pit Areas under all loads postulated for normal, seismic, and accident conditions. The analyzed storage rack configurations for Unit 1 and Unit 2 are depicted in Figures 1.1.1 and 1.1.2, respectively.

The analyses undertaken to confirm the structural integrity of the racks are performed in compliance with the USNRC Standard Review Plan [6.1.1] and the OT Position Paper [6.1.2]. For each of the analyses, an abstract of the methodology, modeling assumptions, key results, and summary of parametric evaluations are presented. Delineation of the relevant criteria is discussed in the text associated with each analysis.

6.2 Overview of Rack Structural Analysis Methodology

The response of a free-standing rack module to seismic inputs is highly nonlinear and involves a complex combination of motions (sliding, rocking, twisting, and turning), resulting in impacts and friction effects. Some of the unique attributes of the rack dynamic behavior include a large fraction of the total structural mass in a confined rattling motion, friction support of rack pedestals against lateral motion, and large fluid coupling effects due to deep submergence and independent motion of closely spaced adjacent structures.

Linear methods, such as modal analysis and response spectrum techniques, cannot accurately simulate the structural response of such a highly nonlinear structure to seismic excitation. An accurate simulation is obtained only by direct integration of the nonlinear equations of motion with the three pool slab acceleration time-histories applied as the forcing functions acting simultaneously.

The DYNARACK solver [6.2.4] is the vehicle utilized in this project to simulate the dynamic behavior of the complex storage rack structures. The following sections provide the basis for this selection and discussion on the development of the methodology.

6.2.1 Background of Analysis Methodology

Reliable assessment of the stress field and kinematic behavior of the rack modules calls for a conservative dynamic model incorporating all *key attributes* of the actual structure. This means that the model must feature the ability to execute the concurrent motion forms compatible with the free-standing installation of the modules. The model must possess the capability to effect momentum transfers which occur due to rattling of fuel assemblies inside storage cells and the capability to simulate lift-off and subsequent impact of support pedestals with the rack platform. The contribution of the water mass in the interstitial spaces around the rack modules and within the storage cells must be modeled in an accurate manner, since erring in quantification of fluid coupling on either side of the actual value is no guarantee of conservatism.

The Coulomb friction coefficient at the pedestal-to-rack platform interface may lie in a rather wide range and a conservative value of friction cannot be prescribed *a priori*. In fact, a perusal of results of rack dynamic analyses in numerous docket (Table 6.2.1) indicates that an upper bound value of the coefficient of friction often maximizes the computed rack displacements as well as the equivalent elastostatic stresses.

In short, there are a large number of parameters with potential influence on the rack kinematics. The comprehensive structural evaluation must deal with all of these without sacrificing conservatism.

Briefly, the 3-D rack model dynamic simulation, involving one or more spent fuel racks, handles the array of variables as follows:

Interface Coefficient of Friction: Parametric runs are made with upper bound and lower bound values of the coefficient of friction. The limiting values are based on experimental data which have been found to be bounded by the values 0.2 and 0.8. Simulations are also performed with the array of pedestals having randomly chosen coefficients of friction in a Gaussian distribution with a mean of 0.5 and lower and upper limits of 0.2 and 0.8, respectively. In the fuel rack simulations, the Coulomb friction interface

between rack support pedestal and rack platform is simulated by piecewise linear (friction) elements. These elements function only when the pedestal is physically in contact with the platform.

Rack Beam Behavior: Rack elasticity, relative to the rack base, is included in the model by introducing linear springs to represent the elastic bending action, twisting, and extensions.

Impact Phenomena: Compression-only gap elements are used to provide for opening and closing of interfaces such as the pedestal-to-rack platform interface, and the fuel assembly-to-cell wall interface. These interface gaps are modeled using nonlinear spring elements. The term "nonlinear spring" is a generic term used to denote the mathematical representation of the condition where a restoring force is not linearly proportional to displacement.

Fuel Loading Scenarios: The fuel assemblies are conservatively assumed to rattle in unison, which obviously exaggerates the contribution of impact against the cell wall.

Fluid Coupling: Holtec International extended Fritz's classical two-body fluid coupling model to multiple bodies and utilized it to perform the first two-dimensional multi-rack analysis (Diablo Canyon, ca. 1987). Subsequently, laboratory experiments were conducted to validate fluid coupling theory. This technology was incorporated in the computer code DYNARACK [6.2.4]. This development was first utilized in Chinshan, Oyster Creek, and Shearon Harris plants [6.2.1, 6.2.3] and, subsequently, in numerous other rerack projects. Despite the fact that the analyses for this project require the simulation of only one rack, the DYNARACK code, is used for this project.

6.3 Description of Racks

Rack material is defined in Table 6.3.1.

As may be seen in the rack layouts provided in Figures 1.1.1 and 1.1.2, the nominal distance between the side of the Unit 1 rack and the walls is approximately 4" in the N-S direction and approximately 6" in the E-W direction, and the nominal distance between the side of the Unit 2 rack and the walls in each

direction is approximately 9". The dimensions are chosen to ensure that the rack is centered within the Cask Pit. During rack installation, these dimensions will be met to the extent possible, considering rack and wall straightness and leveling tolerances. The walls and distances separating the Cask Pit Area from the Spent Fuel Pool will effectively eliminate fluid coupling between the proposed rack in each Unit and the racks in the adjacent SFP. The excitation of the proposed racks will be primarily dependent on the motion of the floor and walls of the Cask Pit. The independence of motion of the proposed racks from the racks located in the adjacent SFP allows single rack analysis to produce accurate predictions of the rack motion during dynamic simulations.

The Cartesian coordinate system utilized within the rack dynamic model has the following nomenclature:

- x = Horizontal axis along plant East
- y = Horizontal axis along plant North
- z = Vertical axis upward from the rack base

6.3.1 Fuel Weights

The dry fuel weight for Unit 1 is 1328 lbs. However, for the Unit 1 dynamic rack simulations, a higher fuel weight value of 1423 lbs is used to account for control components being stored along with every fuel assembly. This slightly higher weight is conservative, since it is unlikely that every location in the Cask Pit rack will contain a control element assembly (CEA) stored integrally with a fuel assembly. The dry fuel weight for Unit 2 is 1325 lbs. However, for the Unit 2 dynamic rack simulations, a higher fuel weight value of 1384 lbs is used to account for control components being stored along with fuel assemblies. The actual maximum weight of a fuel assembly plus CEA is 1410 lbs. However, this represents an increase of less than 3% over the value used in the evaluations and the analyses conservatively consider the increased weight in the assemblies at every location. Given the small weight difference and large margins of safety in the design, restrictions on CEA storage are not warranted for Unit 2.

6.4 Synthetic Time-Histories

The synthetic time-histories in three orthogonal directions (N-S, E-W, and vertical) are generated in accordance with the provisions of SRP 3.7.1 [6.4.1]. For Unit 1 the structural damping is taken to be 2% for both OBE and SSE, and for Unit 2 the structural damping is taken to be 2% for OBE and 3% for SSE, based on the FSAR for the respective Units. The mass of the model is comprised primarily of the fuel assemblies, which rattle within the storage cells during the seismic event. This rattling behavior, and the associated friction between model components, warrants use of the damping factors associated with bolted and riveted assemblies.

In order to prepare an acceptable set of acceleration time-histories, Holtec International's proprietary code GENEQ [6.4.2] is utilized.

A preferred criterion for the synthetic time-histories in SRP 3.7.1 calls for both the response spectrum and the power spectral density corresponding to the generated acceleration time-history to envelope their target (design basis) counterparts with only finite enveloping infractions. The time-histories for the pools have been generated to satisfy this preferred criterion. The seismic files also satisfy the requirements of statistical independence mandated by SRP 3.7.1.

Figures 6.4.1 through 6.4.12 provide plots of the time-history accelerograms, which were generated for 20-second duration OBE and SSE events. These artificial time-histories are used in all non-linear dynamic simulations of the racks.

Results of the correlation function of the three time-histories are given in Tables 6.4.1 and 6.4.2. Absolute values of the correlation coefficients are shown to be less than 0.15, indicating that the desired statistical independence of the three data sets has been met.

6.5 Modeling Methodology

Recognizing that the analysis work effort must deal with both stress and displacement criteria, the sequence of model development and analysis steps that are undertaken are summarized in the following:

- a. Prepare 3-D dynamic rack models suitable for a time-history analysis. Include all fluid coupling interactions and mechanical coupling appropriate to performing an accurate non-linear simulation.
- b. Perform 3-D dynamic analyses on various physical conditions (such as coefficient of friction and extent of cells containing fuel assemblies). Archive appropriate displacement and load outputs from the dynamic model for post-processing.
- c. Perform stress analysis of high stress areas for the limiting case of all the rack dynamic analyses. Demonstrate compliance with ASME Code Section III, Subsection NF limits on stress and displacement.

6.5.1 Model Details for Spent Fuel Racks

The dynamic modeling of the rack structure is prepared with special consideration of all nonlinearities and parametric variations. Particulars of modeling details and assumptions for the analysis of racks are given in the following:

6.5.1.1 Model Details and Assumptions

- a. The fuel rack structure motion is captured by modeling the rack as a 12 degree-of-freedom structure. Movement of the rack cross-section at any height is described by six degrees-of-freedom of the rack base and six degrees-of-freedom at the rack top. In this manner, the response of the module, relative to the baseplate, is captured in the dynamic analyses once suitable springs are introduced to couple the rack degrees-of-freedom and simulate rack stiffness.
- b. Rattling fuel assemblies within the rack are modeled by five lumped masses located at H, .75H, .5H, .25H, and at the rack base (H is the rack height measured above the baseplate). Each lumped fuel mass has two horizontal displacement degrees-of-freedom. Vertical motion of the fuel assembly mass is assumed equal to rack vertical motion at the baseplate level. The centroid of each fuel assembly mass can be located off-center, relative to the rack structure centroid at that level, to simulate a partially loaded rack.

- c. Seismic motion of a fuel rack is characterized by random rattling of fuel assemblies in their individual storage locations. All fuel assemblies are assumed to move in-phase within a rack. This exaggerates computed dynamic loading on the rack structure and, therefore, yields conservative results.
- d. Fluid coupling between rack and fuel assemblies, and between rack and wall, is simulated by appropriate inertial coupling in the system kinetic energy. Inclusion of these effects uses the methods of References [6.5.2, 6.5.3].
- e. Fluid damping and form drag are conservatively neglected.
- f. Sloshing is found to be negligible at the top of the rack and is, therefore, neglected in the analysis of the rack.
- g. Potential impacts between the cell walls of the new racks and the contained fuel assemblies are accounted for by appropriate compression-only gap elements between masses involved. The possible incidence of rack-to-wall impact is simulated by similar gap elements at the top and bottom of the rack in two horizontal directions. Bottom gap elements are located at the baseplate elevation. The initial gaps reflect the presence of baseplate extensions, and the gap element stiffnesses are chosen to simulate local structural detail.
- h. Pedestals and rack support platforms are modeled by gap elements in the vertical direction and as "rigid links" for transferring horizontal friction forces. Local pedestal vertical spring stiffness accounts for floor elasticity and for local rack elasticity just above the pedestal.
- i. Each pedestal support is linked to the supporting rack platform by two piece-wise linear friction springs. The rack platform is assumed to travel along with the pool liner during seismic events with possible slippage occurring between the support pedestal and the rack platform. The flexibility of the supporting rack platform is also addressed by the evaluation.
- j. Rattling of fuel assemblies inside the storage locations causes the gap between fuel assemblies and cell wall to change from a maximum of twice the nominal gap to a theoretical zero gap. Fluid coupling coefficients are based on the nominal gap in order to provide a conservative measure of fluid resistance to gap closure.
- k. The model for the rack is considered supported, at the base level, on four pedestals modeled as non-linear compression only gap spring elements and eight piecewise linear friction spring elements. These elements are properly located with respect to the centerline of the rack beam, and allow for arbitrary rocking and sliding motions.
- l. The nominal rack to wall dimensions shown in Figures 1.1.1 and 1.1.2 are the gaps surrounding the respective racks at the start of each dynamic simulation.

- m. The racks and support platforms are level and plumb such that the rack-to-wall dimensions are maintained over the rack vertical length).

6.5.1.2 Element Details

Figure 6.5.1 shows a schematic of the dynamic model of the rack. The schematic depicts many of the characteristics of the model including all of the degrees-of-freedom and some of the spring restraint elements.

Table 6.5.1 provides a complete listing of each of the 22 degrees-of-freedom for a rack model. Six translational and six rotational degrees-of-freedom (three of each type on each end) describe the motion of the rack structure. Rattling fuel mass motions (shown at nodes 1*, 2*, 3*, 4*, and 5* in Figure 6.5.1) are described by ten horizontal translational degrees-of-freedom (two at each of the five fuel masses). The vertical fuel mass motion is assumed (and modeled) to be the same as that of the rack baseplate. The five masses are connected to each other by an axially rigid member, which enables the fuel masses to vibrate in unison with the rack in the vertical direction. However, the connecting element has no bending or shear stiffness. Therefore, the masses vibrate independently in the horizontal direction and are driven by the inertia loads and local impact loads. The five fuel masses are connected to the rack model via impact gap elements. Impact loads between the fuel masses and the rack cell wall are obtained upon closure of this gap element. The gap dimensions are determined at each time step by establishing the independent displacements of the fuel masses and the rack geometric centerline displacement corresponding to the same elevation. Therefore, the outer boxes surrounding the fuel masses shown in Figure 6.5.1 depict the inside of the fuel cell.

The assumption of five fuel masses connected to the rack in the horizontal direction by impact gap elements is conservative in several ways. The actual fuel assembly would impact the inside of the cell walls at the rod spacer grid locations. Since there are many more than five grids, the tributary length of fuel assembly associated with each actual grid would be less than that provided by the quarter points associated with only five masses. The masses at each of the nodes of the modeled fuel is much greater than the masses associated with each length of fuel assembly centered on a spacer grid. Therefore, the

resulting dynamic impact forces would be greater. Because of the fact that the fuel masses are connected by an element that has no bending or shear stiffness, the fuel nodes come into contact with the inside of the fuel cell when the rack moves a sufficient distance to close the gap between fuel node and cell node. In other words, the rack walls actually strike and drive the fuel assembly mass during a dynamic event. The rack motion is driven by the pool floor. The inertia of the conservatively modeled masses produce a greater impact force upon closure of the gap element than the smaller inertia of the actual masses associated with each spacer grid.

Each of the five modeled fuel masses contains the mass associated with that respective elevation for every fuel assembly within the storage module. All of the fuel assemblies are modeled as one. Therefore, all of the fuel mass at each elevation behaves in unison and is free to rattle within the cell. This is conservative, since the actual fuel assemblies would rattle within each of the cells in a haphazard fashion. It is unlikely that their combined mass would travel in harmony at any one time.

The stiffness of the fuel assembly-to-cell wall impact gap elements is determined based on an evaluation of the cell wall. The fuel spacer grids are considered rigid in comparison and the flexibility of the grid and fuel rods is not included in these terms. Thus, the stiffness is overestimated and will produce conservatively higher forces. The stiffness is computed using the formula for a plate with diameter equal to the width of the cell that is loaded by uniform pressure.

Figure 6.5.2 depicts the fuel to rack impact springs (used to develop potential impact loads between the fuel assembly mass and rack cell inner walls) in a schematic isometric. Only one of the five fuel masses is shown in this figure. Four compression only springs, acting in the horizontal direction, are provided at each fuel mass.

Figure 6.5.3 provides a 2-D schematic elevation of the storage rack model, discussed in more detail in Section 6.5.3. This view shows the vertical location of the five storage masses and some of the support pedestal spring members.

Figure 6.5.4 shows the modeling technique and degrees-of-freedom associated with rack elasticity. In each bending plane a shear and bending spring simulate elastic effects [6.5.4]. Linear elastic springs coupling rack vertical and torsional degrees-of-freedom are also included in the model.

6.5.2 Fluid Coupling Effect

In its simplest form, the so-called "fluid coupling effect" [6.5.2, 6.5.3] can be explained by considering the proximate motion of two bodies under water. If one body (mass m_1) vibrates adjacent to a second body (mass m_2), and both bodies are submerged in frictionless fluid, then Newton's equations of motion for the two bodies are:

$$(m_1 + M_{11}) A_1 + M_{12} A_2 = \text{applied forces on mass } m_1 + O(X_1^2)$$

$$M_{21} A_1 + (m_2 + M_{22}) A_2 = \text{applied forces on mass } m_2 + O(X_2^2)$$

A_1 , and A_2 denote absolute accelerations of masses m_1 and m_2 , respectively, and the notation $O(X^2)$ denotes nonlinear terms.

M_{11} , M_{12} , M_{21} , and M_{22} are fluid coupling coefficients, which depend on body shape, relative disposition, etc. Fritz [6.5.3] gives data for M_{ij} for various body shapes and arrangements. The fluid adds mass to the body (M_{11} to mass m_1), and an inertial force proportional to acceleration of the adjacent body (mass m_2). Thus, acceleration of one body affects the force field on another. This force field is a function of inter-body gap, reaching large values for small gaps. Lateral motion of a fuel assembly inside a storage location encounters this effect. For example, fluid coupling behavior will be experienced between nodes 2 and 2* in Figure 6.5.1.

The derivation of the fluid coupling matrix [6.5.5] relies on the classical inviscid fluid mechanics principles, namely the principle of continuity and Kelvin's recirculation theorem. While the derivation of the fluid coupling matrix is based on no artificial construct, it has been nevertheless verified by an extensive set of shake table experiments [6.5.5].

6.5.3 Stiffness Element Details

Three element types are used in the rack models. Type 1 elements are linear elastic elements used to represent the beam-like behavior of the integrated rack cell matrix. Type 2 elements are the piece-wise linear friction springs used to develop the appropriate forces between the rack pedestals and the supporting rack platform. Type 3 elements are non-linear gap elements, which model gap closures and subsequent impact loadings (i.e., between fuel assemblies and the storage cell inner walls, and rack outer periphery spaces).

If the simulation model is restricted to two dimensions (one horizontal motion plus one vertical motion, for example), for the purposes of model clarification only, then Figure 6.5.3 describes the configuration. This simpler model is used to elaborate on the various stiffness modeling elements.

Type 3 gap elements modeling impacts between fuel assemblies and racks have local stiffness K_i in Figure 6.5.3. Support pedestal spring rates K_s are modeled by type 3 gap elements. Local compliance of the concrete floor is included in K_s . The type 2 friction elements are shown in Figure 6.5.3 as K_f . The spring elements depicted in Figure 6.5.4 represent type 1 elements.

Friction at support/rack platform interface is modeled by the piecewise linear friction element with a suitably large stiffness value of K_f . This friction element allows load to be increased until the limiting lateral load μN is reached, where μ is the coefficient of friction and N is the current compression load at the interface between support and rack platform. At every time-step during the dynamic simulation, the current value of N (either zero, if the pedestal has lifted off the support platform, or a compressive finite value) is computed.

The gap element K_s , modeling the effective compression stiffness of the structure in the vicinity of the support, includes stiffness of the pedestal, local stiffness of the underlying pool slab, and local stiffness of the rack cellular structure above the pedestal.

The previous discussion is limited to a 2-D model solely for simplicity. Actual analyses incorporate 3-D motions.

6.5.4 Coefficients of Friction

To eliminate the last significant element of uncertainty in rack dynamic analyses, multiple simulations are performed to adjust the friction coefficient ascribed to the pedestal-to-rack platform interface. These friction coefficients are chosen consistent with the two bounding extremes from Rabinowicz's data [6.5.1]. Simulations are also performed by imposing intermediate value friction coefficients developed by a random number generator with Gaussian normal distribution characteristics. The assigned values are then held constant during the entire simulation in order to obtain reproducible results. †Thus, in this manner, the analysis results are brought closer to the realistic structural conditions.

The coefficient of friction (μ) between the pedestal supports and the rack platform is indeterminate. According to Rabinowicz [6.5.1], results of 199 tests performed on austenitic stainless steel plates submerged in water show a mean value of μ to be 0.503 with standard deviation of 0.125. Upper and lower bounds (based on twice standard deviation) are 0.753 and 0.253, respectively. Analyses are therefore performed for coefficient of friction values of 0.2 (lower limit) and for 0.8 (upper limit), and for random friction values clustered about a mean of 0.5. The bounding values of $\mu = 0.2$ and 0.8 have been found to envelope the upper limit of module response in previous rerack projects.

6.5.5 Governing Equations of Motion

Using the structural model discussed in the foregoing, equations of motion corresponding to each degree-of-freedom are obtained using Lagrange's Formulation [6.5.4]. The system kinetic energy includes contributions from solid structures and from trapped and surrounding fluid. The final system of equations obtained have the matrix form:

$$[M] \left[\frac{d^2 q}{dt^2} \right] = [Q] + [G]$$

where:

† It is noted that DYNARACK has the capability to change the coefficient of friction at any pedestal at each instant of contact based on a random reading of the computer clock cycle. However, exercising this option would yield results that could not be reproduced. Therefore, the random choice of coefficients is made only once per run.

- [M] - total mass matrix (including structural and fluid mass contributions). The size of this matrix will be 22 x22.
- q - the nodal displacement vector relative to the pool slab displacement (the term with q indicates the second derivative with respect to time, i.e., acceleration)
- [G] - a vector dependent on the given ground acceleration
- [Q] - a vector dependent on the spring forces (linear and nonlinear) and the coupling between degrees-of-freedom

The above column vectors have a length of 22. The equations can be rewritten as follows:

$$\left[\frac{d^2 q}{dt^2} \right] = [M]^{-1} [Q] + [M]^{-1} [G]$$

This equation set is mass uncoupled, displacement coupled at each instant in time. The numerical solution uses a central difference scheme built into the proprietary computer program DYNARACK [6.2.4].

6.6 Structural Evaluation of Spent Fuel Rack Design

6.6.1 Kinematic and Stress Acceptance Criteria

There are two sets of criteria to be satisfied by the rack modules:

a. Kinematic Criteria

It is not physically possible for the proposed isolated fuel rack situated in the Cask Pit Area to overturn, because of the proximity of the surrounding four walls. The rack-to-wall dimensions would not allow the rack center of gravity to be located over any pedestal(s). Rack overturning could occur only if the relative displacement between the center of gravity and the pedestals is

greater than about one-half the distance between the pedestals, since this will place the center of mass over one pair of pedestals.

According to Ref [6.1.1 and 6.1.2], the minimum required safety margins under the OBE and SSE events are 1.5 and 1.1, respectively. The maximum displacements of the rack (in the two principal axes) are obtained from a post processing of the rack time history response output. The ratio of the displacement required to produce incipient tipping in either principal plane to the actual maximum displacement in that plane from the time history solution is the margin of safety.

All ratios available for the OBE and SSE events should be greater than 1.5 and 1.1, respectively to satisfy the regulatory acceptance criteria. However, in order to be conservative, the worst case displacements from the SSE simulations must ensure a more conservative factor of safety of 1.5.

b. Stress Limit Criteria

Stress limits must not be exceeded under the postulated load combinations provided herein.

6.6.2 Stress Limit Evaluations

The stress limits presented below apply to the rack structure and are derived from the ASME Code, Section III, Subsection NF [6.6.1]. Parameters and terminology are in accordance with the ASME Code. Material properties are obtained from the ASME Code Appendices [6.6.2], and are listed in Table 6.3.1.

(i) Normal and Upset Conditions (Level A or Level B)

- a. Allowable stress in tension on a net section is:

$$F_t = 0.6 S_y$$

Where, S_y = yield stress at temperature, and F_t is equivalent to primary membrane stress.

- b. Allowable stress in shear on a net section is:

$$F_v = .4 S_y$$

- c. Allowable stress in compression on a net section is given by:

$$F_a = S_y \left(.47 - \frac{k \ell}{444 r} \right)$$

where kl/r for the main rack body is based on the full height and cross section of the honeycomb region and does not exceed 120 for all sections.

ℓ = unsupported length of component

k = length coefficient which gives influence of boundary conditions. The following values are appropriate for the described end conditions:

= 1 (simple support both ends)

= 2 (cantilever beam)

= 0.5 (clamped at both ends)

r = radius of gyration of component

- d. Maximum allowable bending stress at the outermost fiber of a net section, due to flexure about one plane of symmetry is:

$$F_b = 0.60 S_y \quad (\text{equivalent to primary bending})$$

- e. Combined bending and compression on a net section satisfies:

$$\frac{f_a}{F_a} + \frac{C_{mx} f_{bx}}{D_x F_{bx}} + \frac{C_{my} f_{by}}{D_y F_{by}} < 1$$

where:

f_a = Direct compressive stress in the section

f_{bx} = Maximum bending stress along x-axis

f_{by} = Maximum bending stress along y-axis

C_{mx} = 0.85

C_{my} = 0.85

D_x = $1 - (f_a/F'_{ex})$

D_y = $1 - (f_a/F'_{ey})$

$F'_{ex,ey}$ = $(\pi^2 E)/(2.15 (kl/r)_{x,y}^2)$

E = Young's Modulus

and subscripts x,y reflect the particular bending plane.

- f. Combined flexure and compression (or tension) on a net section:

$$\frac{f_a}{0.6 S_y} + \frac{f_{bx}}{F_{bx}} + \frac{f_{by}}{F_{by}} < 1.0$$

The above requirements are to be met for both direct tension or compression.

- g. Welds

Allowable maximum shear stress on the net section of a weld is given by:

$$F_w = 0.3 S_u$$

where S_u is the weld material ultimate strength at temperature. For fillet weld legs in contact with base metal, the shear stress on the gross section is limited to $0.4S_y$, where S_y is the base material yield strength at temperature.

(ii) Level D Service Limits

Based on Section F-1334 (ASME Section III, Appendix F) [6.6.2], the limits for the Level D condition are the minimum of $1.2 (S_y/F_t)$ or $(0.7S_u/F_t)$ times the corresponding limits for the Level A condition. S_u is ultimate tensile stress at the specified rack design temperature. Examination of material properties for 304L stainless demonstrates that 1.2 times the yield strength is less than the 0.7 times the ultimate strength.

Exceptions to the above general multiplier are the following:

- a) Stresses in shear shall not exceed the lesser of $0.72S_y$ or $0.42S_u$. In the case of the material used here, $0.72S_y$ governs.
- b) Axial Compression Loads shall be limited to $2/3$ of the calculated buckling load.
- c) Combined Axial Compression and Bending - The equations for Level A conditions shall apply except that:

$F_a = 0.667 \times \text{Buckling Load} / \text{Gross Section Area}$,
and the terms F'_{ex} and F'_{ey} may be increased by the factor 1.65.

- d) For welds, the Level D allowable maximum weld stress is not specified in Appendix F of the ASME Code. An appropriate limit for weld throat stress is conservatively set here as:

$$F_w = (0.3 S_u) \times \text{factor}$$

where:

$$\begin{aligned} \text{factor} &= (\text{Level D shear stress limit}) / (\text{Level A shear stress limit}) \\ &= 0.72 \times S_y / 0.4 \times S_y = 1.8 \end{aligned}$$

6.6.3 Dimensionless Stress Factors

For convenience, the stress results are presented in dimensionless form. Dimensionless stress factors are defined as the ratio of the actual developed stress to the specified limiting value. The limiting value of each stress factor is 1.0.

Stress factors reported are:

R_1 = Ratio of direct tensile or compressive stress on a net section to its allowable value (note pedestals only resist compression)

R_2 = Ratio of gross shear on a net section in the x-direction to its allowable value

R_3 = Ratio of maximum x-axis bending stress to its allowable value for the section

R_4 = Ratio of maximum y-axis bending stress to its allowable value for the section

R_5 = Combined flexure and compressive factor (as defined in the foregoing)

R_6 = Combined flexure and tension (or compression) factor (as defined in the foregoing)

R_7 = Ratio of gross shear on a net section in the y-direction to its allowable value

6.6.4 Loads and Loading Combinations for Spent Fuel Racks

The applicable loads and their combinations which must be considered in the seismic analysis of rack modules is excerpted from Refs. [6.1.2] and [6.6.3]. The load combinations considered are identified below:

Loading Combination	Service Level
D + L D + L + T _o D + L + T _o + E	Level A
D + L + T _a + E D + L + T _o + P _f	Level B
D + L + T _a + E' D + L + T _o + F _d	Level D The functional capability of the fuel racks must be demonstrated.

Where:

- D = Dead weight-induced loads (including fuel assembly weight)
- L = Live Load (not applicable for the fuel rack, since there are no moving objects in the rack load path)
- P_f = Upward force on the racks caused by postulated stuck fuel assembly
- F_d = Impact force from accidental drop of the heaviest load from the maximum possible height.
- E = Operating Basis Earthquake (OBE)
- E' = Design Basis Earthquake (SSE)
- T_o = Differential temperature induced loads (normal operating or shutdown condition based on the most critical transient or steady state condition)
- T_a = Differential temperature induced loads (the highest temperature associated with the postulated abnormal design conditions)

T_a and T_o produce local thermal stresses. The worst thermal stress field in a fuel rack is obtained when an isolated storage location has a fuel assembly generating heat at maximum postulated rate and

surrounding storage locations contain no fuel. Heated water makes unobstructed contact with the inside of the storage walls, thereby producing maximum possible temperature difference between adjacent cells. Secondary stresses produced are limited to the body of the rack; that is, support pedestals do not experience secondary (thermal) stresses.

6.7 Parametric Simulations

The following table presents a complete listing of the simulations discussed herein. Consideration of the parameters described in Section 6.5 resulted in the following runs.

<u>Run</u>	<u>Unit</u>	<u>Rack Type</u>	<u>Rack Fuel Loading Pattern</u>	<u>COF</u>	<u>Event</u>
1	1	Region 1	fully loaded	0.8	SSE
2	1	Region 1	fully loaded	0.2	SSE
3	1	Region 1	fully loaded	Random	SSE
4	1	Region 1	fully loaded	0.8	OBE
5	1	Region 1	fully loaded	0.2	OBE
6	1	Region 1	fully loaded	Random	OBE
7	1	Region 1	nearly empty rack	0.8	SSE
8	1	Region 1	half loaded (diagonally)	0.8	SSE
9	1	Region 1	Half loaded (on east side)	0.8	SSE
10	1	Region 1	half loaded (on north side)	0.8	SSE
11 *	1	Region 1	fully loaded with equipment tray	0.8	SSE
12	2	Region 2	fully loaded	0.8	SSE
13	2	Region 2	fully loaded	0.2	SSE
14	2	Region 2	fully loaded	Random	SSE
15	2	Region 2	fully loaded	0.8	OBE
16	2	Region 2	fully loaded	0.2	OBE
17	2	Region 2	fully loaded	Random	OBE
18	2	Region 2	nearly empty rack	0.8	SSE
19	2	Region 2	half loaded (diagonally)	0.8	SSE
20	2	Region 2	half loaded (one side)	0.8	SSE
21 *	2	Region 2	fully loaded with equipment tray	0.8	SSE

* See explanatory note about runs 11 and 21 below.

where:

Random = Gaussian distribution with a mean of 0.5 Coefficient of friction (upper and lower limits of 0.8 and 0.2).

Runs 7 through 10 and 18 through 20 are performed to evaluate the rack stability against overturning. Runs were not necessary for the OBE condition, since the SSE condition will produce worse displacements and the acceptance criteria for the OBE case (margin of at least 1.5 against tipover) is applied for these simulations. The runs include various fuel loading patterns selected to place the total fuel mass centroid as far from the rack centroid as possible. These fictitious conditions were modeled to maximize horizontal displacements and the possibility of overturning. Therefore, these simulations are not concerned with rack stresses, pedestal loads, etc. and the following sections will only report the displacements for these runs.

Additionally, a review of the results for these simulations indicates that these runs do not control for rack stresses or pedestal loadings, as expected, due to the lower fuel mass considered in the simulations.

The Cask Pit Area of each Unit has historically been used for underwater storage of miscellaneous equipment. Placement of storage racks in these pits requires removal of any components in these areas and a reduction of storage space. Runs 11 and 21 are performed to consider a fictitious equipment tray (platform) weighing 2000 pounds (including all stored equipment) located 24" above the top of the storage rack and supported by the rack. These runs are prepared to address possible installation of a future miscellaneous equipment platform being placed above the storage rack. Performing these simulations for the 0.8 coefficient of friction conditions was chosen, since these conditions produced worst-case displacements and/or stress factors for fully loaded simulations performed without the fictitious storage platforms.

6.8 Time History Simulation Results

The results from the DYNARACK runs can be obtained from the raw data output files. However, due to the huge quantity of output data, a post-processor is used to scan for worst case conditions and develop the stress factors discussed in subsection 6.6.3. Further reduction in this bulk of information is provided

in this section by extracting the worst case values from the parameters of interest; namely displacements, support pedestal forces, impact loads, and stress factors. This section also summarizes supplemental analyses performed to develop and evaluate structural member stresses, which are not determined by the post processor.

6.8.1 Rack Displacements

The maximum rack displacements are obtained from the time histories of the motion of the upper and lower four corners of each rack in each of the simulations. The maximum absolute value of displacement in the two horizontal directions, relative to the pool slab, is computed for each rack, at the top and bottom corners. The maximum displacement for all simulations is 0.396" in the North-South (x) direction, which occurs in simulation 13. However, other simulations have comparable displacements in both x and y directions.

Under all of the simulations, the rack does not impact the adjacent walls at any time (i.e., the rack-to-wall gaps at every time instant during the simulation are always greater than 0.0 inches). It is noted that the minimum nominal gap between the rack and wall (3-15/16") occurs on the Unit 1 configuration.

By comparison with half the distance between the pedestals for the rack with the worst-case displacement, tipover is not a concern and the safety factor is approximately 180. The maximum displacement (0.385") for the Unit 1, region 1 rack simulations is similar, with a safety factor against tipover of 172.

6.8.2 Pedestal Vertical Forces

The maximum vertical pedestal force for the Unit 2 rack is 216,800 lbs, which occurs in simulation 21. The maximum vertical pedestal force for the Unit 1 rack is 136,900 lbs, which occurs in simulation 11. The Unit 2 rack pedestal loads are greater primarily due to the larger number of assemblies stored within the Region 2 style rack.

6.8.3 Pedestal Friction Forces

The maximum (x or y direction) shear loads are 73,400 lbs for Unit 2 (simulation 21) and 49,400 lbs for Unit 1 (simulation 3).

6.8.4 Rack Impact Loads

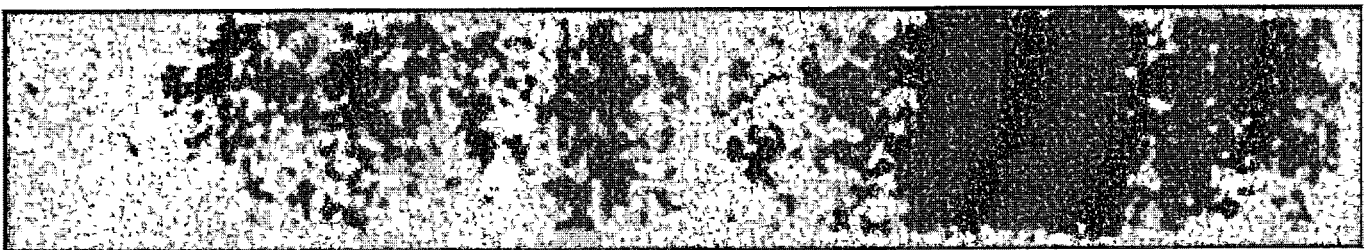
A freestanding rack, by definition, is a structure subject to potential impacts during a seismic event. Impacts arise from rattling of the fuel assemblies in the storage rack locations and, in some instances, from localized impacts between the racks and the pool wall. The following sections discuss the bounding values of these impact loads.

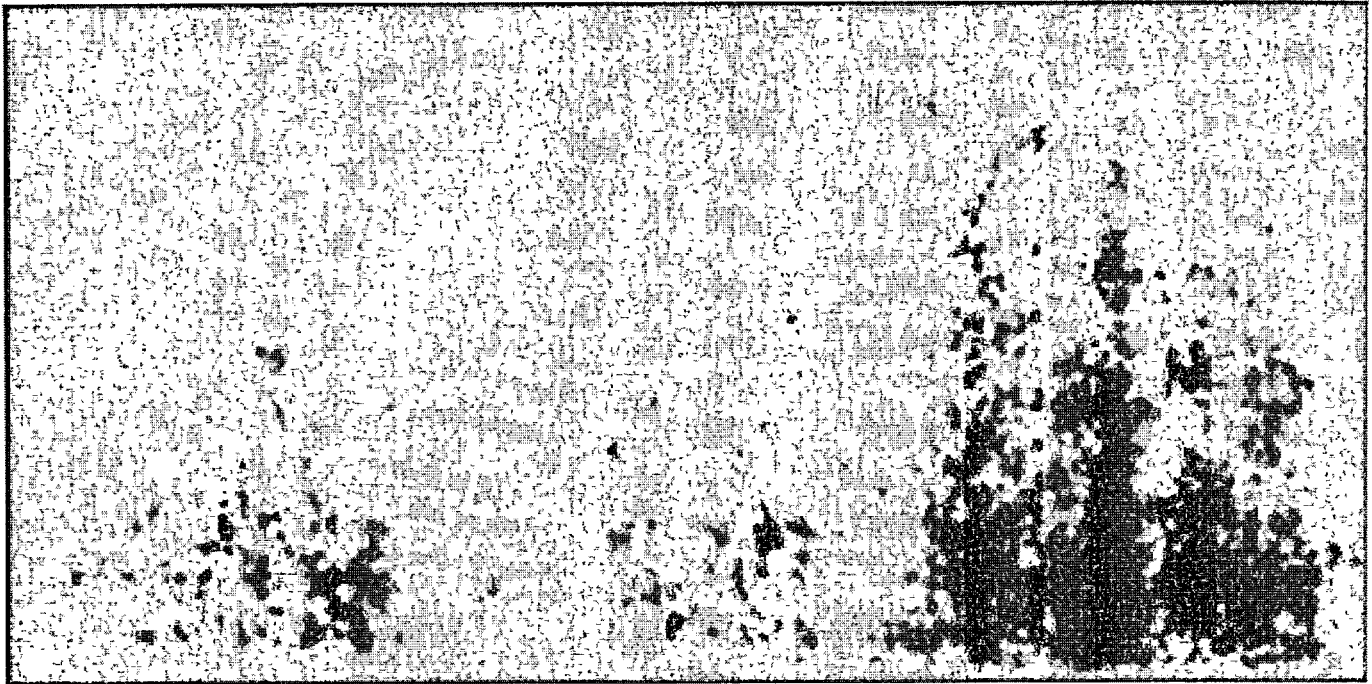
6.8.4.1 Rack to Wall Impacts

The storage racks do not impact the Cask Pit walls under any simulation. The gap between the top-of-rack and wall is several times greater than the maximum horizontal displacement.

6.8.4.2 Fuel to Cell Wall Impact Loads

A review of all simulations performed allows determination of the maximum instantaneous impact load between fuel assembly and fuel cell wall at any modeled impact site. The maximum fuel/cell wall impact load value is 461 lbs, which occurs during simulation 21.





Therefore, a maximum fuel assembly-to-cell wall impact load of less than 500 lbs is provided with a safety factor of about 44.

6.9 Rack Structural Evaluation

6.9.1 Rack Stress Factors

The time history results from the DYNARACK solver provide the pedestal normal and lateral interface forces, which may be converted to the limiting bending moment and shear force at the bottom baseplate-pedestal interface. In particular, maximum values for the previously defined stress factors are determined for every pedestal. With this information available, the structural integrity of the pedestal can be assessed and reported. The net section maximum (in time) bending moments and shear forces can also be determined at the bottom baseplate-rack cellular structure interface for each spent fuel rack in the pool. Using these forces and moments, the maximum stress in the limiting rack cell (box) can be evaluated.

The stress factor results for male and female pedestals, and for the entire spent fuel rack cellular cross-section just above the bottom casting have been determined. These factors are reported for every pedestal and the rack cell wall cross-section in each simulation. These locations are the most heavily loaded net sections in the structure so that satisfaction of the stress factor criteria at these locations ensures that the overall structural criteria set forth in Section 6.6 are met.

The maximum SSE condition pedestal stress factor is 0.189, which occurs under simulation 12. The maximum, OBE condition pedestal stress factor is 0.197, which occurs under simulation 16. The maximum SSE condition cell wall stress factor is 0.170, which occurs under simulation 12. The maximum, OBE condition cell wall stress factor is 0.205, which occurs under simulation 16. An evaluation of the stress factors for all of the simulations performed, leads to the conclusion that all stress factors, as defined in Section 3, are less than the mandated limit of 1.0. Therefore, the requirements of Section 3 are indeed satisfied for the load levels considered for every limiting location in the rack.

6.9.2 Pedestal Thread Shear Stress

The maximum average shear stress in the engagement region under SSE conditions is 7,446 psi. This computed stress is applicable to both the male and female pedestal threads. The ultimate strength of the female part of the pedestal is 66,200 psi. The yield stress for this material is 21,300 psi.

The allowable shear stress in the female pedestal for Level B conditions is 0.4 times the yield stress, which gives 8,520 psi. The allowable shear stress for Level D conditions is the lesser of: $0.72 S_y = 15,336$ psi or $0.42 S_u = 27,804$ psi. Therefore, the former criteria controls. However, for conservatism the actual stress for the SSE condition may be compared against the allowable for the OBE condition. Since 7,446 psi is less than the OBE allowable of 8,520 psi, the female pedestal threads are shown to be acceptable. The allowable stress for the male pedestal threads is much larger due to the higher material strength.

6.9.3 Local Stresses Due to Impacts

Impact loads at the pedestal base (discussed in subsection 6.8.2) produce stresses in the pedestal for which explicit stress limits are prescribed in the Code. However, the impact loads on the cellular region of the racks, discussed in subsection 6.8.4, produce stresses, which attenuate rapidly away from the loaded region. This behavior is characteristic of secondary stresses.

Even though limits on secondary stresses are not prescribed in the Code for class 3 NF structures, evaluations must be made to ensure that the localized impacts do not lead to plastic deformations in the storage cells which affect the subcriticality of the stored fuel array.

Local cell wall integrity is conservatively estimated from peak impact loads. Plastic analysis is used to obtain the limiting impact load which would lead to gross permanent deformation. As shown in Tables 6.9.1 and 6.9.2, the limiting impact load (of 3,423 lbf, including a safety factor of 2.0) is much greater than the highest calculated impact load value (of less than 500 lbf, see subsection 6.8.4.2) obtained from any of the rack analyses. Therefore, fuel impacts do not represent a significant concern with respect to fuel rack cell deformation.

6.9.4 Assessment of Rack Fatigue Margin

Deeply submerged high density spent fuel storage racks arrayed in close proximity to each other in a free-standing configuration behave primarily as a nonlinear cantilevered structure when subjected to 3-D seismic excitations. In addition to the pulsations in the vertical load at each pedestal, lateral friction forces at the pedestal/ rack platform interface, which help prevent or mitigate lateral sliding of the rack, also exert a time-varying moment in the baseplate region of the rack. The friction-induced lateral forces act simultaneously in x and y directions with the requirement that their vectorial sum does not exceed μV , where μ is the limiting interface coefficient of friction and V is the concomitant vertical thrust on the rack platform (at the given time instant). As the vertical thrust at a pedestal location changes, so does

the maximum friction force, F , that the interface can exert. In other words, the lateral force at the pedestal/ rack platform interface, F , is given by

$$F \leq \mu N(\tau)$$

where N (vertical thrust) is the time-varying function of τ . F does not always equal μN ; rather, μN is the maximum value it can attain at any time; the actual value, of course, is determined by the dynamic equilibrium of the rack structure.

In summary, the horizontal friction force at the pedestal/ rack platform interface is a function of time; its magnitude and direction of action varies during the earthquake event.

The time-varying lateral (horizontal) and vertical forces on the extremities of the support pedestals produce stresses at the root of the pedestals in the manner of an end-loaded cantilever. The stress field in the cellular region of the rack is quite complex, with its maximum values located in the region closest to the pedestal. The maximum magnitude of the stresses depends on the severity of the pedestal end loads and on the geometry of the pedestal/rack baseplate region.

Alternating stresses in metals produce metal fatigue if the amplitude of the stress cycles is sufficiently large. In high density racks designed for sites with moderate to high postulated seismic action, the stress intensity amplitudes frequently reach values above the material endurance limit, leading to expenditure of the fatigue "usage" reserve in the material.

Because the locations of maximum stress (viz., the pedestal/rack baseplate junction) and the close placement of racks, a post-earthquake inspection of the high stressed regions in the racks is not feasible. Therefore, the racks must be engineered to withstand multiple earthquakes without reliance of nondestructive inspections for post-earthquake integrity assessment. The fatigue life evaluation of racks is an integral aspect of a sound design.

The time-history method of analysis, deployed in this report, provides the means to obtain a complete cycle history of the stress intensities in the highly stressed regions of the rack. Having determined the amplitude of the stress intensity cycles and their number, the cumulative damage factor, U, can be determined using the classical Miner's rule:

$$U = \sum \frac{n_i}{N_i}$$

where n_i is the number of stress intensity cycles of amplitude σ_i , and N_i is the permissible number of cycles corresponding to σ_i from the ASME fatigue curve for the material of construction. U must be less than or equal to 1.0.

To evaluate the cumulative damage factor, a finite element model of a portion of the spent fuel rack in the vicinity of a support pedestal is constructed in sufficient detail to provide an accurate assessment of stress intensities. The finite element solutions for unit pedestal loads in three orthogonal directions are combined to establish the maximum value of stress intensity as a function of the three unit pedestal loads. Using the archived results of the spent fuel rack dynamic analyses (pedestal load histories versus time) enables a time-history of stress intensity to be established at the most limiting location. This permits establishing a set of alternating stress intensity ranges versus cycles for an SSE and an OBE event. Following ASME Code guidelines for computing U for the Unit 2 rack, it is found that $U = 0.196$ due to the combined effect of one SSE and twenty OBE events. This is well below the ASME Code limit of 1.0. The U value for the Unit 1 rack is much lower (less than 0.1)

6.9.5 Weld Stresses

Weld locations subjected to significant seismic loading are at the bottom of the rack at the baseplate-to-cell connection, at the top of the pedestal support at the baseplate connection, and at cell-to-cell connections. Bounding values of resultant loads are used to qualify the connections.

a. Baseplate-to-Rack Cell Welds

For Level A or B conditions, Ref. [6.6.1] permits an allowable weld stress of $\tau = .3 S_u = 19,860$ psi. As stated in subsection 6.6.2 the allowable may be increased for Level D by some amplification factor.

Weld stresses are produced through the use of a simple conversion (ratio) factor applied to the corresponding stress factor in the adjacent rack material. The ratio is developed from the differences in material thickness and length versus weld throat dimension and length:

$$\text{RATIO} = \frac{t_{\text{cell}} \cdot L_{\text{cell}}}{t_{\text{rack}} \cdot L_{\text{rack}}}$$

The highest predicted cell to baseplate weld stress under the Unit 2 OBE simulations is conservatively calculated to be 6,436 psi. This value is less than the OBE allowable weld stress value, which is 19,860. The highest predicted cell to baseplate weld stress for the Unit 2 SSE simulation is 11,048 psi. The calculated stress value is less than the allowable weld stress value 35,748 psi. The Unit 2 rack cell-to-pedestal weld stresses control over the Unit 1 stresses. As shown in Tables 6.9.1 and 6.9.2, all weld stresses between the baseplate and cell wall base are acceptable.

b. Baseplate-to-Pedestal Welds

The weld between baseplate and support pedestal is checked using finite element analysis to determine that the maximum stress for Unit 2 is 13,780 psi under a Level D event. This calculated stress value is well below the allowable of 35,748 psi. The maximum Unit 2 weld stress under OBE conditions is 3,397 psi, which is less than the OBE allowable of 19,860 psi. The Unit 1 weld stresses are lower as shown in Table 6.9.1. Therefore, the welds are acceptable.

c. Cell-to-Cell Welds

Cell-to-cell connections are by a series of connecting welds along the cell height. Stresses in storage cell to cell welds develop due to fuel assembly impacts with the cell wall. These weld stresses are conservatively considered by assuming that fuel assemblies in adjacent cells are moving out of phase with one another so that impact loads in two adjacent cells are in opposite directions and are applied simultaneously. This load application tends to separate the two cells from each other at the weld.

Tables 6.9.1 and 6.9.2 give results for the maximum allowable load that can be transferred by these welds based on the available weld area. An upper bound on the load required to be transferred is also given in the tables and is much lower than the allowable load. This upper bound value is very conservatively obtained by applying the bounding rack-to-fuel impact load from any simulation in two orthogonal directions simultaneously, and multiplying the result by 2 to account for the simultaneous impact of two assemblies. An equilibrium analysis at the connection then yields the upper bound load to be transferred. It is seen from the results in Tables 6.9.1 and 6.9.2 that the calculated load is well below the allowable.

6.10 Level A Evaluation

The Level A condition is not a governing condition for spent fuel racks, since the general level of loading is far less than Level B loading and the stress allowables are the same for the two conditions. To illustrate this, the racks for each Unit are considered under the dead weight load. It is shown below that the maximum pedestal load under the deadweight condition is low and that further stress evaluations are unnecessary.

6.10.1 Unit 1 Cask Pit Rack

Dry Weight of Largest Holtec Rack	=	34200 lbf
Dry Weight of 143 Fuel Assemblies	=	203489 lbf
Total Dry Weight	=	237689 lbf
Total Buoyant Weight ($0.87 \times$ Total Dry Weight)	=	206789 lbf
Load per Pedestal	=	51697 lbf

The stress allowables for the normal condition is the same as for the Upset (OBE) condition, which resulted in a maximum pedestal load of 99,100 lbs. Since this load (and the corresponding stress throughout the rack members) is much greater than the 51,697 lb load calculated above, the Upset condition controls over normal (Gravity) condition. Therefore, no Level A evaluation is required to be performed.

6.10.2 Unit 2 Cask Pit Rack

Dry Weight of Largest Holtec Rack	=	29054 lbf
Dry Weight of 225 Fuel Assemblies	=	311400 lbf
Total Dry Weight	=	340454 lbf
Total Buoyant Weight ($0.87 \times$ Total Dry Weight)	=	296195 lbf
Load per Pedestal	=	74049 lbf

The stress allowables for the normal condition is the same as for the upset condition, which resulted in a maximum pedestal load of 130,000 lbs. Since this load (and the corresponding stress throughout the

rack members) is much greater than the 74,049 lb load calculated above, the Upset (OBE) condition controls over normal (Gravity) condition. Therefore, no Level A evaluation is required to be performed.

6.11 Hydrodynamic Loads on Pool Walls

The maximum hydrodynamic pressure that is developed, at any point between the fuel racks and the walls, due to fluid coupling on the Unit 1 rack is 1.05 psi. The maximum hydrodynamic pressure that is developed, at any point between the fuel racks and the walls, due to fluid coupling on the Unit 2 rack is 1.8 psi. The hydrodynamic pressure values are unsigned and, therefore, are added to or subtracted from the pool hydrostatic pressure at the depth of the tops of the racks during evaluation of the Cask Pit structure, as discussed in Section 8.0.

6.12 Temperature Gradient Across Rack Cell Wall

6.12.1 Cell Wall Buckling

The possibility of cell wall buckling and evaluation of the cell-to-cell welded joints are examined under the loading conditions arising from thermal effects due to an isolated hot cell, in this sub-section.

The allowable local buckling stresses in the fuel cell walls are obtained by using classical plate buckling analysis. The following formula for the critical stress has been used.

$$\sigma_{cr} = \frac{\beta \pi^2 E t^2}{12 b^2 (1 - \mu^2)}$$

where $E = 27 \times 10^6$ psi, μ is Poison's ratio, $t = .075$ ", $b = 8.58$ ". The factor β is suggested to be 4.0 in [6.12.1] for a long panel loaded as shown in Figure 6.12.1.

For the given data $\sigma_{cr} = 7,458$ psi

It should be noted that this calculation is based on the applied stress being uniform along the entire length of the cell wall. In the actual fuel rack, the compressive stress comes from consideration of overall bending of the rack structures during a seismic event and as such is negligible at the rack top and maximum at the rack bottom. It is conservative to apply the above equation to the rack cell wall if we compare σ_{cr} with the maximum compressive stress anywhere in the cell wall.

As shown in Section 6, this local buckling stress limit is not violated anywhere in the body of the rack modules, since the maximum compressive stress in the outermost cell is $= 2 \cdot (0.6)(21,300) \cdot R6$ (from Section 6.9.1 with $R6 = .170$) $= 4,350 \text{ psi} < 7,458 \text{ psi}$. Therefore, cell wall buckling is not a concern.

6.12.2 Cell-to-Cell Weld Stress Due to Hot Cell Thermal Expansion

Cell-to cell welded joints are examined under the loading conditions arising from thermal effects due to an isolated hot cell, in this sub-section. This secondary stress condition is evaluated alone and not combined with primary stresses from other load conditions.

A thermal gradient between cells will develop when an isolated storage location contains a fuel assembly emitting maximum postulated heat, while the surrounding locations are empty. We can obtain a conservative estimate of weld stresses along the length of an isolated hot cell by considering a beam strip uniformly heated by 90°F , and restrained from growth along one long edge. This thermal gradient is based on the results of the thermal-hydraulic evaluations discussed in Section 5.0, which shows that the maximum difference between the local cell maximum temperature (196°F) and the bulk pool temperature (161°F) is approximately 35°F . The configuration is shown in Figure 6.12.2.

Using shear beam theory and subjecting the strip to a uniform temperature rise $\Delta T = 90^\circ\text{F}$, we can calculate an estimate of the maximum value of the average shear stress in the strip. The strip is subjected to the following boundary conditions.

- a. Displacement $U_x(x,y) = 0$ at $x = 0$, at $y = H$, all x .

- b. Average force M_x , acting on the cross section $Ht = 0$ at $x = 1$, all y .

The final result for wall shear stress, maximum at $x = 1$, is found to be given as

$$\tau_{\max} = \frac{E \alpha \Delta T}{0.931}$$

where $E = 27 \times 10^6$ psi, $\alpha = 9.5 \times 10^{-6}$ in/in $^{\circ}\text{F}$ and $\Delta T = 90^{\circ}\text{F}$. Therefore, we obtain an estimate of maximum weld shear stress in an isolated hot cell, due to thermal gradient, as

$$\tau_{\max} = 24,796 \text{ psi}$$

Since this is a secondary thermal stress, we use the allowable shear stress criteria for faulted conditions ($0.42 \cdot S_u = 27,804$ psi) as a guide to indicate that the maximum shear is acceptable.

6.13 Rack Support Platform

The floor of the Cask Pit of each Unit is at a lower elevation than the floor of the spent fuel pool. In order to ensure that the top of any spent fuel rack placed in the cask pit is at the same elevation as racks in the pool, a cask pit rack platform will be installed in each Cask Pit to raise the top of the rack to the appropriate elevation.

Figure 2.1.3 provides a schematic representation of the rack support platforms. The cask pit rack platforms consist of a frame approximately 3.5 feet tall constructed of box beam sections comprised of 1" plates with 8" diameter pipes located directly beneath each rack pedestal. The top of the platform corners are equipped with positioning rings, such that the 5" OD rack pedestals can be accurately positioned on the platform.

The evaluations for the platforms are performed using classical strength of materials formulations. Worst-case loads from the rack seismic/structural evaluation were used as the design inputs to design the platform. The platforms are designed with the same Code requirements as the supported racks. As such,

the platforms are designed as Class 3 Linear-Type component supports and must meet applicable stress levels of ASME Section III, NF-3553 [1]. The evaluations show that all required geometry checks and stress checks are satisfied for both Level A and Level D conditions and for the lifting condition. Safety factors for bearing, tearout and gross force and moment are greater than 1.0.

6.14 References

- [6.1.1] USNRC NUREG-0800, Standard Review Plan, June 1987.
- [6.1.2] (USNRC Office of Technology) "OT Position for Review and Acceptance of Spent Fuel Storage and Handling Applications", dated April 14, 1978, and January 18, 1979 amendment thereto.
- [6.2.1] Soler, A.I. and Singh, K.P., "Seismic Responses of Free Standing Fuel Rack Constructions to 3-D Motions", Nuclear Engineering and Design, Vol. 80, pp. 315-329 (1984).
- [6.2.2] Soler, A.I. and Singh, K.P., "Some Results from Simultaneous Seismic Simulations of All Racks in a Fuel Pool", INNEM Spent Fuel Management Seminar X, January, 1993.
- [6.2.3] Singh, K.P. and Soler, A.I., "Seismic Qualification of Free Standing Nuclear Fuel Storage Racks - the Chin Shan Experience, Nuclear Engineering International, UK (March 1991).
- [6.2.4] Holtec Proprietary Report HI-961465 - WPMR Analysis User's Manual, May, 1998.
- [6.4.1] NUREG 0800, Standard Review Plan, SRP 3.7.1, Seismic Design Parameters.
- [6.4.2] Holtec Proprietary Report HI-89364 - Verification and User's Manual for Computer Code GENEQ, January, 1990.
- [6.5.1] Rabinowicz, E., "Friction Coefficients of Water Lubricated Stainless Steels for a Spent Fuel Rack Facility," MIT, a report for Boston Edison Company, 1976.
- [6.5.2] Singh, K.P. and Soler, A.I., "Dynamic Coupling in a Closely Spaced Two-Body System Vibrating in Liquid Medium: The Case of Fuel Racks," 3rd International Conference on Nuclear Power Safety, Keswick, England, May 1982.
- [6.5.3] Fritz, R.J., "The Effects of Liquids on the Dynamic Motions of Immersed Solids," Journal of Engineering for Industry, Trans. of the ASME, February 1972, pp 167-172.
- [6.5.4] Levy, S. and Wilkinson, J.P.D., "The Component Element Method in Dynamics with Application to Earthquake and Vehicle Engineering," McGraw Hill, 1976.

- [6.5.5] Paul, B., "Fluid Coupling in Fuel Racks: Correlation of Theory and Experiment", (Proprietary), NUSCO/Holtec Report HI-88243.
- [6.6.1] ASME Boiler & Pressure Vessel Code, Section III, Subsection NF, 1989 Edition.
- [6.6.2] ASME Boiler & Pressure Vessel Code, Section III, Appendices, 1989 Edition.
- [6.6.3] USNRC Standard Review Plan, NUREG-0800 (Section 3.8.4, Rev. 2, 1989).
- [6.8.1] UCID-21246, "Dynamic Impact Effects on Spent Fuel Assemblies," Lawrence Livermore National Laboratory, dated October 20, 1987.
- [6.9.1] ACI 349-85, Code Requirements for Nuclear Safety Related Concrete Structures, American Concrete Institute, Detroit, Michigan, 1985.
- [6.9.2] ACI 318-95, Building Code Requirements for Structural Concrete, American Concrete Institute, Detroit, Michigan, 1995.
- [6.12.1] "Strength of Materials", S. P. Timoshenko, 3rd Edition, Part II, pp 194-197 (1956).

Table 6.2.1		
PARTIAL LISTING OF FUEL RACK APPLICATIONS USING DYNARACK		
PLANT	DOCKET NUMBER(s)	YEAR
Enrico Fermi Unit 2	USNRC 50-341	1980
Quad Cities 1 & 2	USNRC 50-254, 50-265	1981
Rancho Seco	USNRC 50-312	1982
Grand Gulf Unit 1	USNRC 50-416	1984
Oyster Creek	USNRC 50-219	1984
Pilgrim	USNRC 50-293	1985
V.C. Summer	USNRC 50-395	1984
Diablo Canyon Units 1 & 2	USNRC 50-275, 50-323	1986
Byron Units 1 & 2	USNRC 50-454, 50-455	1987
Braidwood Units 1 & 2	USNRC 50-456, 50-457	1987
Vogtle Unit 2	USNRC 50-425	1988
St. Lucie Unit 1	USNRC 50-335	1987
Millstone Point Unit 1	USNRC 50-245	1989
Chinshan	Taiwan Power	1988
D.C. Cook Units 1 & 2	USNRC 50-315, 50-316	1992
Indian Point Unit 2	USNRC 50-247	1990
Three Mile Island Unit 1	USNRC 50-289	1991
James A. FitzPatrick	USNRC 50-333	1990
Shearon Harris Unit 2	USNRC 50-401	1991
Hope Creek	USNRC 50-354	1990
Kuosheng Units 1 & 2	Taiwan Power Company	1990
Ulchin Unit 2	Korea Electric Power Co.	1990

Table 6.2.1		
PARTIAL LISTING OF FUEL RACK APPLICATIONS USING DYNARACK		
PLANT	DOCKET NUMBER(s)	YEAR
Laguna Verde Units 1 & 2	Comision Federal de Electricidad	1991
Zion Station Units 1 & 2	USNRC 50-295, 50-304	1992
Sequoyah	USNRC 50-327, 50-328	1992
LaSalle Unit 1	USNRC 50-373	1992
Duane Arnold Energy Center	USNRC 50-331	1992
Fort Calhoun	USNRC 50-285	1992
Nine Mile Point Unit 1	USNRC 50-220	1993
Beaver Valley Unit 1	USNRC 50-334	1992
Salem Units 1 & 2	USNRC 50-272, 50-311	1993
Limerick	USNRC 50-352, 50-353	1994
Ulchin Unit 1	KINS	1995
Yonggwang Units 1 & 2	KINS	1996
Kori-4	KINS	1996
Connecticut Yankee	USNRC 50-213	1996
Angra Unit 1	Brazil	1996
Sizewell B	United Kingdom	1996
Waterford 3	USNRC 50-382	1996
Vogtle	USNRC 50-424	1997
J. A. Fitzpatrick	USNRC 50-333	1997
Vermont Yankee	USNRC 50-271	1998
Callaway	USNRC 50-483	1998

Table 6.2.1		
PARTIAL LISTING OF FUEL RACK APPLICATIONS USING DYNARACK		
PLANT	DOCKET NUMBER(s)	YEAR
Nine Mile	USNRC 50-220	1998
Chin Shan	Taiwan Power Company	1998
Millstone 3	USNRC 50-423	1998
Byron/Braidwood	USNRC 50-454, 50-455, 50-567, 50-457	1999
Wolf Creek	USNRC 50-482	1999
Plant Hatch Units 1 & 2	USNRC 50-321, 50-366	1999
Harris Pools C and D	USNRC 50-401	1999
Davis-Besse	USNRC 50-346	1999
Enrico Fermi Unit 2	USNRC 50-341	2000
Kewaunee	USNRC 50-305	2001

Table 6.3.1 RACK MATERIAL DATA (200°F) (ASME - Section II, Part D)			
Material	Young's Modulus E (psi)	Yield Strength S_y (psi)	Ultimate Strength S_u (psi)
SA240; 304L S.S.	27.6 x 10 ⁶	21,300	66,200
SUPPORT MATERIAL DATA (200°F)			
SA240, Type 304L (upper part of support feet)	27.6 x 10 ⁶	21,300	66,200
SA-564-630 (lower part of support feet; age hardened at 1100°F)	28.5 x 10 ⁶	106,300	140,000

Table 6.4.1	
UNIT 1	
TIME-HISTORY STATISTICAL CORRELATION RESULTS	
OBE	
Data1 to Data2	-0.041
Data1 to Data3	0.032
Data2 to Data3	0.081
SSE	
Data1 to Data2	0.052
Data1 to Data3	-0.011
Data2 to Data3	-0.021

Data1 corresponds to the time-history acceleration values along the **X axis (East)**

Data2 corresponds to the time-history acceleration values along the **Y axis (North)**

Data3 corresponds to the time-history acceleration values along the **Z axis (Vertical)**

Table 6.4.2	
UNIT 2	
TIME-HISTORY STATISTICAL CORRELATION RESULTS	
OBE	
Data1 to Data2	0.042
Data1 to Data3	0.088
Data2 to Data3	-0.025
SSE	
Data1 to Data2	0.006
Data1 to Data3	0.137
Data2 to Data3	-0.051

Data1 corresponds to the time-history acceleration values along the **X axis (North)**

Data2 corresponds to the time-history acceleration values along the **Y axis (West)**

Data3 corresponds to the time-history acceleration values along the **Z axis (Vertical)**

Table 6.5.1						
Degrees-of-freedom						
LOCATION (Node)	DISPLACEMENT			ROTATION		
	U _x	U _y	U _z	θ _x	θ _y	θ _z
1	p ₁	p ₂	p ₃	q ₄	q ₅	q ₆
2	p ₇	p ₈	p ₉	q ₁₀	q ₁₁	q ₁₂
Node 1 is assumed to be attached to the rack at the bottom most point. Node 2 is assumed to be attached to the rack at the top most point. Refer to Figure 6.5.1 for node identification.						
2*	p ₁₃	p ₁₄				
3*	p ₁₅	p ₁₆				
4*	p ₁₇	p ₁₈				
5*	p ₁₉	p ₂₀				
1*	p ₂₁	p ₂₂				

where the relative displacement variables q_i are defined as:

p_i = q_i(t) + U_x(t) i = 1,7,13,15,17,19,21
= q_i(t) + U_y(t) i = 2,8,14,16,18,20,22
= q_i(t) + U_z(t) i = 3,9
= q_i(t) i = 4,5,6,10,11,12

p_i denotes absolute displacement (or rotation) with respect to inertial space
q_i denotes relative displacement (or rotation) with respect to the floor slab

* denotes fuel mass nodes

U(t) are the three known earthquake displacements

<p>Table 6.9.1</p> <p>UNIT 1</p> <p>COMPARISON OF BOUNDING CALCULATED LOADS/STRESSES VS. CODE ALLOWABLES</p> <p>AT IMPACT LOCATIONS AND AT WELDS</p>				
	OBE		SSE	
Item/Location	Calculated	Allowable	Calculated	Allowable
Fuel assembly/cell wall impact, lbf.	248	3,423 [†]	419	3,423 [†]
Rack/baseplate weld, psi	4,451	19,860	8,903	35,748
Baseplate/Pedestal weld, psi	2,151	19,860	6,167	35,748
Cell/cell welds, psi			1,946 ^{††}	8,520 ^{†††}

[†] Based on the limit load for a cell wall.

^{††} Cell-to-cell weld stresses, including consideration of shear.

^{†††} Conservatively based on OBE allowable stresses.

Table 6.9.2**UNIT 2****COMPARISON OF BOUNDING CALCULATED LOADS/STRESSES VS. CODE ALLOWABLES
AT IMPACT LOCATIONS AND AT WELDS**

	OBE		SSE	
Item/Location	Calculated	Allowable	Calculated	Allowable
Fuel assembly/cell wall impact, lbf.	159	3,423 [†]	449	3,423 [†]
Rack/baseplate weld, psi	6,436	19,860	11,048	35,748
Baseplate/Pedestal weld, psi	3,397	19,860	13,780	35,748
Cell/cell welds, psi			2,515 ^{††}	8,520 ^{†††}

[†] Based on the limit load for a cell wall.

^{††} Cell-to-cell weld stresses, including consideration of shear.

^{†††} Conservatively based on OBE allowable stresses.

Figure 6.4.1
Holtec Report
HI-2022882

St. Lucie Unit 1 Elevation 21.50'
Time History Accelerogram
E/W Direction SSE (2% Damping)

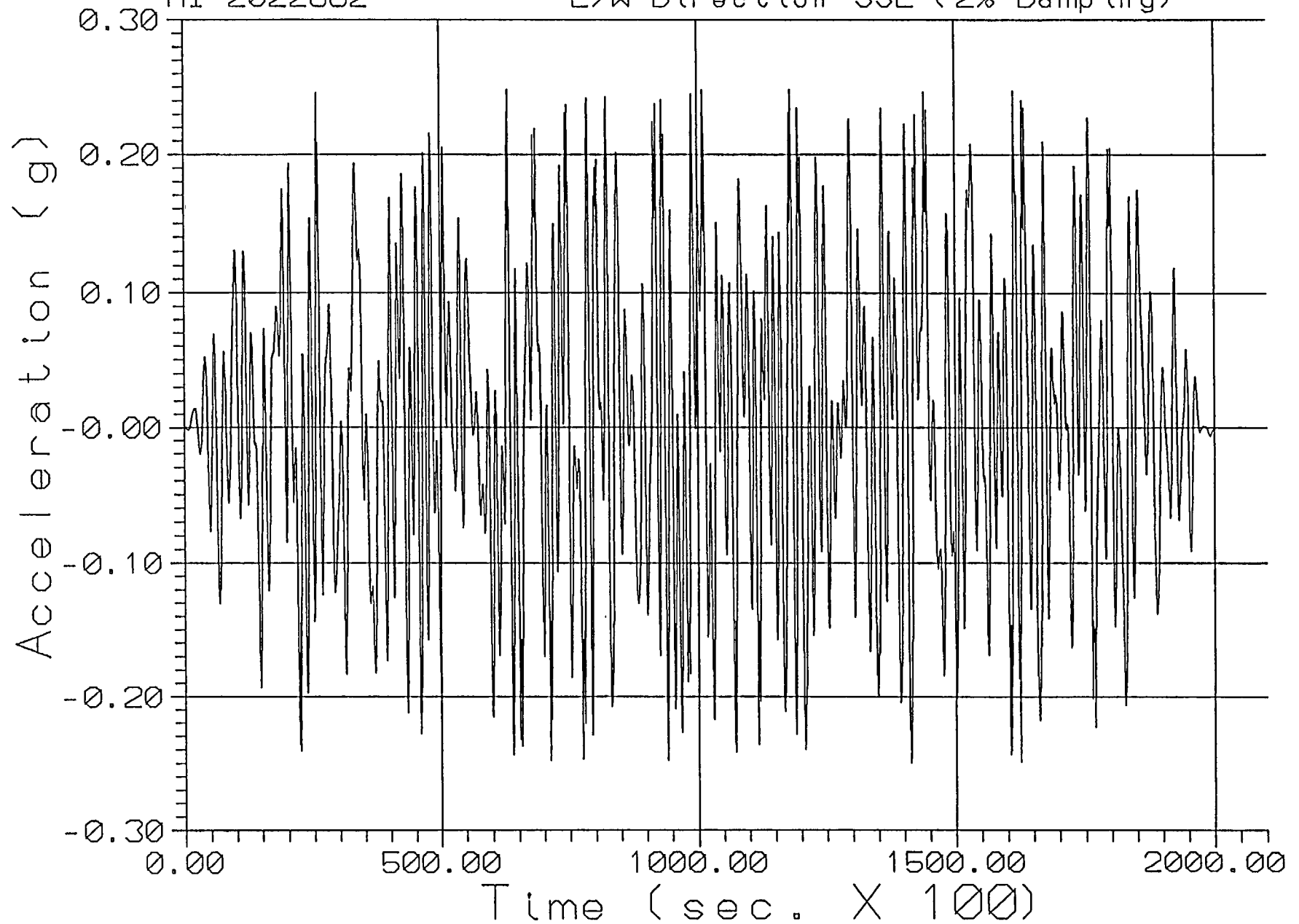


Figure 6.4.2
Holtec Report
HI-2022882

St. Lucie Unit 1 Elevation 21.50'
Time History Accelerogram
N/S Direction SSE (2% Damping)

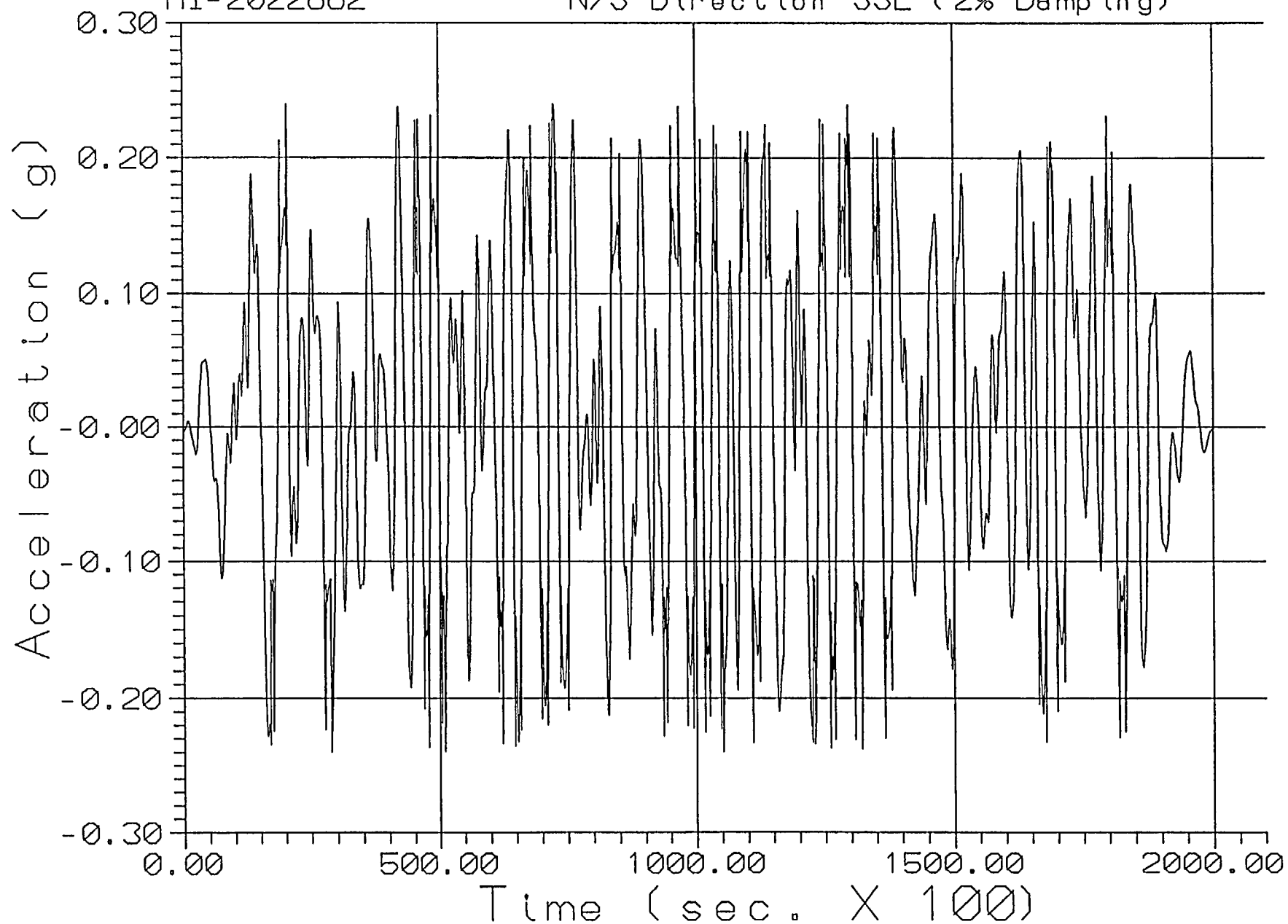


Figure 6.4.3
Holtec Report
HI-2022882

St. Lucie Unit 1 Elevation 21.50'
Time History Accelerogram
Vert SSE (2% Damping)

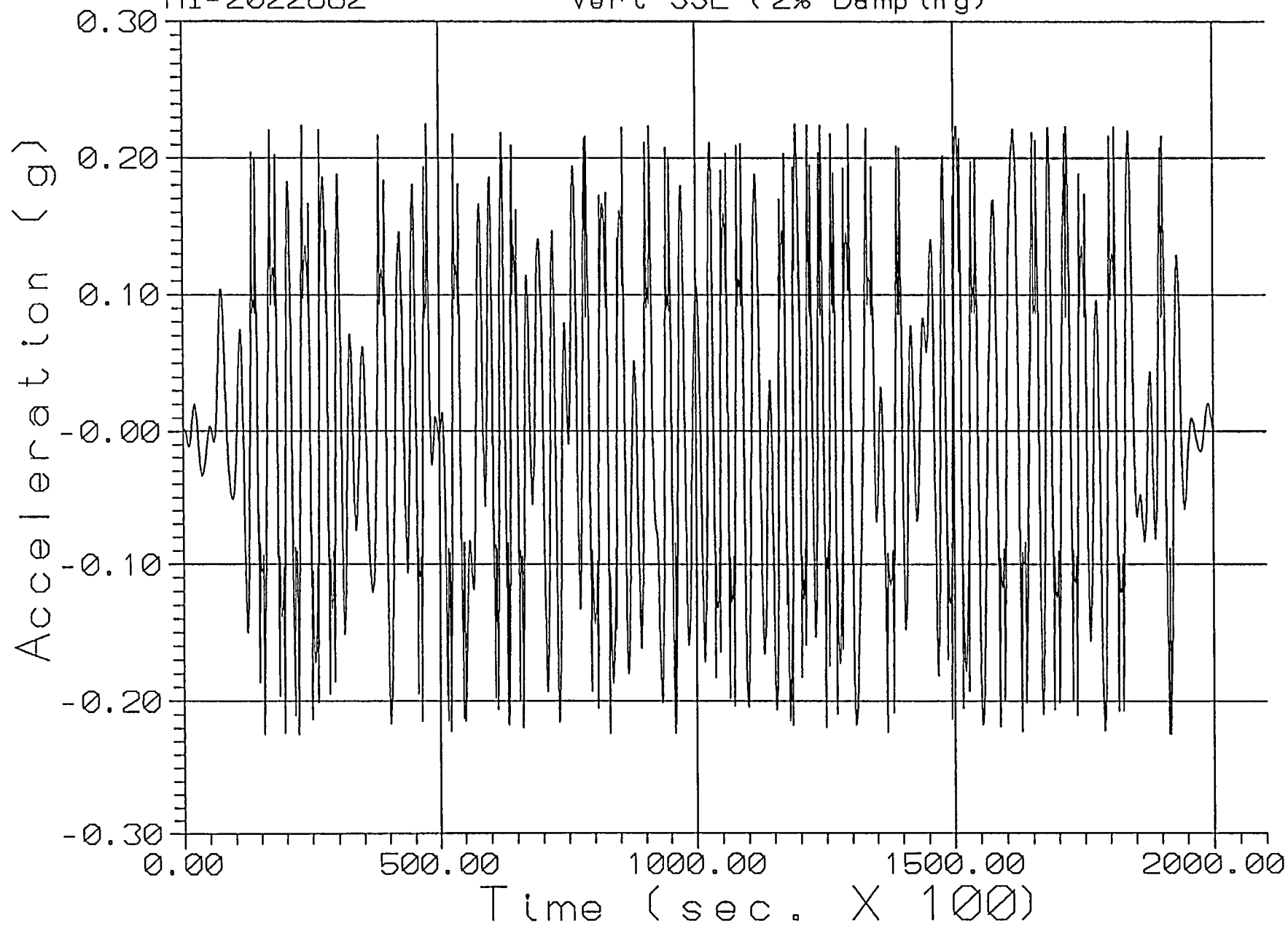


Figure 6.4.4
Holtec Report
HI-2022882

St. Lucie Unit 1 Elevation 21.50'
Time History Accelerogram
E/W Direction OBE (2% Damping)

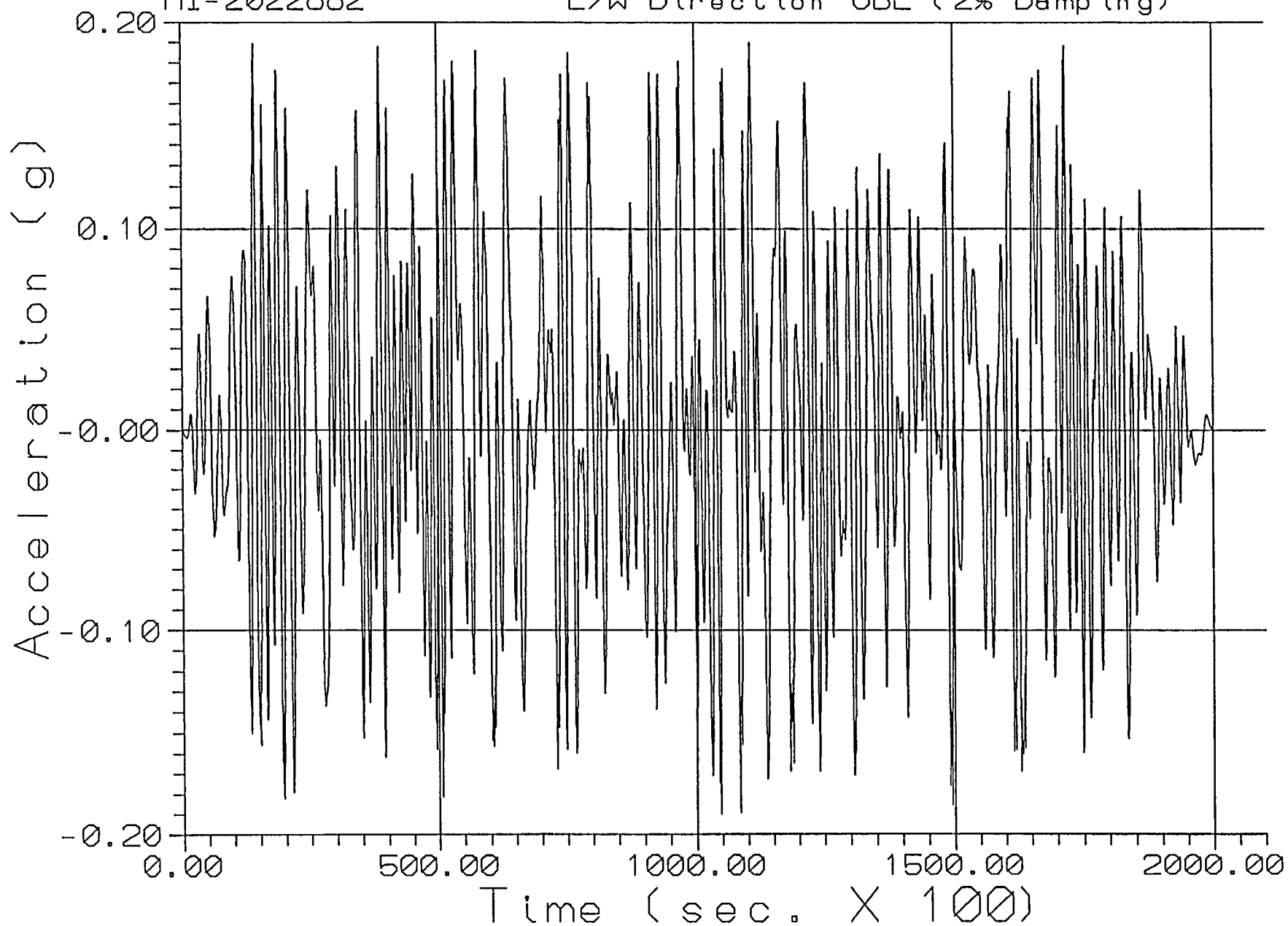


Figure 6.4.5
Holtec Report
HI-2022882

St. Lucie Unit 1 Elevation 21.50'
Time History Accelerogram
N/S Direction OBE (2% Damping)

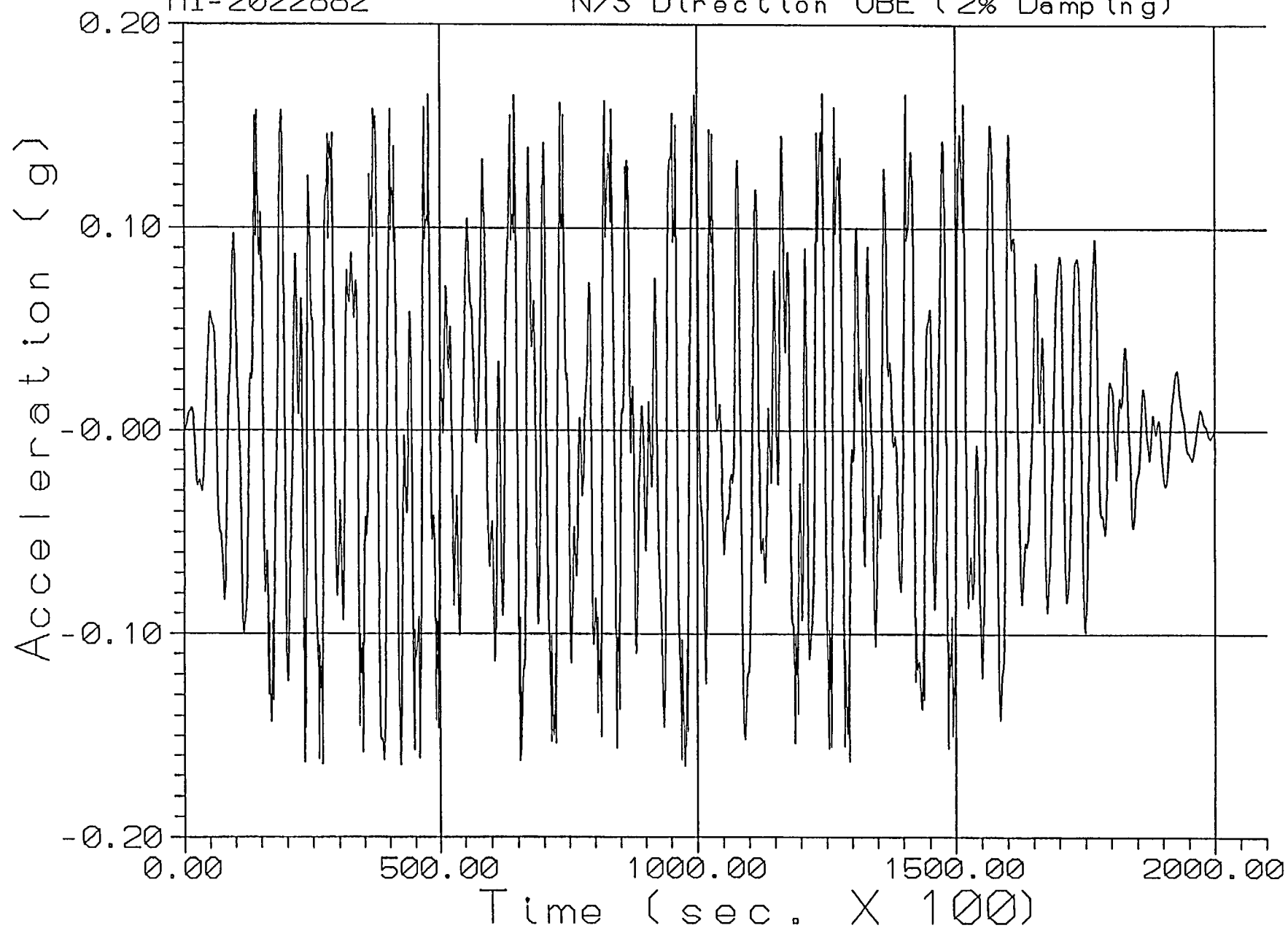
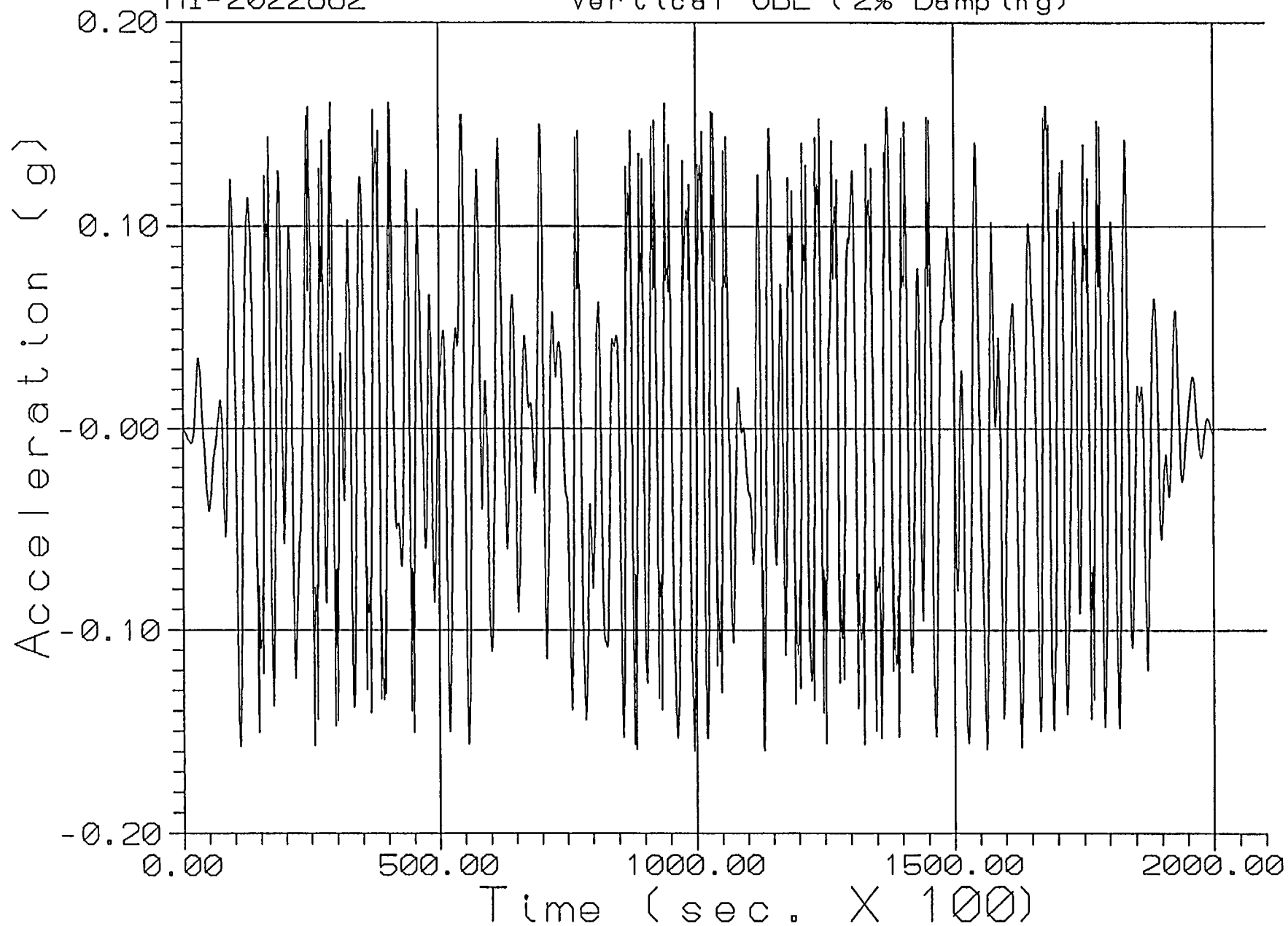


Figure 6.4.6
Holtec Report
HI-2022882

St. Lucie Unit 1 Elevation 21.50'
Time History Accelerogram
Vertical OBE (2% Damping)



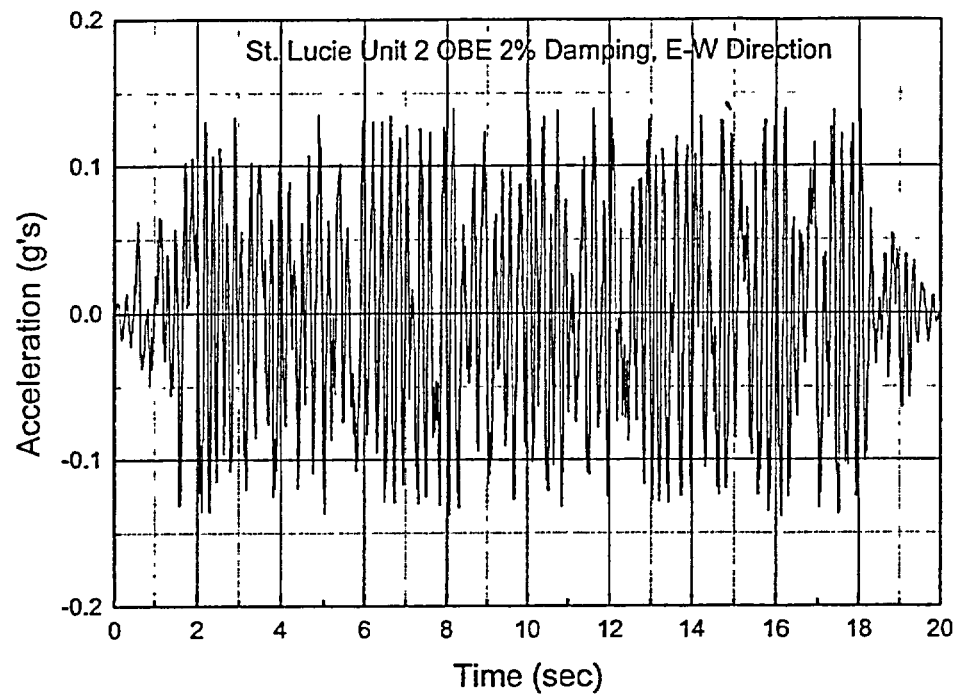


Fig. 6.4.7 OBE acceleration time history in the East-West direction

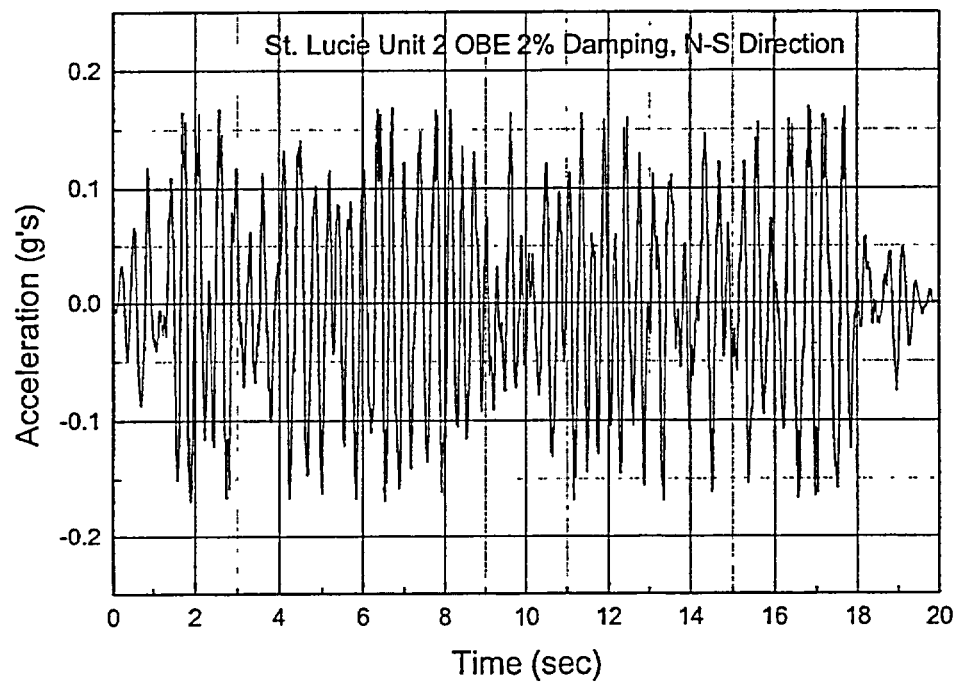


Fig. 6.4.8 OBE acceleration time history in the North-South direction

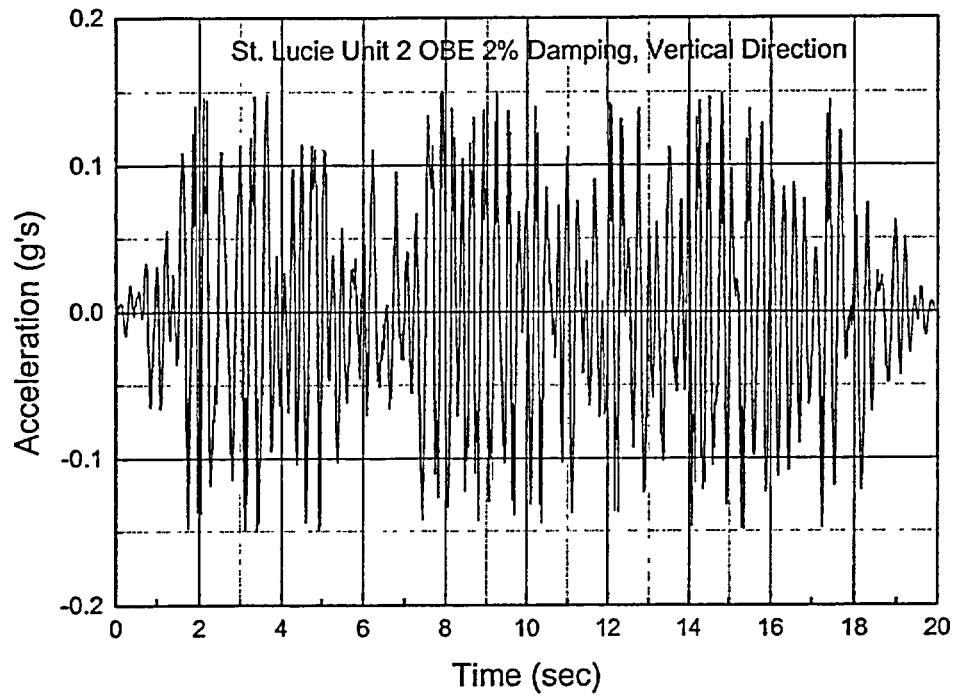


Fig. 6.4.9 OBE acceleration time history in the vertical direction

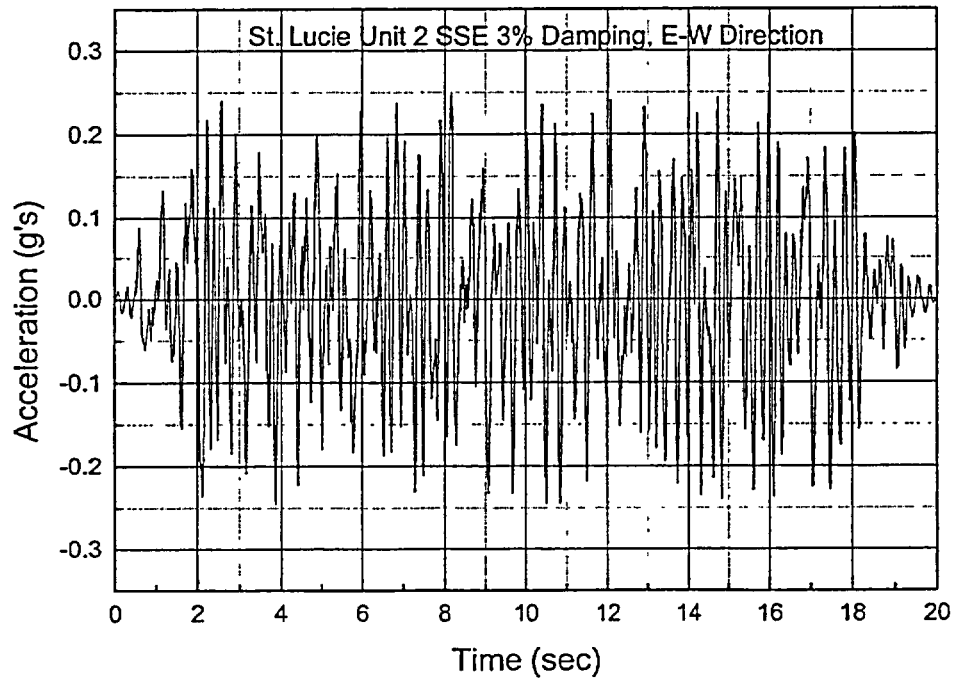


Fig. 6.4.10 SSE acceleration time history in the East-West direction

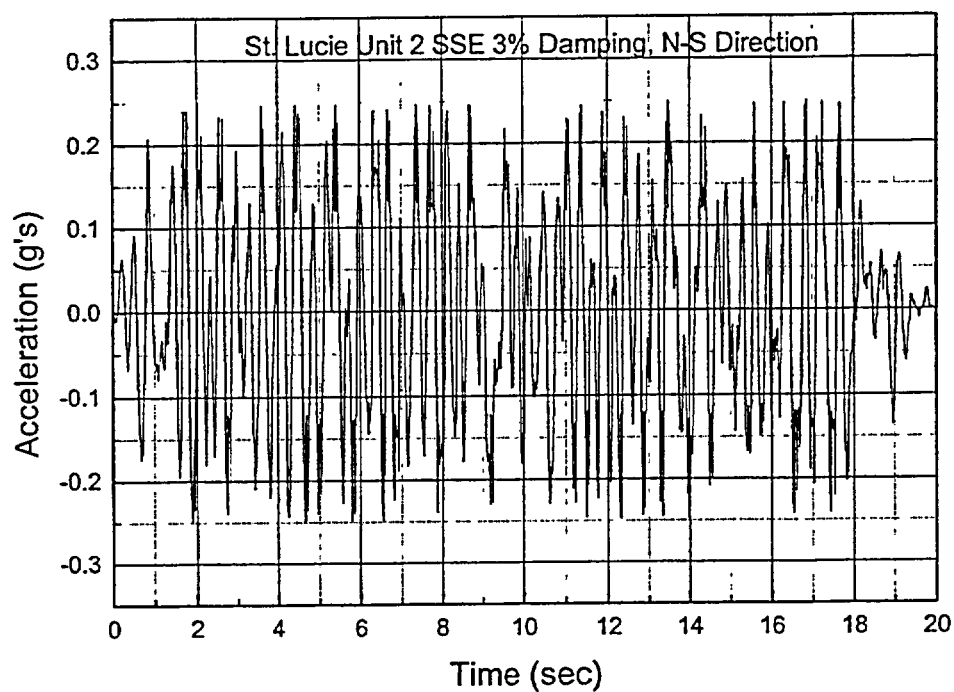


Fig. 6.4.11 SSE acceleration time history in the North-South direction

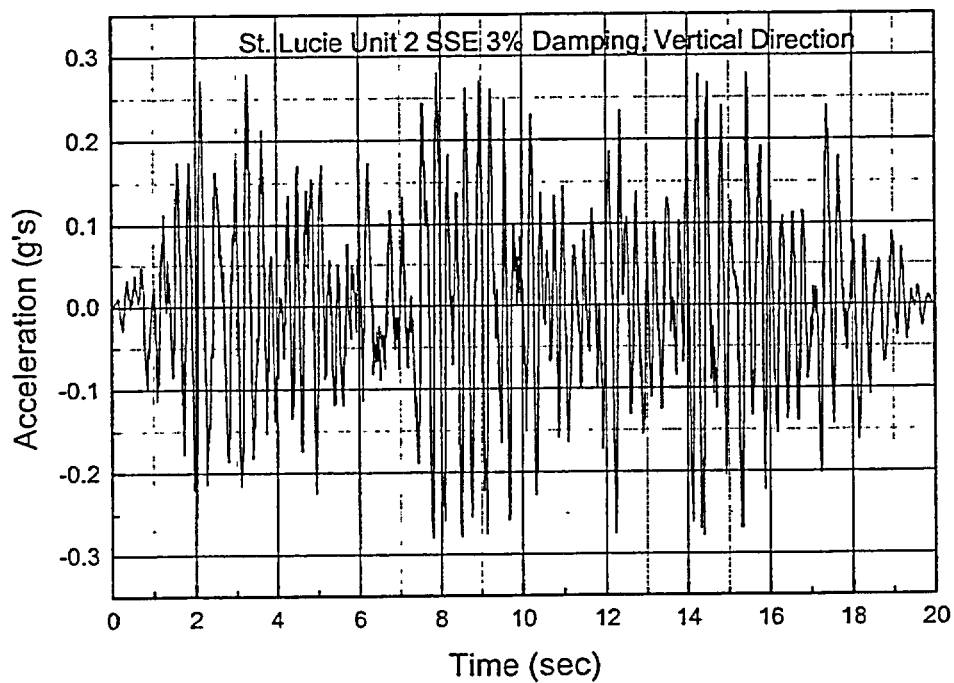


Fig. 6.4.12 SSE acceleration time history in the vertical direction

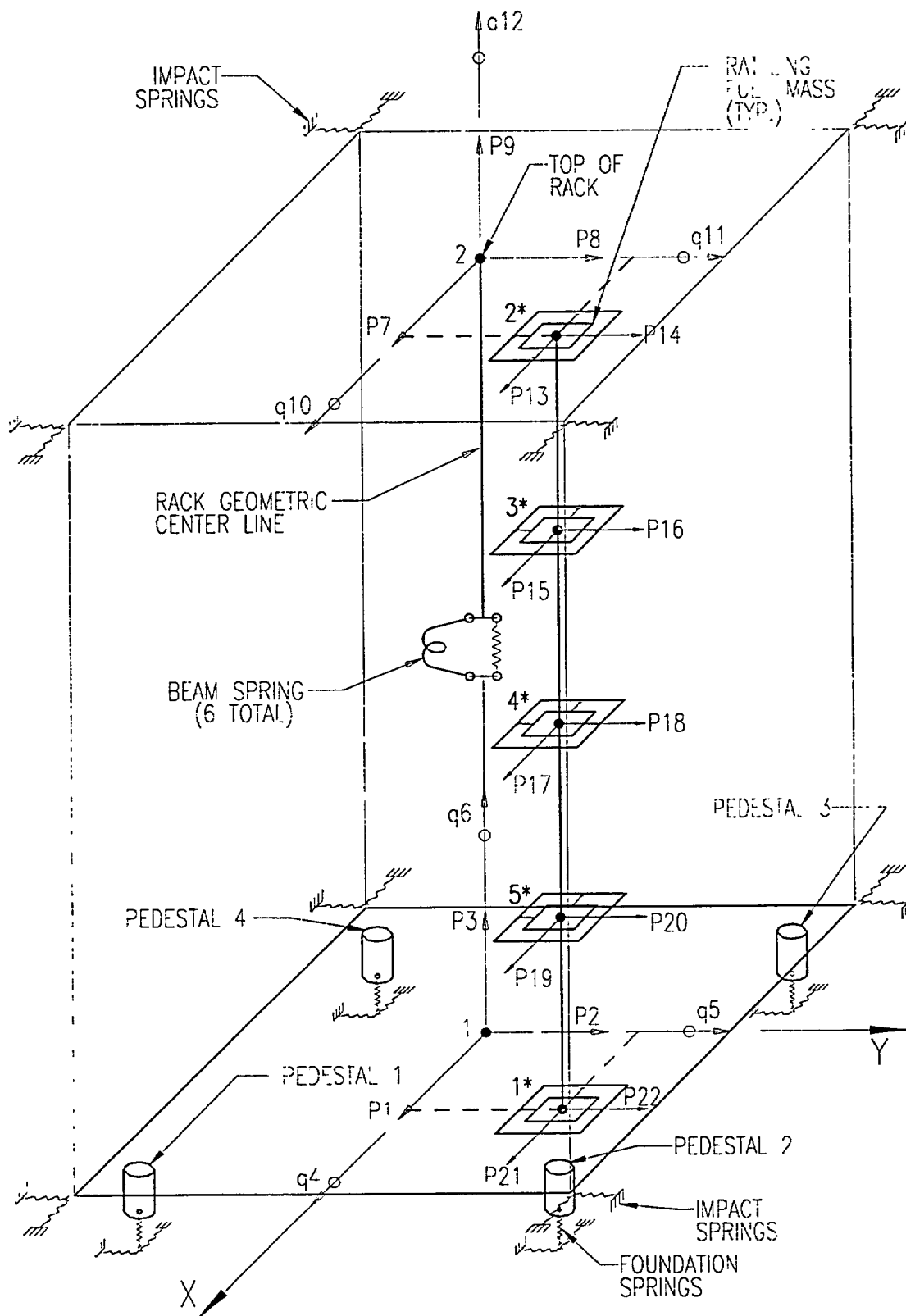


FIGURE 6.5.1; SCHEMATIC OF THE DYNAMIC MODEL OF A SINGLE RACK MODULE USED IN DYNARACK

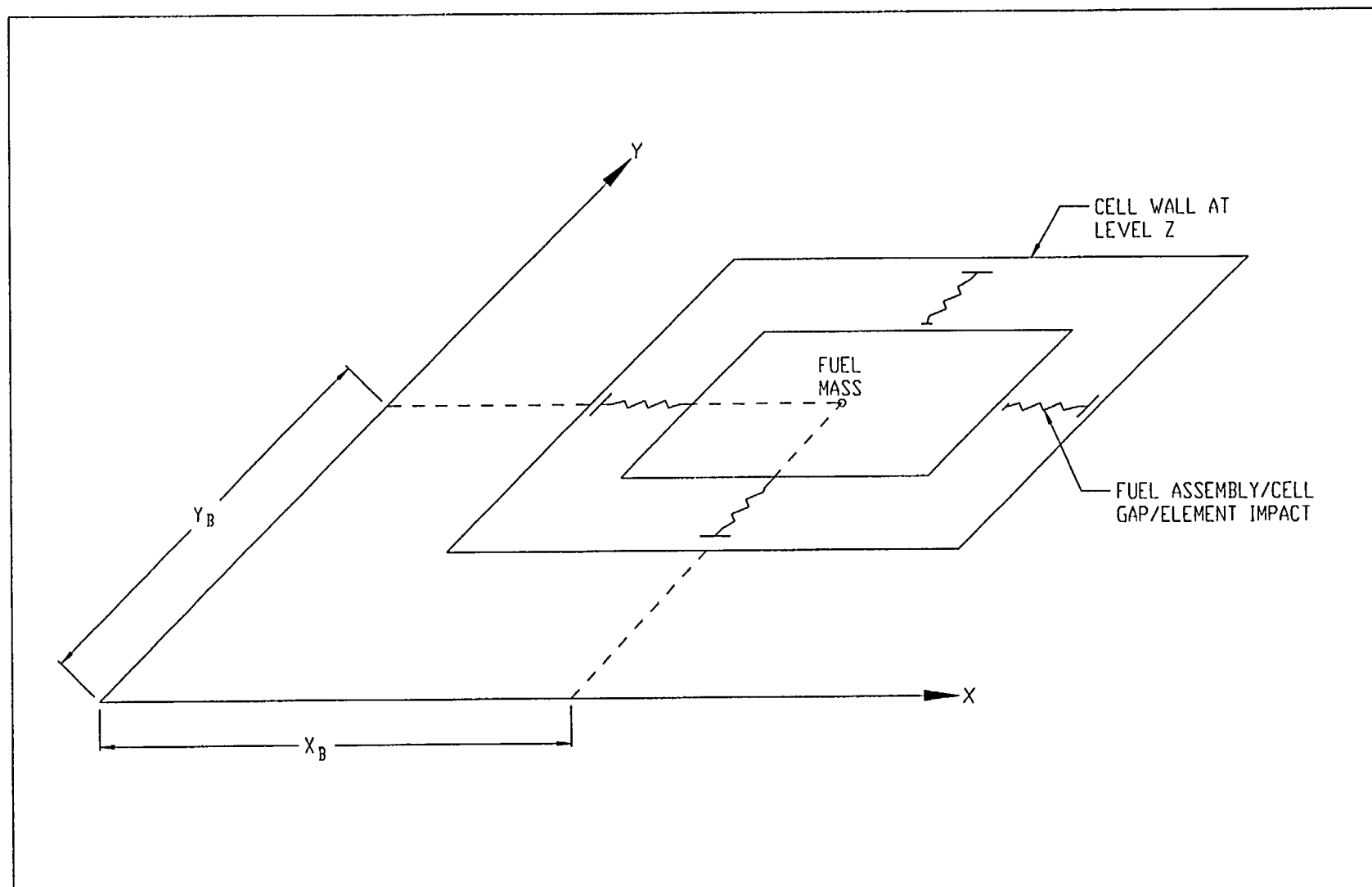


FIGURE 6.5.2; FUEL-TO-RACK GAP/IMPACT ELEMENTS AT LEVEL OF RATTLING MASS

HI201

HI-2022882

G:\DRAWINGS\0-FIGURES\1201\REPORT-HI-2022882\FIGURE 6.5.2

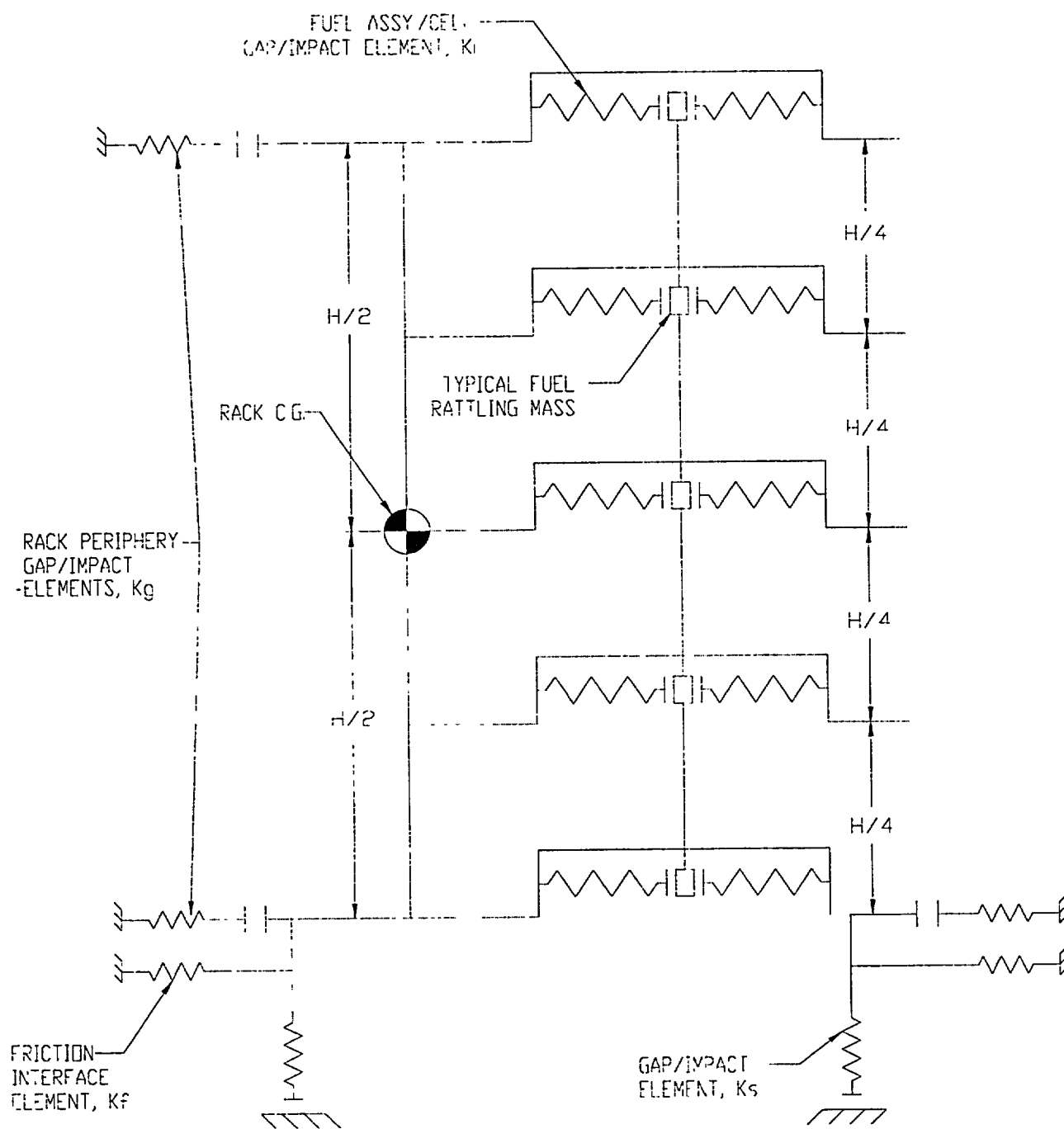
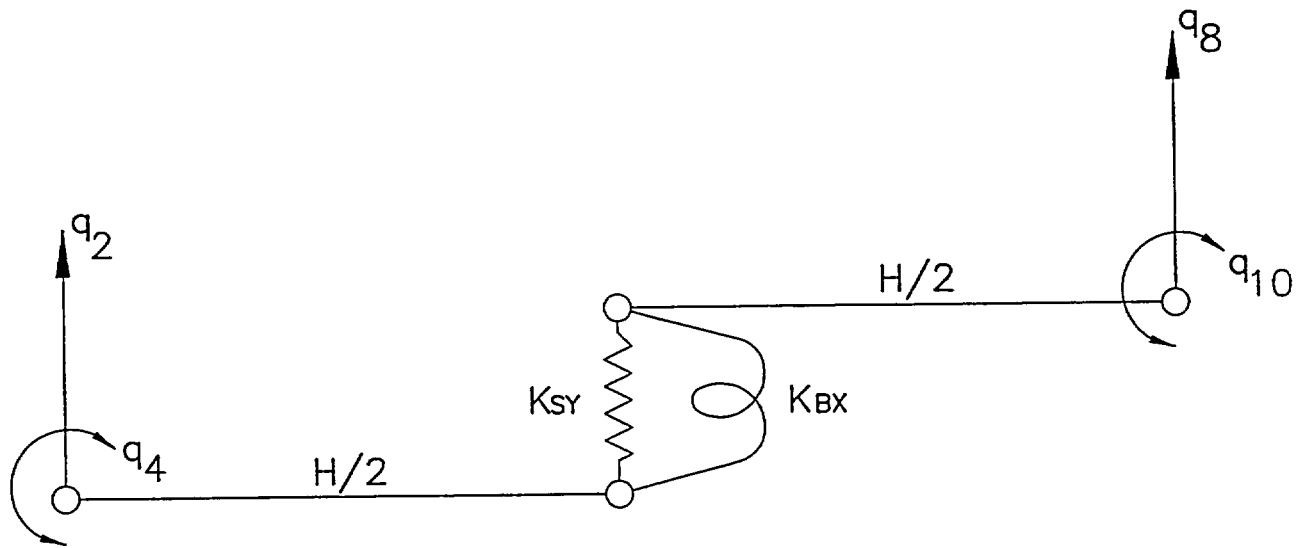
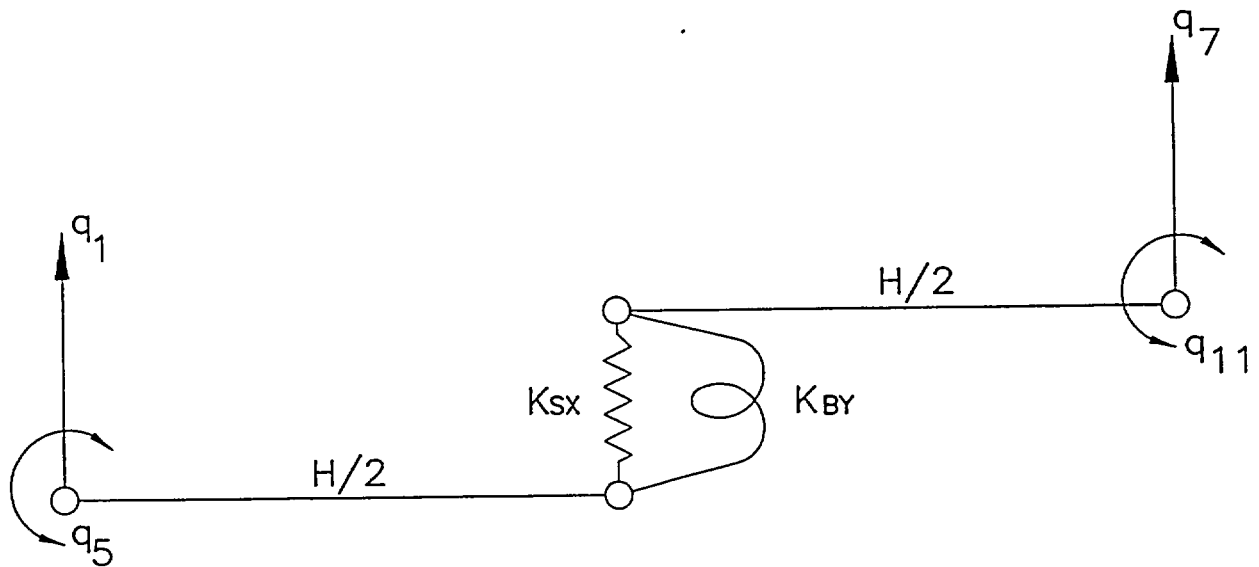


FIGURE 6.5.3; TWO DIMENSIONAL VIEW OF THE SPRING-MASS SIMULATION



FOR Y-Z PLANE BENDING



FOR X-Z PLANE BENDING

FIGURE 6.5.4; RACK DEGREES-OF-FREEDOM
WITH SHEAR AND BENDING SPRINGS

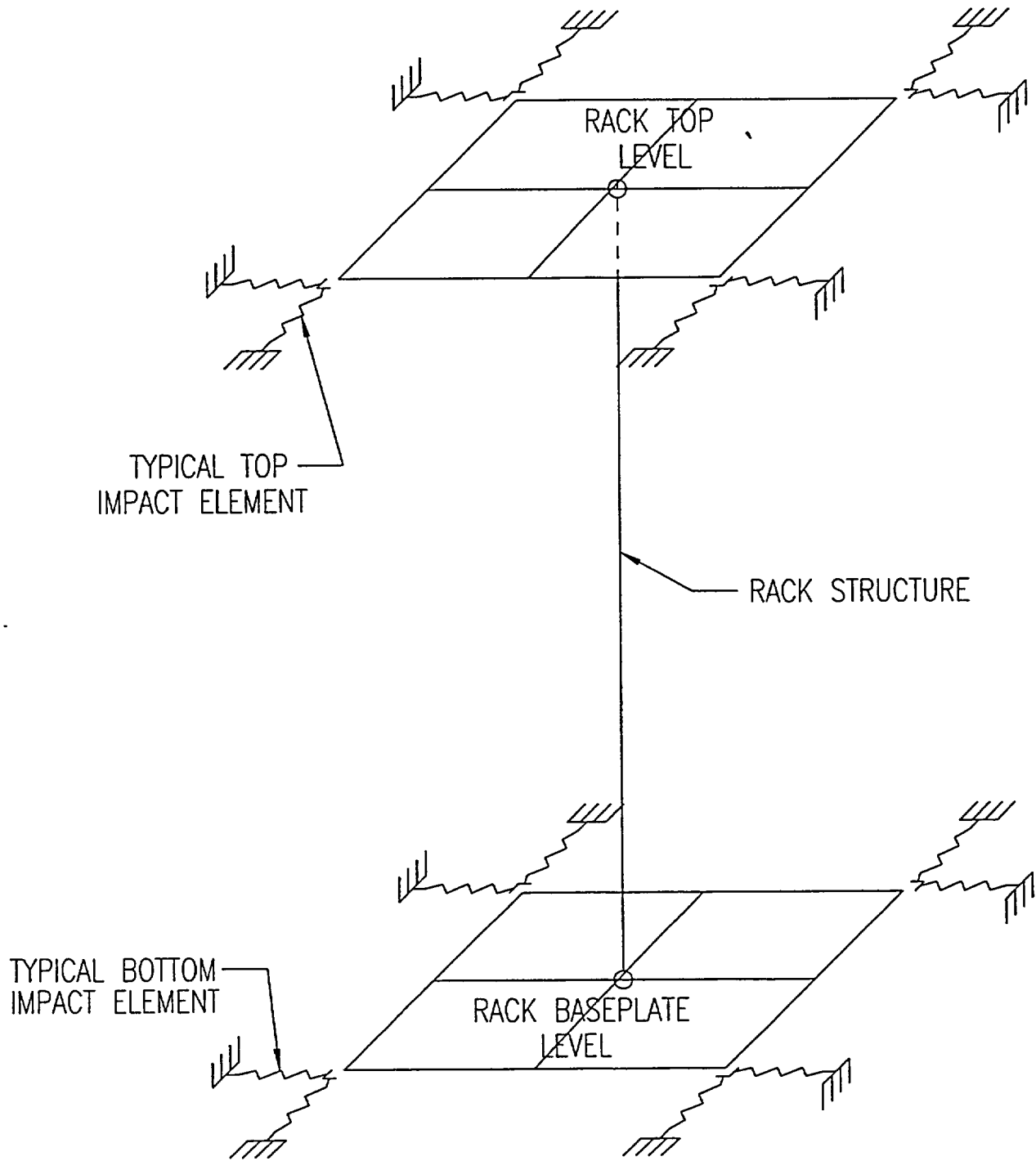


FIGURE 6.5.5; RACK PERIPHERY GAP/IMPACT ELEMENTS

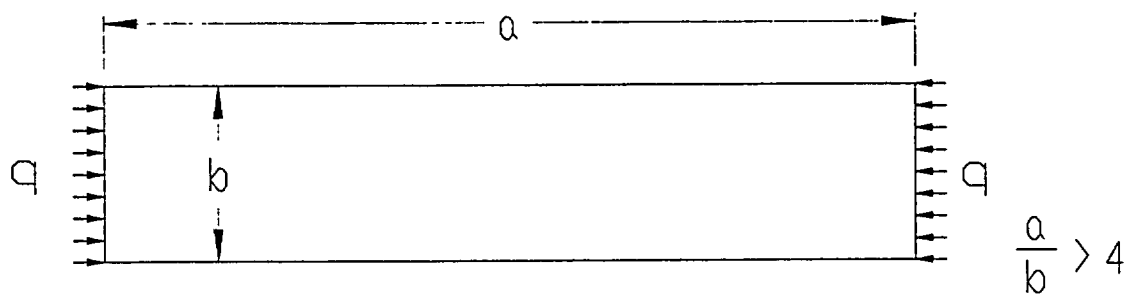


FIGURE 6.12.1; LOADING ON RACK WALL

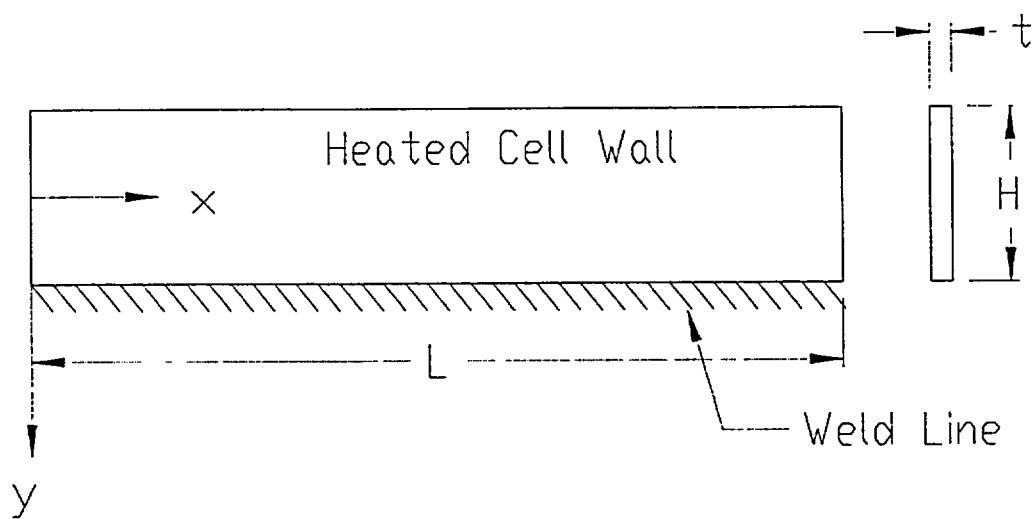


FIGURE 6.12.2; WELDED JOINT IN RACK